UNIVERSITY OF OKLAHOMA

GRADUATE COLLEGE

LABEL-FREE FLOW CYTOMETRY TO UNDERSTAND NANOPARTICLE-CELL INTERACTIONS

A THESIS

SUBMITTED TO THE GRADUATE FACULTY

in partial fulfillment of the requirements for the

Degree of

MASTER OF SCIENCE

By

MAJD HADDAD
Norman, Oklahoma
2023

LABEL-FREE FLOW CYTOMETRY TO UNDERSTAND NANOPARTICLE-CELL INTERACTIONS

A THESIS APPROVED FOR THE

STEPHENSON SCHOOL OF BIOMEDICAL ENGINEERING

BY THE COMMITTEE CONSISTING OF

Dr. Stefan Wilhelm, Chair
Dr. Rebecca Scott
Dr. Sarah Breen

Acknowledgments

I would like to particularly thank my advisor Dr. Wilhelm for taking me on as a Master's student. Dr. Wilhelm has been extraordinarily tolerant and supportive, and for that, I am very grateful. I extend my gratitude to my committee members, Dr. Scott and Dr. Breen, as their advice and comments have been of immense help in my journey of learning.

Additionally, I would like to acknowledge the help I received from Alex Frickenstein regarding collection of data using ICP-MS and TEM, as well as providing me with the written experimental methods for using SP-ICP-MS and TEM. Furthermore, I would like to thank Vinit Sheth for helping with the data collection using CLSM, as well as James Lowe for helping in some sample preparation.

Contributions

Alex Frickenstein: data collection using ICP-MS and TEM; providing the written methods for TEM and SP-ICP-MS characterization

Vinit Sheth: data collection using CLSM; aided in some sample preparation

James Lowe: helped in some sample preparation for flow cytometry experiments

Sarah Butterfield: aided in digestion of samples for ICP-MS

Yuxin He: helped in digestion of samples and cell standard curve preparation for ICP-MS

Table of Contents

List of Tables

List of Figures

Abstract

Understanding nanoparticle-cell interactions at single-nanoparticle and single-cell resolutions is crucial to improving the design of next-generation nanoparticles for safer, more effective, and more efficient applications in nanomedicine. This study partly focuses on recent advances in the continuous high-throughput analysis of nanoparticle-cell interactions at the single-cell level. We highlight and discuss the current trends in continual flow high-throughput methods for analyzing single cells centered around flow cytometry techniques. This study further discusses the challenges and opportunities with current flow cytometry approaches and provides proposed directions for innovation in the high-throughput analysis of nanoparticle-cell interactions.

With the information obtained from the investigation of the single-cell analysis methods, it was clear than such analysis methods at the single-cell level are necessary to understand cell behavior and nanoparticle-cell interactions. However, current methods, such as inductively coupled plasma mass spectrometry and microscopy, have some disadvantages, such as being labor-intensive and can affect nano-bio interactions. Therefore, we used flow cytometry (FCM) as a label-free technique to enhance our knowledge of nanoparticle-cell interactions. To understand how 100 nm gold nanoparticles (AuNPs) affect cellular behavior, we incubated the NPs with RAW 264.7 cells to examine the change in granularity. Upon confirming this change, we wanted to investigate how using different nanoparticles and cell types can impact nano-bio interactions. Our results show that larger nanoparticles increase the side scattering (SSC) readings, hence the complexity of cells. Next, we performed a kinetics analysis experiment to understand how the uptake of NPs influences cells over a period of 24 hrs. We found that NP uptake increases with time but reaches a plateau at higher NP concentrations towards the end of the investigation period. Additionally, we investigated

if endocytosis pathway for Heparosan (HEP)-coated 100 nm AuNPs can be determined. Despite using inhibitors from different pathways, we have not been able to confirm which pathway HEP-coated 100 nm AuNPs get uptaken by.

Chapter 1

Introduction

1.1 Thesis Introduction and Aims

This thesis serves two primary purposes: first, to explore flow cytometry as a single-cell method commonly used to analyze cells and cellular interactions, and second to highlight and experimentally validate a relatively simple, low-cost, label-free analysis method to monitor interactions of live cells with nanoparticles, or in other words, to assess nano-bio interactions.

1.2 Introduction

Creating safe, effective, and efficient nanomedicines for biomedical applications requires a thorough understanding of how administered nanoparticles interact with cells [1], [2]. These so-called nanotechnology-biology "nano-bio" interactions are complex and can occur with a broad range of efficiency, selectivity, and specificity, which is partially attributed to the substantial cell heterogeneity in both healthy and diseased tissues [3]. Such interactions occur between nanoparticles and cells. Nanoparticles' size ranges from 1-100 nm and can vary from inorganic to organic materials [4].

Nanoparticles are essential for therapeutic drug delivery, and can be even used in imaging diagnostics, and vaccination [5]–[8]. That being said, it is essential to determine how effective and safe the nanoparticles can be to be able to create better nanomedicine techniques [9], [10]. This can be made possible by examining the interactions between nanoparticles and cells at the single-cell level.

In batch mode, although information is obtained through population-based analysis thus providing trends in nano-bio interactions based on changes in nanoparticle characteristics, this technique does not allow for studying the distribution of nanoparticles within cells. Additionally, what can be seen in some cells, can provide assumptions of trends that are not necessarily the case for other samples.

Therefore, single-cell analysis methods are a better option for the study of nano-bio interactions. This is because it is possible to study how nanoparticle characteristics such as size, shape, and surface chemistry can influence nano-bio interactions [11]–[18]. This is made possible due to the increased resolution provided by such techniques as well as enhancing the understanding of cellular mechanisms and behaviors relative to cellular interactions. Finally, single-cell analysis for distribution analysis to understand the range of nano-bio interactions for a given system and can identify cells that contain no nanoparticles after treatment.

Current methods of analyzing nano-bio interactions at the cellular level include, amongst others, microscopy [19]–[21], flow cytometry [22], [23], and mass spectrometry [24], [25]. Such techniques enable visualization, analysis, and/or quantification of cells at varying degrees of spatial and temporal resolution. Importantly, flow cytometry allows for a continual flow analysis of cell samples which allows for the high-throughput assessment nano-bio interactions at the single-cell level.

In this thesis, we highlight current technologies and advancing trends in continual flow, high-throughput analysis used to assess nanoparticle-cell interactions with single-cell resolution. We focus our overview on flow cytometry. The advantages and considerations

of each technique are discussed while highlighting areas of current investigation and future growth to advance the study of nano-bio interactions at the single-cell level.

1.3 Literature Review and Connection to Data Collection

1.3.1 Flow Cytometry

Multiple approaches for flow cytometry have been employed to assess nano-bio interactions at the single-cell level. Table 1 provides a summary of selected recent studies in this research area. We discuss four different methods from the recently published literature, including conventional flow cytometry, imaging flow cytometry, photoacoustic (imaging) flow cytometry, and *in vivo* flow cytometry, and how these analytical methods have been used to study nano-bio interactions.

Table 1: Selected Nano-Bio Interaction Studies Using Different Flow Cytometry Approaches

Approach	Nanoparticle Type	Nanoparticle Size (nm)	Nanoparticle Function	Cell Line(s)	Notable Methods	Ref.
Conventional Flow Cytometry/FACS*	Silver	10, 50, and 100 nm	Affects expression of Toll-like receptors	RAW264.7 mouse leukemia cells	Allows for sorting of cells	[26]
	Silver	10, 50, and 75 nm	Affects cell growth and nanoparticle uptake	ARPE-19 human epithelial cells	Analysis of nanoparticle cell uptake based on the combination of light scattering and far-red fluorescence	[27]
	Silver	80 nm	Affects nanoparticle uptake	ARPE-19 human epithelial cells	Analysis of how different nanoparticle surface modifications affect nanoparticle cell uptake	[28]
	Gold nanospheres, Gold nanorods	26 nm and 67 nm × 33 nm, respectively	Used as intracellular imaging probes or as therapeutic reagents	MDA-MB-231 human breast cancer cells	Use of more red-shifted excitation lasers to enhance the optical signal of flow cytometry	[29]

Approach	Nanoparticle Type	Nanoparticle Size (nm)	Nanoparticle Function	Cell Line(s)	Notable Methods	Ref.
Conventional Flow Cytometry/FACS*	Gold	40, 60, 80, and 100 nm	Internalization in many different types of cells	HeLa human cervical cancer cells	Label-free quantification of nanoparticles within cells	[30]
	TiO_2	<10 nm	Chemical inertness	NIH/3T3 mouse fibroblasts and A549 human pulmonary cancer cells	Analysis of nanoparticle-cell interactions via fluorescence	[31]
	ZnO and TiO_2	30 and 50 nm, respectively	Commercially relevant in consumer products and nanodevices	*Escherichia coli* bacterial cells	Detection of nanoparticle uptake in bacteria	[32]

Approach	Nanoparticle Type	Nanoparticle Size (nm)	Nanoparticle Function	Cell Line(s)	Notable Methods	Ref.
Conventional Flow Cytometry/FACS*	TiO_2, SiO_2, CeO_2, and ZnO	TiO_2: ~168 nm –1um; SiO_2: 175 – 250 nm; CeO_2: <10nm and < 25nm; ZnO: ~41.5nm	Understanding of nanoparticle ecotoxicological effects	Freshwater algae (Raphidocelis subcapitata, Desmodesmus subspicatus, and Chlorella vulgaris)	Analysis of nanoparticle uptake in microalgae	[33]
	Ultrasmall nanoparticles	2 nm	Understanding protein corona interactions	A549 human pulmonary cancer cells	Detection of nanoparticle (<5 nm in diameter) interactions with cells	[34]
	CuS	8 nm	Evaluation of biocompatibility and toxicity	HeLa human cervical cancer cells	Photothermal efficiency analysis of the nanoparticles to determine cell viability	[35]

Approach	Nanoparticle Type	Nanoparticle Size (nm)	Nanoparticle Function	Cell Line(s)	Notable Methods	Ref.
Conventional Flow Cytometry/FACS*	Magnetite nanoparticles	10 nm	Relevant nanomaterial for diagnosis and cancer therapy	PC3 human cancer epithelial cells and BPH1 human healthy epithelial cells	Label-free quantification of various concentrations of nanoparticles with different surface chemistries within cells	[36]
	$NaYbF_4$@$NaYF_4$	~18 nm	Used due to their high stability, large anti-Stokes shift, and narrow emission bandwidth	A549 human pulmonary cancer cells	Examines side scattering vs. fluorescence intensity of the single-cell suspension rather than comparing side scattering to forward scattering	[37]
	SiO_2	~27 nm and ~70 nm	Enhanced (colloidal) stability	A549 human pulmonary cancer cells	Analysis of fluorescence intensity of nanoparticles rather than side scattering of the single-cell suspension	[38]

Approach	Nanoparticle Type	Nanoparticle Size (nm)	Nanoparticle Function	Cell Line(s)	Notable Methods	Ref.
Conventional Flow Cytometry/FACS*	Fluorescently-labeled polystyrene nanoparticles	40, 100, and 200 nm	Nanoparticle size tunability	HeLa human cervical cancer cells	Detection of nanoparticle interactions with various intracellular organelles	[39]
	Fluorescently-labeled polystyrene nanoparticles	100 nm	Size tunability	MDA-MB-231 human breast cancer cells	Correlation of nanoparticle uptake with cell size rather than cell complexity	[40]
	Fn14-Targeted polymeric nanoparticles	~96-163 nm	Used due to their prolonged systemic circulation, enhanced tumor accumulation, and extended tissue penetration and drug release	Human MDA-MD-231-TD-luciferase triple negative breast cancer cells	Uptake analysis of fluorescently labeled nanoparticles by cells	[41]

Approach	Nanoparticle Type	Nanoparticle Size (nm)	Nanoparticle Function	Cell Line(s)	Notable Methods	Ref.
Conventional Flow Cytometry/FACS*	Polymeric nanoparticles	~45 nm	Used due to their ability to label cells, and usage in imaging modalities	Primary macrophages	Analysis of nanoparticle-labeled cells	[42]
	Polymeric nanoparticles	128 nm	Used due to their abilities to scavenge reactive oxygens, serving as an effective therapy for atherosclerosis	RAW264.7 mouse leukemia cells	Analysis of fluorescence intensity of nanoparticles rather than side scattering of the single-cell suspension	[43]
	Gag-based virus-like particles	161 and 184 nm	Used due to their potential as candidates for recombinant vaccine development	Insect-derived cells (S. frugiperda and T. ni BTI-TN-5B1-4)	Allows for baculovirus infection process comparison between different insect cell lines	[44]

Approach	Nanoparticle Type	Nanoparticle Size (nm)	Nanoparticle Function	Cell Line(s)	Notable Methods	Ref.
Imaging Flow Cytometry	SiO_2	50 nm	Used due to their ability to be easily labeled with different fluorochromes	NCI-H292 human pulmonary cancer cells	Evaluation of nanoparticle internalization at different temperatures	[45]
	Polymeric nanoparticles	~50 nm	Used due to their ability to enhance light absorption, induce photoacoustic signals, and high cell viability	B16-F10 mouse melanoma skin cancer cells	Analysis of nano-bio interactions on an on-chip photoacoustic imaging flow cytometer	[46]
	CD63-eGFP–transfected HEK293T extracellular vesicles	~104nm	Used due to their inherent rapid proliferation, high EV yield, and ease of genetic manipulation	HEK293T human embryonic kidney cells	Imaging of sEVs down to 100 nm in diameter	[47]

Approach	Nanoparticle Type	Nanoparticle Size (nm)	Nanoparticle Function	Cell Line(s)	Notable Methods	Ref.
Imaging Flow Cytometry	eGFP-labelled small extracellular vesicles	130 nm	Used due to their abundance, ability to control various processes and mediate complex intercellular interactions in a targeted manner	THP-1 human leukemia cells	Discrimination between single and coincidental sEVs	[48]
Photoacoustic (Imaging) Flow Cytometry	CuS	8.6 nm	Used due to their ability to specifically target ovarian circulating tumor cells and capability to emit a photoacoustic signal	SKOV-3 human ovarian cancer cells	Real-time imaging of sample	[49]

Approach	Nanoparticle Type	Nanoparticle Size (nm)	Nanoparticle Function	Cell Line(s)	Notable Methods	Ref.
Photoacoustic (Imaging) Flow Cytometry	CuS NPs	8.6 nm	Used due to their ability to enable specific binding of ovarian-cancer cells and PA detection	SKOV-3 human ovarian cancer cells	Detection of early-stage cancer metastasis	[50]
	Gold nanorods	25 × 113 nm	Used due to their ability to enable PA detection at the single-cell level	MDA-MB-231 human breast cancer cells and ZR-75-1 human breast cancer cells	Analysis of nanoparticle toxicity	[51]
	Streptavidin coated red fluorescent latex nanoparticles	320 nm	Used due to their ability to be detected and attached to breast cancer cells	T-47D human breast cancer cells	Detection of colocalized nanoparticles within breast cancer cells in a coculture sample	[52]

Approach	Nanoparticle Type	Nanoparticle Size (nm)	Nanoparticle Function	Cell Line(s)	Notable Methods	Ref.
Photoacoustic (Imaging) Flow Cytometry	Polymeric nanoparticles	Not Reported	Used to their ability to label cells, identify, and eliminate glioma cells	9L mouse glioma cells, HeLa human cervical cancer cells, and C6 mouse glioma cells	Multiparametric labeling and identification of cells in a single workflow	[53]
***In vivo* Flow Cytometry**	Pristine graphene flakes	1 – 1.2 nm	Used due to their tremendous potential in various medical applications	Red Blood Cells	Imaging of circulating GBN clusters in blood vessels and assessment of their kinetics	[54]
	Quantum dot-carbon nanotube conjugates	~5 nm	Used due to their ability to be photothermal, photothermal and fluorescent contrast agents	Plant xylem and phloem vascular systems	In vivo real-time photoacoustic monitoring of nanoparticle uptake in plants	[55]

Approach	Nanoparticle Type	Nanoparticle Size (nm)	Nanoparticle Function	Cell Line(s)	Notable Methods	Ref.
***In vivo* Flow Cytometry**	Gold nanorods	~10 × 35 nm	Used due to their ability to be used as magnetic–photothermal switchable probes	Melanoma cells	Uses high-pulse-repetition rate laser	[56]
	Gold nanorods	15 × 50 nm	Used due to their ability to label circulating cell tumors, allowing for the cells' detection	HTB-65 human melanoma cells, MALME-3M human melanoma skin cancer cells, and B16-F10 mouse melanoma skin cancer cells	Blood cancer testing using a high-pulse-repetition-rate diode laser	[57]

Approach	Nanoparticle Type	Nanoparticle Size (nm)	Nanoparticle Function	Cell Line(s)	Notable Methods	Ref.
***In vivo* Flow Cytometry**	Magnetic nanoparticles and golden carbon nanotubes	30 nm	Used due to their ability to target a breast cancer cells' receptor, and to improve detection sensitivity and specificity, respectively	MDA-MB-231 human breast cancer cells	Detection of cells in the bloodstream	[58]
	Polylactic acid	100 nm	Used due to their ability to circulate longer in the bloodstream and form less aggregates	Primary mouse monocytes	Simultaneous monitoring of monocytes and nanoparticles *in vivo*	[59]
	Polymeric nanoparticles	~107 – 122 nm	Used due to their effect to target and neutralize circulating tumor cells	4T1 mouse breast cancer epithelial cells	Detection of labeled cancer cells *in vivo* using polymeric modified and labeled nanoparticles	[60]

Approach	Nanoparticle Type	Nanoparticle Size (nm)	Nanoparticle Function	Cell Line(s)	Notable Methods	Ref.
***In vivo* Flow Cytometry**	Carbon nanotubes	Length: 186 nm; Diameter: 1.7 nm for the single-walled Length: 376 nm; Diameter: 19.0 nm for the multiwalled	Used due to their ability to be used as near infra-red high-photoacoustic contrast agent	*Escherichia coli* bacterial cells	Detection of labeled bacteria *in vivo*	[61]

* FACS = fluorescence-activated cell sorting

1.3.2 Conventional Flow Cytometry

Conventional flow cytometry is a technique in which individual cells are passed through a microfluidic system and subsequently illuminated by a laser source [23], [62]. Upon interaction of the cells with the laser light, the scattered light and any fluorescence emissions are detected and quantified. This analysis provides insight into various cell parameters, including cell identity, phenotype, and viability. Light scattered from an individual cell is typically quantified in a label-free way as side scattering or forward scattering depending on whether the scattered light is detected orthogonally to the laser or in the same axis as the laser, respectively [63]. Generally, the label-free side scattering signal correlates with cell granularity or complexity, while the label-free forward scattering signal correlates with cell size. Besides light scattering, the laser may also excite

fluorescence emissions from dyes used to label the cells, thus allowing for the identification and quantification of cells based on the specific fluorescence emission profiles [64].

Upon interaction with cells, nanoparticles can contribute to the label-free side scattering and forward scattering signals detected by the flow cytometer (Figure 1A) [29], [65]. The nanoparticle contribution to side scattering signal varies based on both the nanoparticle type and nanoparticle concentration. The effect of nanoparticle concentration on the side scattering signal was reported in a study by Youhannavee *et al.* An increase in magnetite nanoparticle concentration resulted in an increase in detected side scattering signal due to increased nanoparticle-cell interactions (Figure 1B) [36]. This same study further showed how nanoparticle uptake varies by cell type. For the same magnetite nanoparticle concentration, PC3 human epithelial cancer cells showed increased nanoparticle-cell interactions compared to BPH1 human healthy epithelial cells. Other studies have reported similar trends whereby after increasing the nanoparticle concentration, cells more readily interact with nanoparticles, which results generally in an increase in label-free flow cytometry side scattering signal [26], [66].

Additionally, the forward scattering signal can be used to check for apoptotic cells. FSC changes when cells die due to apoptosis. Cells that undergo apoptosis have a decreased forward scattering signal as the cell size decreases due to cell shrinkage, while the side scattering signal increases due to changes in cell granularity associated with the formation of apoptotic bodies within the cell [67]. Tracking these changes in cell scattering signal can be used to determine the effect of nanoparticle concentration or toxicity on cells. For instance, Taccola *et al*. found that the threshold value at which

ZnO nanoparticles start inducing cell death in SH-SY5H human neuroblastoma cells is at a concentration of 0.42 mM. The authors used propidium iodide stain to compare live versus dead cells and confirm that the decrease in measured forward scattering signal is due to the threshold concentration value of the nanoparticles [68].

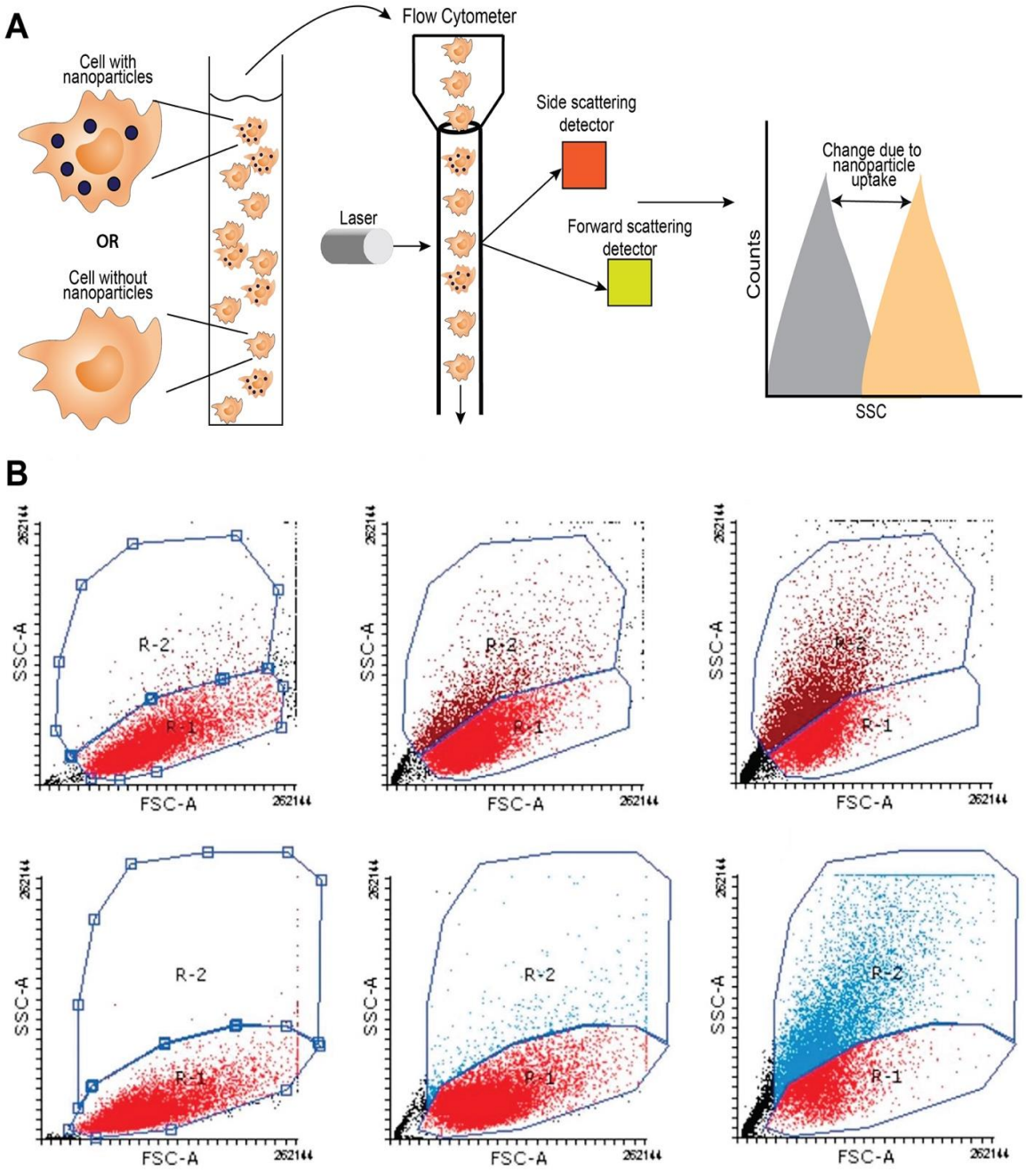

Figure 1: Flow cytometry for label-free quantification of nanoparticle-cell interactions. (A) A schematic overview of the sample introduction and measurement workflows. A single-cell suspension is run through the flow cytometer. At the interrogation point, data is collected and a histogram showing the count vs side scattering is generated. The side scattering values increase with the magnitude of nanoparticle interactions with cells. **(B)** PC3 cells (top line) and BPH1 cells (bottom lines) were exposed to magnetite nanoparticle at concentrations of 0, 100 and 500 $\frac{\mu g}{mL}$ (left to right), and nanoparticles were detected in a label-free way using flow cytometry-based measurements of side scattering signal and forward scattering signal. Adapted with permission from [36]. Copyright 2023 Journal of Magnetism and Magnetic Materials.

Conventional flow cytometry is further capable of detecting how differences in nanoparticle surface chemistry affect cellular interactions [34]. In a study by Zucker *et al.*, silver nanoparticles (AgNPs) of varying surface modifications, i.e., branched poly(ethyleneimine) (bPEI), citrate (CIT) polyvinylpyrrolidone (PVP), and poly (ethylene glycol) (PEG), were used to treat ARPE-19 human epithelial cells. Significant differences in the measured side scattering signals were observed between the different AgNP surface chemistries when cells were assessed with label-free flow cytometry after nanoparticle incubation [28]. Cells treated with positively charged AgNP-bPEI demonstrated greater side scattering signals by 3-6 fold compared to the other tested surface chemistries. A similar experiment by Chakraborty *et al.* was performed using gold nanorods (GNRs). The nanoparticles were surface-modified with PEG, poly(allylamine hydrochloride) (PAH), polystyrene sulfonate (PSS), or CIT the corresponding nanoparticle-cell interactions with human THP1 differentiated M1 and M2 macrophages were assessed by label-free flow cytometry. The greatest side scattering signal in both M1 and M2 macrophages was measured in cells treated with positively charged PAH-GNRs [69]. These observations are in line with reports by Lee *et al*. and Donahue *et al*., who used inductively coupled plasma mass spectrometry to quantify the effect of positive surface charges on nanoparticle-cell interactions [70], [71].

Conventional flow cytometry has also been used to assess how nanoparticle composition influences nano-bio interactions, as shown by Kumar *et al*. The researchers reported higher side scattering signals from *E. coli* bacterial cells exposed to TiO_2 nanoparticles compared to the same concentration of ZnO nanoparticles. The observed increase in the side scattering signal can be attributed to a greater degree of interaction

between *E. Coli* and TiO_2 nanoparticles [32]. The authors attribute that signal increase to the size of the TiO_2 nanoparticles, in which the TiO_2 nanoparticles were of a smaller size than that of the ZnO nanoparticles.

The ability of conventional flow cytometry to identify and quantify individual cells, while gaining insight into nanoparticle interactions with cells, does come with some notable limitations. Firstly, the number of fluorescent channels in a conventional flow cytometer is limited due to spectral overlaps of fluorophores, limiting the ability to quantify complex cellular phenotypes, as needed for many immunological studies [22], [72]. It is challenging to directly image cells using conventional flow cytometry which lacks spatial resolution, leading to a loss of spatial information [73]. The lack of imaging further complicates identification and resolution of coincidental events, where multiple cells interact with the laser simultaneously. Conventional flow cytometry is further prone to some ambiguity in results, as cell debris or nanoparticle aggregates will be detected alongside whole cells [74], [75]. Careful selection of appropriate control groups and tools, such as gating strategies and scattering signal threshold settings, are needed to address this limitation [75]. Moreover, quantifying protein abundance from raw fluorescence signals remains challenging with conventional flow cytometry. Finally, antibody labeling is challenging for some cells or cell markers, complicating the analysis of specific cell lines [76].

Recent innovative contributions have aimed to overcome some of the limitations of conventional flow cytometry. For instance, the implementation of microfluidics-based cytometry, which uses a microchannel with a microfabricated window for detecting fluorescence signals, enables cell characterization and detection of intracellular

proteins [77]. Cells tagged with fluorescent dye-labeled antibodies can pass through the microchannel to evaluate and quantify fluorescence emission intensity. Additionally, this method allows for quantification of cell diameter and the absolute number of proteins and associated protein concentration at the single-cell level, as demonstrated by Li *et al*. The researchers quantified the number of β-actin proteins on A549 human lung cancer cells, Hep G2 human liver cancer cells, MCF 10 non-tumorigenic human breast epithelial cells, and HeLa human cancer cells. Although this study did not quantify nano-bio interactions, it is worth noting that this study can be improved upon to characterize proteins, such as p53, at the single-cell level to allow for the study of tumor heterogeneity and nano-bio interactions through examining the effect of nanoparticles on cancer cells [77].

Spectral analyzer technologies have been applied to conventional flow cytometers, creating a spectral fingerprint that measures the full fluorescence emission spectra in multicolor samples for each individual fluorochrome. Each spectrum is isolated for precise signal determination [22], [78], [79]. Furthermore, a spectral analyzer allows for the analysis of up to 48 channels, thus substantially expanding the analysis capabilities of conventional flow cytometers [78].

RNA flow cytometry, which facilitates the detection of multiple RNA transcripts with high sensitivity from single cells in heterogeneous samples, has also demonstrated significant promise [75]. RNA flow cytometry utilizes RNA expression as an identifier, particularly in cases where antibodies cannot be used to label the cells of interest. Additionally, RNA flow cytometry allows for analyzing gene expression through the detection of fluorescent tags attached to the cell targets. Correlation between mRNA transcripts and antigen expression of tagged cell proteins can be made at the single-cell

level, allowing for analysis of metabolic profile, cell type, or cell stage [76], [80]. New developments have been made in which techniques such as simultaneous quantification of protein expression and multiple mRNA transcripts at the single cell level can occur [81], [82]. This simultaneous analysis allows for the correlation of mRNA with changes in cellular proteins at the single-cell level.

1.3.3 Spectral Flow Cytometry

Spectral flow cytometry improves upon conventional flow cytometry by using an optical filter-based division multiplexer to disperse emitted light across sensitive arrays of photodiodes [83], [84]. Typically, spectral flow cytometry has been used to analyze high-abundance proteins on cells for immunophenotyping [79], [85], [86].

Recently, the technology has been improved upon through methods that decrease probing volume and increase the exposure time of each particle in the cell sample to the laser, improving photon generation and minimizing background signal [84]. These changes have been implemented through the creation of spectral nano-flow cytometry (nFCM), which allows for the detection of nanoparticles interactions with cells, with particles as small as 7 nm being successfully detected [84], [87]–[90]. nFCM has been reported to be 4-6 orders of magnitude more sensitive in detecting side scattering signal and 1-2 orders of magnitude more sensitive in fluorescence emission detection compared to conventional flow cytometry [91]. The increased sensitivity of nFCM is attributed to significant background signal reduction and an increased spectral resolution of 2.1 nm [84], [92]. The increased spectral resolution of nFCM is made

possible by the holographic grating that rejects out-of-focus scattering signals and ensures that the photons are dispersed according to wavelength [84], [93].

A study by Li *et al*. used nFCM to quantify biotinylated *E. Coli* labeled with different quantum dot (QD) streptavidin conjugates, i.e., QD525, QD565, QD605, QD655, and QD705. nFCM was needed for this study to effectively resolve between the different side scattering signals obtained from the five different QDs used. The results demonstrated an increase in spectral intensity associated with each of the quantum dots bound to specific bacterial antigens, allowing for the identification of differing antigen-presenting bacterial cells through nanoparticle labeling [84].

Given its sensitivity, nFCM has been instrumental in studies investigating extracellular vesicles (EVs) [94]. These Evs can be extracted from platelet-free plasma or derived from cells, such as HCT15 human colon adenocarcinoma cancer cells [94]. EVs can be tagged with fluorophore-conjugated antibodies, and their associated fluorescence emission can be detected by nFCM. The interest in EVs stems from their utility as RNA delivery vehicles or as immunosuppression agents. Choi *et al*. assessed differences in rates of nanoparticle-cell interactions in A431 human epidermoid cancer cells. A431 cells were incubated with extracellular vesicles (EVs) that were derived from these cells and were then analyzed using nFCM to understand the EV populations interacting with the A431 human cancer cells. The data showed a highly heterogeneous distribution of some elements of the EVs, such as surface protein receptors, among all analyzed cells [95].

1.3.4 Imaging Flow Cytometry

To allow for visualization of cells as they are analyzed during flow cytometry, imaging flow cytometry has become a recent focus of flow cytometry investigations. Imaging flow cytometry combines conventional flow cytometry with fluorescence microscopy such that cell features can be imaged and spatially resolved during data collection [96]–[98]. In imaging flow cytometry, cells are imaged using either a traditional CCD camera or a photomultiplier (PMT) method as they flow through the microfluidic channels leading to the laser (Figure 2A-2C) [99]. 2D imaging allows for cell phenotyping by visualizing the cells' physical characteristics. Imaged data can be obtained when a laser on cells in the flow tank, which then get processed and digitized through appropriate microscope objective lenses as well as flow cytometric lenses and filters [100], [101]. In addition to the images, traditional flow cytometry light scattering signal data [99], [102]. The imaging capabilities of imaging flow cytometry allow for the detection of cell movement as well as the colocalization of nanoparticles within cells [103]. It is necessary that users understand the complexity of the sample and sample environment to determine which imaging flow cytometry approach, camera-based or PMT based method, best suits their needs.

Recent studies with imaging flow cytometry have been performed with white blood cells to classify them by type, rather than solely by cell cycle [104], [105]. Imaging flow cytometry has also been used to assess nano-bio interactions. For example, Vranic *et al*. used imaging flow cytometry to identify the time- and dose-dependence of TiO_2 and SiO_2 nanoparticle interactions with NCI-H292 human pulmonary epithelial cancer cells. During this analysis, the researchers discovered that the endocytosis pathway for

SiO_2 was micropinocytosis through visually tracking cell features following endocytosis pathway inhibition and nanoparticle treatment [45]. Interestingly, a majority of recent imaging flow cytometry studies have focused on the analysis of extracellular vesicle interactions with cells, and the delivery of EVs to cells (Figure 2D-2E) [48], [74], [106]–[111]. We attribute this trend to the growing interest in the use of EVs for therapeutic cargo delivery and the assessment of cellular senescence and aging [112]–[115]. For instance, Görgens *et al*. analyzed the interactions of EVs and small EVs that were derived from THP-1 human cancer cells with THP-1 cells after labeling the EVs with CD63eGFP. The researchers reported that EVs and small EVs could also be detected in unprocessed samples. Their findings, therefore, will allow for an easier analysis of EVs and their interaction with cells without the need to isolate the EVs from cells.

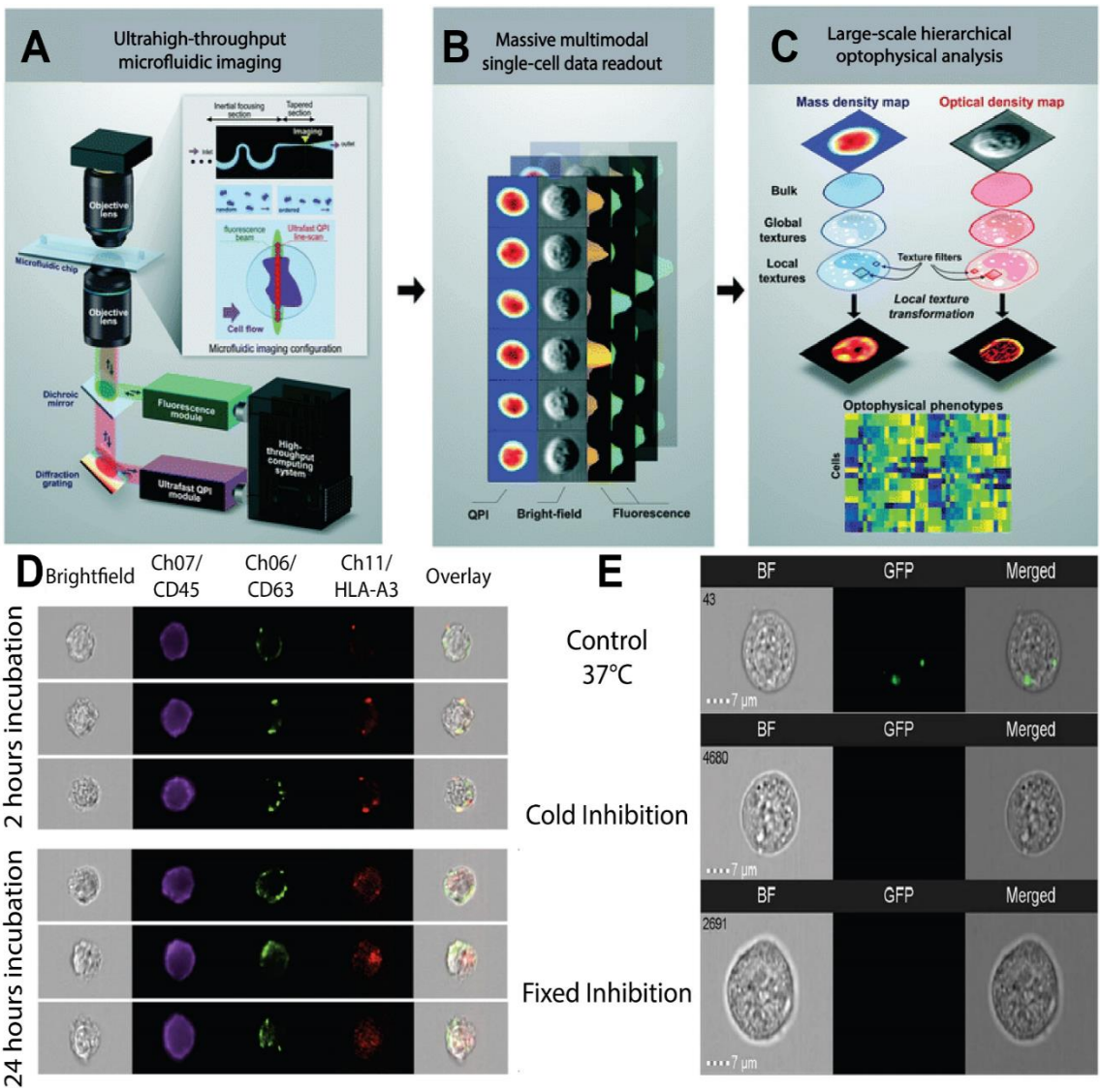

Figure 2: Imaging flow cytometry workflow and data of nanoparticle-cell interaction. (A) The general workflow of an imaging flow cytometer. A fluorescence and a quantitative phase image (QPI) module are used for image acquisition of the sample flowing through the microfluidic chip. **(B)** Once the sample is run through and the cells have been aligned through the chip's single stream, 2D images of single cells in suspension are reconstructed. **(C)** Once the images are reconstructed, they are used for analyses that integrate the correlation between different cell-type classifications. Reproduced with permission from reference [99]. Copyright 2023 Lab on a Chip. **(D)** Using a similar workflow, images of HLA-A3 human cells were incubated with extracellular vesicles for

various periods of time, i.e., 2 hours vs. 24 hours. Images of the different conditions are shown. Reproduced with permission from reference [116]. **(E)** Representative imaging flow cytometry images of HEK293T extracellular vesicle interactions with HEK293T human cells at different conditions, i.e., at 37˚C, 4˚C. Reproduced with permission from reference [47]. Copyright 2023 Springer Nature.

Imaging flow cytometry does have its limitations. The cell sorting capability of imaging flow cytometry sorting capability is very limited. This is because creating an image-based cell sorter requires major enhancements in high-speed image acquisition, as well as the need to incorporate microscale sorting modules and intelligent data analysis methods [102], [117]–[119]. Moreover, it is not feasible to reimage the same cell, as it would be if the cells were imaged using time-lapse slide-based microscopy. This limitation denies the possibility of implementing 3D reconstruction of cells or confocal sectioning (i.e., z-stacking). In addition, there is a lack of workflow automation in imaging flow cytometry. This can lead to significant challenges in downstream analyses as, for example, dozens of masks need to be applied to cellular objects and subcellular compartments for complete analysis [102]. Tracking of cell samples as they flow through the microfluidic chamber for temporal snapshot analysis has yet to be achieved [102]. Finally, imaging flow cytometry data analysis is intensive, requiring manual inspection of images coinciding with scattering data. Scaling experiments to align with reasonable data analysis approaches remains a challenge in imaging flow cytometry methods.

Even with these challenges, imaging flow cytometry advantages are multifold. Imaging flow cytometry uses a sensitive CCD camera that allows for the identification of pixels that have higher signals than their surroundings and provides a better resolution than that of conventional flow cytometry [48]. Additionally, with the imaging processing tools available for imaging flow cytometry, identification of coincidental data is possible, a phenomenon unattainable with conventional flow cytometry [110]. Furthermore, in terms of extracellular vesicle analysis, the slower

flow rate of imaging flow cytometry paired with CCD-camera based detection allows for a more effective extracellular vesicle analysis platform compared to conventional flow cytometry [108]. It is also worth noting that imaging flow cytometry instruments have low background, an increased fluorescence sensitivity, and great data analysis tools that can incorporate machine learning algorithms [74].

Beyond these advantages, recent developments in imaging flow cytometry have sought to overcome the previously discussed challenges. For example, studies using digital holography have generated tomographic flow cytometry, allowing for collection of 3D information of target particles [120], [121]. Recent studies have aimed to develop machine and deep learning algorithms to train models for evaluating and classifying imaging flow cytometry images (Figure 3), providing improved analysis workflows [105], [122], [123]. Also, future improvements can be done to remove the snapshot limitations, in which images of the cell sample are taken as the cell passes specific points in the microfluidic channel, and implement object or sample tracking [102], [121], [124]. It is worth noting that a virtual-freezing fluorescence imaging flow cytometry method has been developed to allow for a longer exposure time for image acquisition, thus, facilitating high-throughput imaging flow cytometry of >10,000 single cells per second without losing spatial resolution or sensitivity [125].

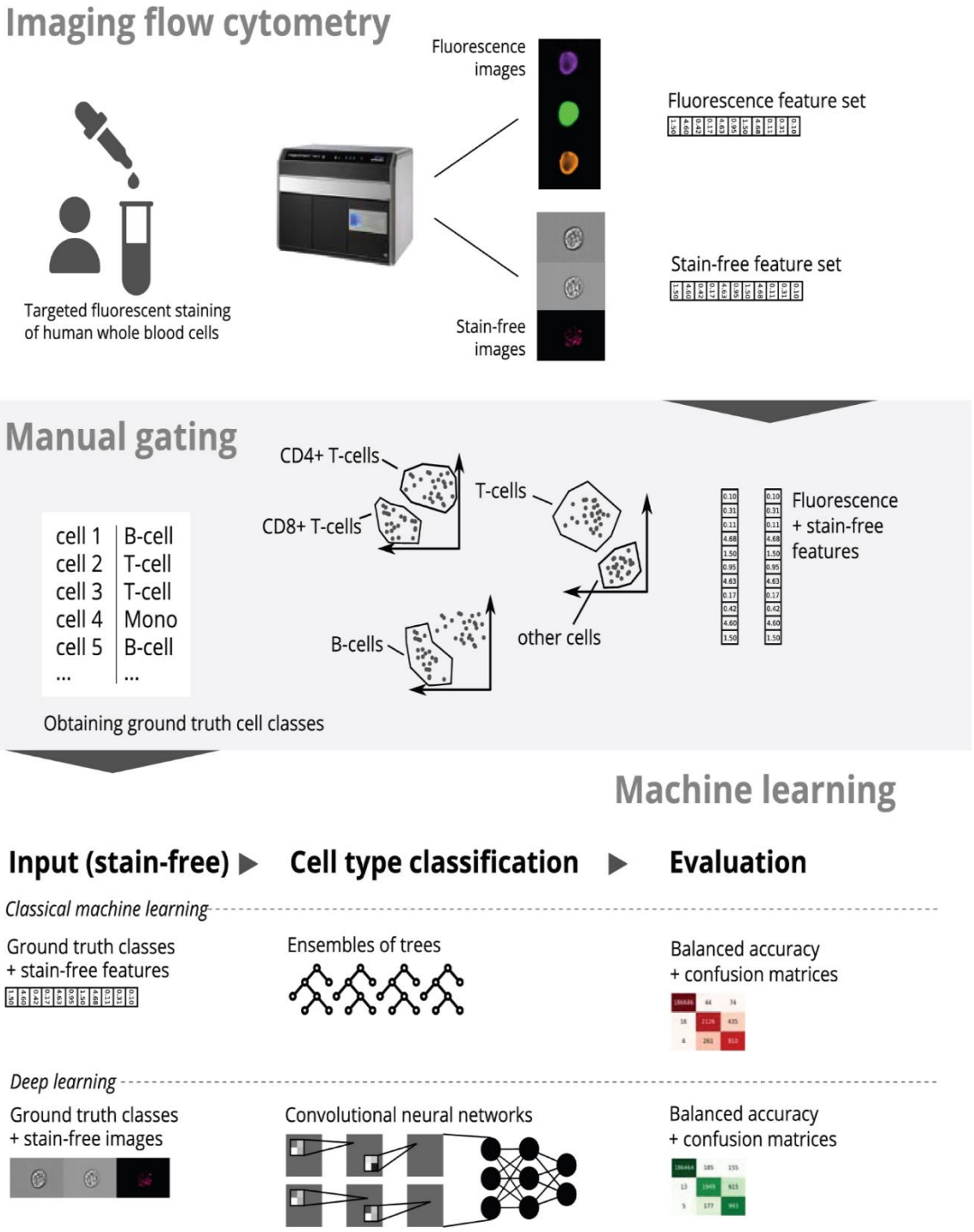

Figure 3: Data processing techniques for imaging flow cytometry. Machine learning algorithms and deep learning models are utilized for the evaluation and classification white blood samples from healthy donors. Reproduced with permission from reference [105]. Copyright 2023 Cytometry Part A.

1.3.5 Photoacoustic Flow Cytometry

Conventional flow cytometry approaches have been paired with photoacoustic technology to produce photoacoustic flow cytometry (PAFC) and photoacoustic imaging flow cytometry [49]. The PAFC system is comprised of five main components: a transducer, a laser, a microscope, a flow tank, and a pump system (Figure 4A-4C) [50], [126]. The pump system shuttles cells into a capillary tube where the cells are irradiated by a laser. The cells absorb laser light and generate an acoustic wave that is detectable by the transducer. The microscope correlates the firing rate of the laser and the sample passage with the acoustic signal recorded by the transducer. Transducer signals are sent to an ultrasound receiver, where they are amplified for data collection. Scanners can be implemented to record images of cells as they move through the microfluidic systems [53].

Specifically, a diode-pumped pulsed laser is used for photoacoustic (PA) excitation. Once excited, the acoustic waves are collected, and separated from the excitation light using a couple of dichroic mirrors and a bandpass filter. The transducer then detects photoacoustic events in the flow chamber [53], [127]. The intensity of the collected photoacoustic signal is then measured using a photomultiplier tube connected to a high-voltage pre-amplifier. The PA signals are then amplified and digitized. Recorded amplitudes of PA signals along with voltage signals from photomultiplier tube are recorded and compared [128], which is possible due to the setup of the flow chamber allowing for the collection of excitation and acoustic wave [129].

PAFC has been used to characterize nanoparticle interactions with cells. Nedosekin *et al*. quantified interactions of antibody-labeled gold nanorods with MDA-MD-231-GFP human and ZR-57-1 human breast cancer cells, whereby photoacoustic signal from cells

treated with the gold nanorods increased by nearly two orders of magnitude compared to controls [51]. Cells labeled with nanoparticles have also been observed using PAFC, such as in a study by Bhattacharyya *et al*. where T47D breast cancer cells were labeled with fluorescent latex nanoparticles [52]. Sun *et al*. used multiparametric PAFC (MPAFC) to successfully identify three different cell lines – 9L mouse cells, HeLa cervical cancer cells, and C6 mouse cells – labeled with three different polymer nanoparticles in simulated blood while, eliminating cross-labeled or label-free cells from analysis (Figure 4D) [130].

PAFC is capable of detecting nanoparticles at a high sensitivity and characterizing cells without compromising the light scattering and fluorescence detection of various biomarkers. However, PAFC can experience deterioration of imaging power due to a majority of suspended cells being distributed out of the focal plane as a result of limited axial resolution and depth of field [45], [51]. However, these limitations can be overcome by the introduction of an acoustic standing wave, which helps confine the suspension cells to the focal plane of the illumination, thus avoiding any effect from the limited axial resolution and depth of field [130]. Implementation of point-to-point scanning can lead to a low throughput and decreased imaging speed. Moreover, the wavelengths of lasers with high pulse repetition rates are restricted, meaning only an exclusive selection of chromophores can be distinguished by the two-color illumination scheme [130], [131].

Innovation in PAFC has produced promising advancements. PAFC analysis speed can be significantly increased as data processing algorithms are implemented [75]. PAFC has medium in place of a flow tank or pump system [132]–[134]. Flow

cytometry techniques are generally limited in *ex vivo* analysis, for example demonstrating low sensitivity while detecting circulating tumor cells, in addition to requiring intensive sample preparation and data analysis methods [75], [135]. Using *in vivo* flow cytometry via PAFC has allowed for the detection of fluorescently labeled low abundance circulating tumor cells directly in the blood of mice [136]. For instance, Yao *et al*. used *in* vivo flow cytometry to study the ability of nanoparticles to target circulating tumor cells. The authors found that fluorescently labeled polymer nanoparticles coated with neutrophil members could more efficiently target circulating tumor cells compared to uncoated nanoparticles [60]. Several studies have used similar *in vivo* approaches to assess how nanoparticles affect blood flow and cells in the blood, such as circulating tumor cells and melanoma cells [52], [54], [57], [61].

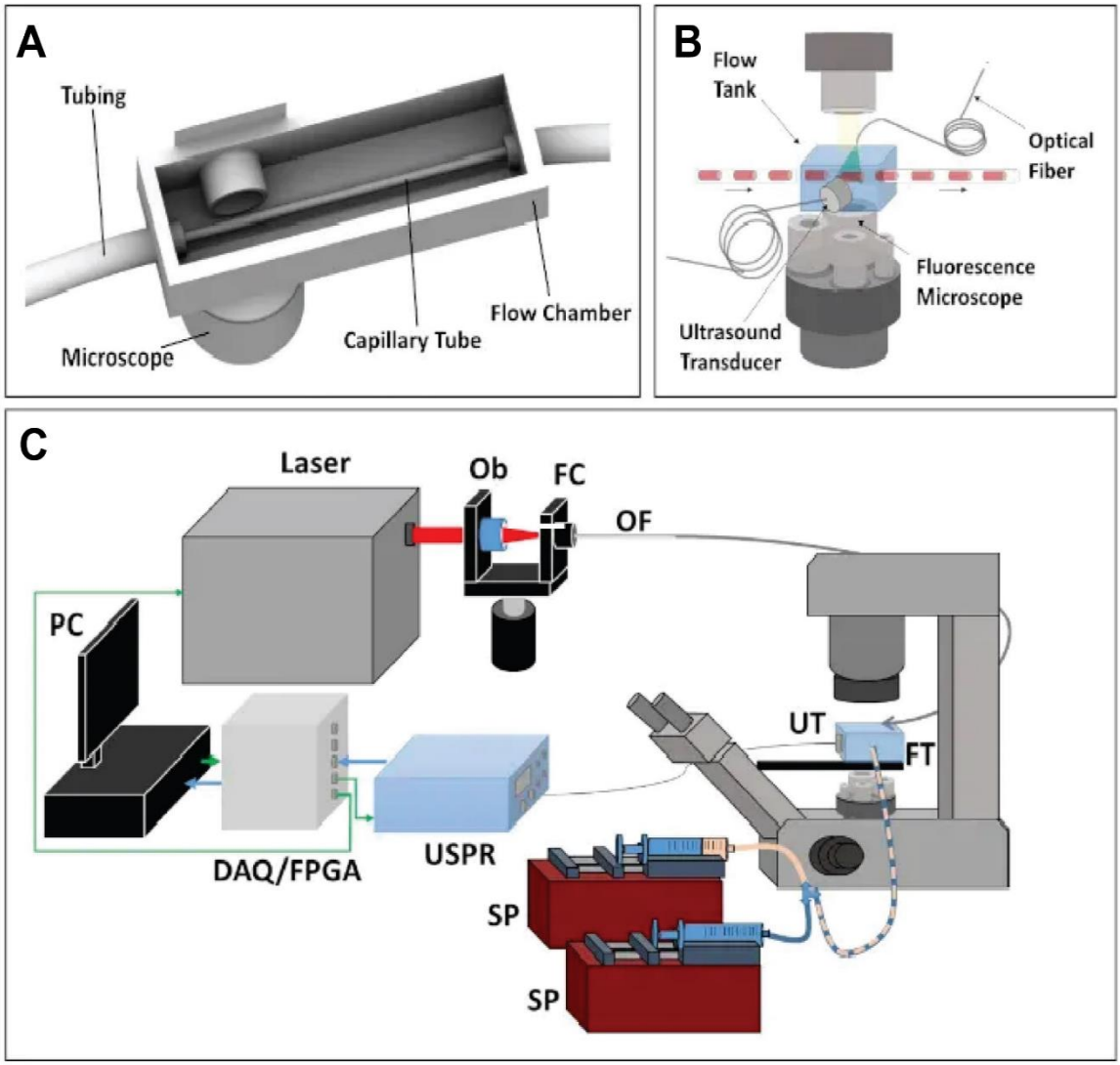
A
Tubing
Microscope
Capillary Tube
Flow Chamber
B
Flow
Tank
Optical
Fiber
Fluorescence
Microscope
Ultrasound
Transducer
C
Laser
Ob
FC
OF
PC
UT
FT
USPR
DAQ/FPGA
SP
SP
D
Tumor cell-CNPPV
Tumor cell-BDT-TQE
Tumor cell-SP2
Blood cell
Melanoma cell
i
532 nm
ii
770 nm
iii
30 μm

Figure 4: Photoacoustic imaging flow cytometry (PAIFC) for the identification of nanoparticle interactions with cells. (A) Diagram of the different components of a photoacoustic imaging flow cytometer. The single cell sample flows through the flow chamber. **(B)** Components of the photoacoustic flow cytometer system. **(C)** The components of a PAIFC system. SP = syringe pump; DAQ/FPGA = data acquisition/field programmable gate array; Ob = objective lens; OF = optical fiber; FC = fiber coupler; UT = ultrasound transducer; FT = flow tank. Adapted with permission from reference [49]. Copyright 2023 Journal of Visualized Experiments. **(D)** Multiparametric photoacoustic flow cytometer is used to analyze C6 (green), HeLa (blue), and 9L (orange) cells that were labeled with SP2, BDT-TQE, and CNPPV polymer nanoparticles, respectively, is shown. The maximum amplitude projection (MAP) images of labelled tumor cells at **(i)** 532 and **(ii)** 770 nm respectively. **(iii)** The PAIFC could identify the cells using the photoacoustic wavelengths generated by each cell Adapted with permission from reference [130]. Copyright 2023 American Chemical Society.

Chapter 2

Introduction

Even within single cell lines, individual cells still behave heterogeneously [137], [138]. As a result, single-cell analysis is necessary to be able to study the behavior of individual cells and their interactions with nanoparticles [139]. Understanding those interactions will allow for enhanced nanomedicine and ultimately improved clinical trials and results, as currently only 0.7% of administered nanoparticles reach the tumor microenvironment [140]. Therefore, a better understanding of nano-bio interactions is needed to improve the delivery of nanoparticles to tumors and subsequently improve the clinical translation of nanomedicine.

Current methods to analyze nano-bio interactions at the single-cell level, include but are not limited to inductively coupled plasma mass spectrometry (ICP-MS) and microscopy [25], [139], [141]. Despite the fact that ICP-MS allows for a high throughput method of analysis and microscopy for visualization of these interactions, ICP-MS is labor-intensive, while tagging nanoparticles (NPs) for microscopy for instance, changes the surface chemistry of these NPs, hence the way they interact with cells [25], [142]–[147]. This change in nano-bio interactions as well as the degree of nanoparticle uptake is demonstrated in Roussel *et al*'s paper [148]. The authors found out that fluorescence type can change the amount of nanoparticle internalization within the cells, and that the fluorescent tag is not internalized in a similar manner to that of the nanoparticles. Similarly, Rodriguez-Lorenzo *et al* found out that the cellular uptake of unlabeled nanoparticles was significantly reduced upon the addition of a fluorescent label [147].

Due to such disadvantages, we aimed to use a method that allows for label-free analysis and is not labor-intensive. For that reason, we used flow cytometry (FCM) as a technique to analyze nanoparticle-cell interactions at the single-cell level. Flow cytometry is a high-throughput method that allows for tens of thousands of particles to run per second [149]. Moreover, FCM can be used to provide diagnostic information on cancer cells, as well as an estimation of the amount of NP uptake and their potential cellular toxicity, thus enhancing the field of cancer nanomedicine [150].

In this study, we aimed to establish flow cytometry as a label-free technique for the analysis of nanoparticle-cell interactions by performing various cell uptake experiments using different nanoparticle systems. To validate the data obtained from flow cytometry, we used confocal laser scanning microscopy (CLSM), as well as ICP-MS to compare the flow data and support the trends seen via FCM. The light scattering intensity using CLSM was compared to the increase in side scattering (SSC) signal measured by flow cytometry. Additionally, the amount of gold nanoparticles (AuNP), specifically AuNP/cell were measured and calculated using ICP-MS and compared as well to the increase in the SSC signals. Considering the SSC is necessary to understand the nano-bio interactions using a label-free way, as SSC correlates to the granularity or complexity of the cells [151], [152]. SSC signal is an indication to how nanoparticles affect cells upon cellular uptake of NPs. The greater the uptake and the larger the size of the NPs, the greater the complexity of organelles within a cell becomes, and the higher the SSC signal becomes [30], [152], [153]. Understanding such characteristics as well as the kinetics of and the extent to which NPs are uptaken by cells is the goal of this study.

Experimental Methods

This section shows the methods and materials used to perform the various experiments in this thesis. These methods include nanoparticle synthesis, addition of surface modifications, and sample preparation and data collection. Figure 20 in the Appendix illustrates the general experimental setups used across the different experiments.

1. Gold nanoparticle synthesis (40 nm, 65 nm or 100 nm)

Aqua regia was used to clean the glass flasks before synthesis. The aqua regia solution is prepared as a 3:1 ratio of hydrochloric acid (Sigma-Aldrich, ACS reagent, 37%) to nitric acid (Sigma-Aldrich, ACS reagent, 70%).

Synthesis of 40 nm gold nanoparticles

To synthesize nanoparticles larger than 14 nm, a seed-mediated synthesis protocol was adopted from Perrault *et al* [154]. 14 nm seed gold nanoparticles without Tween 20 were prepared according to Turkevich *et al*'s protocol [155]. The solutions were added in the following order to synthesize the 40 nm AuNPs, at a stirring speed of ~400 rpm: 92.405 mL of nanopure water, 0.942 mL of 25 mM aqueous gold (III) chloride trihydrate, 0.942 mL of 15 mM aqueous sodium citrate tribasic dihydrate, 4.769 mL of citrate-stabilized 2.4 nM 15-nm gold nanoparticles (without the addition of Tween 20), and 0.942 mL 25 mM aqueous hydroquinone (Sigma-Aldrich, ReagentPlus, ≥ 99.0%). The solution turned from light pink to dark red right after the addition of hydroquinone. After the overnight reaction, 1 mL 10% Tween 20 (v/v) was added for a final ~0.1%

concentration. Nanoparticles were centrifuged at 2500 x g for 180 minutes and then the supernatant was discarded. Pellets were resuspended in 0.1% (v/v) Tween 20, 0.01% (w/v) sodium citrate tribasic dihydrate solution (NP wash buffer) and centrifuged again at 2500 x g for 30 minutes. The supernatant was removed gain and the nanoparticles were then dispersed in NP wash buffer. This was followed by measuring both concentration and hydrodynamic diameter by UV-VIS spectrophotometry and DLS, respectively. The nanoparticle dispersion was stored at 4°C until further use.

Synthesis of 65 nm and 100 nm gold nanoparticles

Similar to what was mentioned earlier, and following the same protocol, to synthesize 65 nm AuNPs, 95.705 mL of nanopure water, 0.961 mL of 25 mM aqueous gold (III) chloride trihydrate, 0.961 mL of 15 mM aqueous sodium citrate tribasic dihydrate, 1.411 mL of citrate-stabilized 2.4 nM 15-nm gold nanoparticles (without the addition of Tween 20), and 0.961 mL 25 mM aqueous hydroquinone (Sigma-Aldrich, ReagentPlus, ≥ 99.0%) were added to a clean flask and stirred at ~400 rpm. The centrifugation speed used for 65 nm AuNPs was 1200 x g. As for 100 nm AuNPs, 97.6 mL of nanopure water, 99.7 μL of 25 mM aqueous gold (III) chloride trihydrate, 0. 997 mL of 15 mM aqueous sodium citrate tribasic dihydrate, 0.305 mL of citrate-stabilized 2.4 nM 15-nm gold nanoparticles (without the addition of Tween 20), and 0.997 mL 25 mM aqueous hydroquinone (Sigma-Aldrich, ReagentPlus, ≥ 99.0%) were added together in the respective order. The 100 nm AuNPs were centrifuged at 750 x g at 4˚C.

2. Silver nanoparticle synthesis (30 nm)

Aqua regia was used to clean the glass flasks before synthesis. The aqua regia solution is prepared as a 3:1 ratio of hydrochloric acid (Sigma-Aldrich, ACS reagent, 37%) to nitric acid (Sigma-Aldrich, ACS reagent, 70%).

Synthesis of 30 nm silver nanoparticles

To synthesize silver nanoparticles, a protocol similar to the one published by Rainville et al was followed [156]. 31.48 mg of sodium citrate tribasic dihydrate and 4.93 mg of tannic acid (Sigma-Aldrich) were needed to synthesize a core diameter of 30 nm silver nanoparticles. The masses of sodium citrate and tannic acid were weighed out. In order to determine which solution will yield the highest volume, the required volume of nanopure water to dissolve the chemicals was calculated. A concentration of 12.2 mM and 290 μM of sodium citrate and tannic acid, respectively, are needed for the synthesis. Once the solution with the highest volume was determined, the appropriate amount of nanopure water was added and the solution was vortexed. Then to dissolve the second solution, the appropriate volume was taken from the first solution and was used to dissolve the former. The combined solution of tannic acid, sodium citrate and nanopure water was vortexed. In case the final volume is greater than 10 mL, the excess volume is removed in order to reach a volume of 10 mL.

9 mg of silver nitrate (Sigma-Aldrich) was weighed out. This was dissolved in 40 mL of nanopure water, and the solution was vortexed. The two solutions of silver nitrate and tannic acid + sodium citrate was placed in the water bath for 15 min at a

temperature of 60 °C. After the 15 min are over, tannic acid + sodium citrate solution was added first to the flask which was placed on a stir plate and was combined with the silver nitrate under vigorous stirring once at 60 °C for 5 min. This was followed by a temperature increase to ~180˚C. Once the solution started boiling, a 20 min timer was set and then the reaction was ended. The flask was removed from the stir plate and was left on a bench away from the light to cool down until it reached room temperature. The 33 nm silver nanoparticles were then transferred into a 50 mL tube and the solution was characterized for both hydrodynamic diameter and concentration using DLS and UV-VIS spectrophotometry.

In order to characterize the concentration, the extinction coefficient was calculated based on Paramelle *et al'*s paper [157]. Then this extinction coefficient was used to determine the concentration of the 30 nm AgNPs. The solution was stored in a drawer away from the light at room temperature.

To clean the flask after the synthesis, 100 mL nitric acid was added to the flask. The flask was then placed on a hot plate at 100°C for 30 min, and then was left in the hood overnight. The acid was then disposed of in the acid waste and the flask was then rinsed a few times with DI water, followed by another few washes of nanopure water.

3. PEGylation of gold and silver nanoparticles

PEGylation of gold nanoparticles

Hydrodynamic diameter was first measured on the DLS. A PEG density of 7 PEG/nm^2 is desired to backfill any desired volume of NPs and 10 kDa mPEG-OPSS (Laysan Bio

Inc) was used to achieve that. Mass was weighed out and the PEG was dissolved in the appropriate amount of nanopure water to reach a concentration of 1 mM. Once the PEG was dissolved, it was added to the NP solution and was quickly vortexed. Then the solution of NPs and PEG were left in room temperature for 30 minutes. Following these 30 minutes, a 30 min centrifugation at 4˚C and 750 x g was done to the PEGylated-AuNP solution. The supernatant was removed, and the PEG-coated NPs were resuspended in 0.1% (v/v) Tween 20, 0.01% (w/v) sodium citrate tribasic dihydrate solution, and then stored at 4˚C, after measuring the concentration and hydrodynamic diameter using UV-VIS spectrophotometry and DLS, respectively.

PEGylation of silver nanoparticles

5 kDa mPEG-SH (Laysan Bio Inc) was used for the surface coating of the silver nanoparticles and the same protocol was followed. The centrifugation speed used for the 30 nm AgNPs was 7500 x g.

4. HEPylation of AuNPs prepared by the pH method

Heparosan-coated 100 nm AuNPs were synthesized using the pH method as described by Yang *et al* [158], [159]. Briefly, 13.3 kDa HEP-OPSS was mixed with dilute HCl solution of a pH of 3.0. The solution was then mixed with citrate-coated AuNPs and was incubated at room temperature (RT) for 5 min. Saline was added to the solution to reach a final concentration of 0.3 M and then was incubated at RT for 20 min. More NaCl was added to the solution to reach a final concentration of 0.7 M. To

get rid of any excess HEP and NaCl, the NPs were centrifuged thrice at 7750 x g for 30 min at 4˚C, and after removing the supernatant, the pellet was resuspended in 0.1% Tween 20 + 0.01% citrate solution.

5. Confocal characterization of nanoparticle cellular uptake (fixed cell imaging)

Cellular uptake experiment

RAW 264.7 macrophages or 4T1 were seeded onto sterile glass coverslips, which were covered with gelatin at a concentration of 2 mg/mL and placed into a 12 well-plate for 20-24 hours with DMEM culture media supplemented with 10% fetal bovine serum and 1% Penicillin-Streptomycin. The cell media was removed the next day, and the cells were treated with 0.216 nM PEG-coated 100-nm gold nanoparticles for 24 hours. Cells were washed thrice with 1X PBS to remove noninternalized gold nanoparticles. Cells were fixed by 4% paraformaldehyde (4% PFA, ThermoFisher) at room temperature for 10 minutes. Fixed cells were stained with wheat germ agglutinin CF488A (WGA, Biotium) and NucBlue fix cell DAPI (ThermoFisher) according to the manufacture's protocols to label the cell surface or the nuclei, respectively. Confocal images were taken with a 63X oil immersion objective (1.4 NA) on a ZEISS LSM 880 inverted confocal microscope using photomultiplier tube (PMT) detectors with a 405 nm diode laser and a 488 nm argon laser for fluorescent channels through a main beam splitter (MBS) 488/561/633 filter. The nanoparticles were imaged using light scattering principles described by Jiang *et al* [160] with a 561 nm diode-pumped solid-state laser and an MBS T80/R20 filter.

For 40 nm AuNPs and 30 nm AgNPs, a concentration of 40 pM was used, while a concentration of 1 nM was used for the 65 nm AuNPs.

Kinetics analysis experiment

The same protocol was followed as mentioned earlier. However, the samples were fixed at different time points, stored after being fixed at 4˚C, and were then all stained with wheat germ agglutinin CF488A (WGA, Biotium) and NucBlue fix cell DAPI (ThermoFisher) according to the manufacture's protocols to label the cell surface or the nuclei, respectively.

Endocytosis inhibition experiment

After covering the coverslips with gelatin, RAW 264.7 macrophages were seeded onto the coverslips and left overnight to proliferate.

To determine what effect surface modification has on the cellular uptake, cells were incubated at 37˚C for with 0.2 nM 100 nm 10 kDa mPEG-OPSS and 0.2 nM 100 nm 13.3 kDa HEP-AuNPs for 1.5 hrs.

To determine what effect low temperature has on the cellular uptake, cells were incubated at 4˚C for 1 hr, then 0 0.2 nM 100 nm 13.3 kDa HEP-AuNPs were added for another 1.5 hrs at 4˚C. Parallel plates of cells were incubated at 37ºC for the control.

To investigate the chemical effect of endocytic inhibitors on cell uptake, a process similar to Okuyama *et al* [161] was followed. After leaving the seeded cells overnight

to proliferate, inhibitors were added to cells for 1 hr. Then 0.2 nM 100 nm 10 kDa mPEG-OPSS and 0.2 nM 100 nm 13.3 kDa HEP-AuNPs, which were diluted in media, were added for another 1.5 hrs. Cells without any inhibitors were used as a control.

After the 1.5 hr incubation with the nanoparticles, the cells were washed thrice with 1x PBS, then were fixed using 4% PFA for 10 min at room temperature. This was followed by staining of the samples using germ agglutinin CF488A (WGA, Biotium) and NucBlue fix cell DAPI (ThermoFisher). Samples were stored at 4˚C until they were imaged.

Cell recovery experiment

Coverslips were cleaned using piranha solution and were then covered with gelatin. RAW 264.7 macrophages were seeded onto the coverslips and were left overnight to proliferate.

To determine how fast cells can recover from the effect of the inhibitors, we used the same inhibitors as in the endocytosis inhibition experiment, i.e., chlorpromazine, Cytochalasin D, Filipin, Sodium Azide and incubation at 4˚C. This time, we incubated the cells with inhibitors for 1 hr, and then the cells were incubated only with 0.2 nM 100 nm 13.3 kDa HEP-AuNPs for 1.5 hrs. Regarding the 4˚C condition, the cells were stored in the fridge for 1 hr, and then 0.2 nM 100 nm 13.3 kDa HEP-AuNPs were added and the well-plate was then stored again in the fridge for the next 1.5 hrs.

After the 1.5 hr incubation with the nanoparticles, the cells were washed thrice with 1x PBS, then were fixed using 4% PFA for 10 min at room temperature. This was followed by staining of the samples using wheat germ agglutinin CF488A (WGA,

Biotium) and NucBlue fix cell DAPI (ThermoFisher). Samples were stored at 4˚C until they were imaged.

6. Batch ICP-MS characterization of cellular uptake and kinetics analysis experiment

Cellular uptake experiment

This protocol was followed by previously published methods in our laboratory [71]. RAW 264.7 macrophages were purchased from ATCC. First, a total of $1.2x10^6$ cells were seeded onto a 48-well plate and allowed to adhere for 22-24 hours. The old media was aspirated and replaced with 500 μL of new media which consists of 1.982 mL of DMEM + FBS + pen/strep and 118 μL of nanoparticles. The cells and the NPs were then incubated at 37°C (5% CO_2) in a humidified tissue culture incubator for 24 hours. After incubation with nanoparticles, cells were washed with 1X PBS thrice to remove non-internalized nanoparticles.

Purified cell samples were then digested by adding 500 μL of 4:1 nitric acid : hydrochloric acid directly into the wells. After 30 min, acid-digested samples were transferred to 1.5 mL microcentrifuge tubes and placed in a water bath at 70°C for 1 hr to complete the digestion process. Samples were then allowed to cool and then diluted 40-fold in iridium water with a final volume of 5 mL. All elemental analysis measurements for nanoparticle uptake were done using the PerkinElmer NexIon 2000 ICP-MS on the Prepfast IC Sample Introduction system at the Mass Spectrometry, Proteomics, and Metabolomics Core Facility, University of Oklahoma. In order to

determine the number of nanoparticles per cell, dissolved gold signals were correlated to the magnesium signals from known numbers of cells. The data were analyzed on GraphPad Prism with three or four replicates.

Kinetics analysis experiment

The same protocol was followed as mentioned earlier. First, a total of 1.44 $x10^7$ cells were seeded onto six 48-well plates and allowed to adhere for 22-24 hours. The old media was aspirated and replaced with 300 μL of new media which consists of 4.796 mL of DMEM + FBS + pen/strep and 204 μL of nanoparticles. The cells and the NPs were then incubated at 37°C (5% CO_2) in a humidified tissue culture incubator for 24 hours. Specific incubation times and nanoparticle concentrations are noted in the figure captions along with each experiment result.

The rest of the digestion process was done in a similar manner to what was mentioned above.

7. Flow cytometric characterization of nanoparticle cellular uptake, kinetics analysis and energy dependent temperature and transport inhibition experiments

Cellular uptake experiment

For the 100 nm AuNP uptake experiment, a total of $5x10^4$ RAW 264.6 macrophages were seeded onto 12-well plate and allowed to adhere for 22-24 hours. The old media was aspirated and replaced with 500 μL of new media which consists of 1.514 mL of DMEM + FBS + pen/strep and 59 μL of nanoparticles, to reach a concentration of 0.216 nM. The

cells and the NPs were then incubated at 37°C (5% CO_2) in a humidified tissue culture incubator for 24 hours. After incubation with nanoparticles, cells were washed with 1X PBS thrice to remove non-internalized nanoparticles.

In a separate well plate, 4T1 cells were seeded at a density of $5x10^4$ cells in a 12-well plate and left for 22-24 hours to adhere and proliferate. The old media was aspirated and replaced with 500 µL of new media which consists of 1.062 mL of DMEM + FBS + pen/strep and 38 µL of nanoparticles, to reach a concentration of 0.216 nM.

When performing the experiment with 40 nm AuNPs and 30 nm AgNPs, a concentration of 40 pM diluted in DMEM + FBS + pen/strep for the NP uptake. 13.8 µL of 30 nm AgNPs were diluted in 1.636 mL of media, whereas 19.3 µL of the 40 nm AuNPs was diluted into 1.632 mL of media. The rest of the incubation process and seeding density were the same.

60 nm AuNPs were incubated with the cells at a concentration of 1 nM. 852 µL of the NPs were diluted in 1.748 mL of media.

After washing the cells with 1x PBS to remove the non-internalized NPs, 1 mL of media was added to each well, and the cells were scraped. Cells were then transferred into FACS tubes and centrifuged at 500 x g for 5 min at 10˚C. The supernatant was then removed, and the pellet was then resuspended into 300 µL of 1x PBS then the samples were analyzed using flow cytometry. 5000 events were recorded on Cytek Northern Lights found in Gallogly Hall at the University of Oklahoma., and the gain parameters used for RAW 264.7 macrophages were 30, 40 and 137 for FSC, SSC and

SSC-B, respectively. As for the 4T1, 15, 25 and 112 gain parameters were used for the FSC, SSC and SSC-B, respectively.

A gating strategy was used, and it can be seen in Figure 12.

Kinetics analysis experiment

RAW 264.7 macrophages were seeded onto seven 24 well-plates and were left for 20-24 hours to proliferate. Each time point has its own well-plate. Five different concentrations of 100 nm AuNPs at a volume of 300 μL were used: 0.1 nM, 0.04 nM, 0.02 nM, 0.0133 nM, and 0.01 nM. Those were all diluted using DMEM + FBS + pen/strep. The different time points used throughout the experiment were: 0, 1, 2, 4, 6, 8, and 24 hours of incubation. After each time point, the samples were washed with 1x PBS to remove the non-internalized NPs. Then, 1 mL of media was added to each well, and the cells were scraped. Cells were then transferred into FACS tubes and centrifuged at 500 x g for 5 min at 10˚C. The supernatant was removed, and the cells were fixed using 4% PFA for 10 min on ice. After the 10 min, the cells were centrifuged again at 500 x g for 5 min at 10˚C, the supernatant was removed, and a wash using 1 mL of 1x PBS per sample was done to get rid of any leftover PFA. After adding 1x PBS, the cells were centrifuged, the supernatant was removed and 200 μL of 1x PBS was used to resuspend the pellet of fixed cells. The samples were stored in the fridge at 4˚C.

The samples were then analyzed through flow cytometry at the end of the last time point. The same gain parameters as mentioned earlier were used, and the number of events recorded was 10,000.

Energy dependent temperature and transport inhibition experiment

RAW 264.7 macrophages were seeded onto two 48 well-plates and were left overnight to proliferate. 100 nm AuNPs were used at a concentration of 0.2 nM.

To determine what effect surface modification has on the cellular uptake, cells were incubated at 37˚C with 0.2 nM 100 nm 10 kDa mPEG-OPSS and 0.2 nM 100 nm 13.3 kDa HEP-AuNPs for 1.5 hrs.

To determine what effect low temperature has on the cellular uptake, cells were incubated at 4˚C for 1 hr, then 0 0.2 nM 100 nm 13.3 kDa HEP-AuNPs were added for another 1.5 hrs at 4˚C. Parallel plates of cells were incubated at 37ºC for the control.

To investigate the chemical effect of endocytic inhibitors on cell uptake, a process similar to Okuyama *et al* [161] was followed. After leaving the seeded cells overnight to proliferate, inhibitors were added to cells for 1 hr. Then 0.2 nM 100 nm 13.3 kDa HEP-AuNPs, which were diluted in media, were added for another 1.5 hrs. Cells without any inhibitors were used as a control.

Following the 1.5 hr NP incubation with the cells, the cells were washed thrice with 1x PBS. Zombie dye viability assay was added to the samples and incubated at room temperature in the darkness for 15-30 min. Samples were then washed with a cell staining buffer (BioLegend, Cat. No. 420201).Then, 400 µL of 1x PBS was added to each well, and the cells were scraped. Cells were then transferred into FACS tubes and centrifuged at 500 x g for 5 min at 10˚C. The supernatant was removed, and the cells were fixed using 4% PFA for 10 min on ice. After the 10 min, the cells were centrifuged again at 500 x g for 5 min at 10˚C, the supernatant was removed, and a wash using 1

mL of 1x PBS per sample was done to get rid of any leftover PFA. After adding 1x PBS, the cells were centrifuged, the supernatant was removed and 200 µL of 1x PBS was used to resuspend the pellet of fixed cells. The samples were stored in the fridge at 4˚C.

The samples were then analyzed through flow cytometry at the end of the last time point. The same gain parameters as mentioned earlier were used, and the number of events recorded was 10,000 events.

8. Single particle ICP-MS (SP-ICP-MS) characterization

Single-particle inductively coupled plasma mass spectrometry (SP-ICP-MS) measurements were carried out based on published methods [162]–[164]. Briefly, AuNPs were diluted to ~3x10-16 M using nanopure water. A PerkinElmer NexIon 2000 with a microfluidic sample introduction system was used to measure the mass of individual particles in solution, creating a measured mass distribution for each particle population measured. Prior to sample measurement, the transport efficiency was measured using Lu175-doped 3 µm polystyrene beads (Fluidigm). Transport efficiency values vaired between 50-70% based on environmental conditions. Additionally, a particle calibration curve was measured for each element being analyzed (Au or Ag) using synthesized nanoparticle standards whose diameter was previously quantified using TEM.

The following nanoparticles were characterized using SP-ICP-MS: 13.3 kDA HEP-coated 100 nm AuNPs, 10 kDA OPSS-mPEG-coated 100 nm AuNPs, citrate-coated 100 nm AuNPs, 10 kDA OPSS-mPEG-coated 65 nm AuNPs, 10 kDA OPSS-mPEG-coated 40 nm AuNPs, and 5 kDA SH-mPEG-coated 30 nm AgNPs.

The following AgNPs were used to create the calibration curve are: 30 nm AgNPs, 35 nm AgNPs, 75 nm AgNPs, 95 nm AgNPs. As for the AuNPs used for the calibration curve are: 14, 30, 45, 60, 100 AuNPs.

After mass distribution measurement by SP-ICP-MS, the nanoparticle diameter distribution was approximated by assuming spherical geometry of nanoparticles and using Equation X:

$$D = \sqrt[3]{\frac{6*m}{\pi*\rho}} \qquad \text{Equation X}$$

Where:

D = diameter

m = mass

ρ = density

Gaussian normal distribution approximations of size estimates were generated using GraphPad Prism®.

9. Transmission electron microscopy (TEM) for analysis of nanoparticles

Transmission electron microscopy (TEM) imaging of synthesized nanoparticles was performed based on prior methods [144], [158], [162]. Nanoparticles were centrifuged to obtain concentrated pellets. After removing supernatant, 5 µL of the concentrated pellet was dropped onto a plasma-cleaned copper TEM grid with carbon film (Ted Pella, 01813-F) for 5 min, before wicking off excess solution. Grids were air

dried before images were collected using a JEOL-Zeiss 2010F TEM. Images were analyzed using ImageJ® to obtain diameter distribution estimates assuming spherical nanoparticles.

Results and Discussion

We first sought to compare the output of spectral flow cytometry, one of the flow cytometry types examined in Chapter 1, to confocal laser scanning microscopy (CLSM) and inductively coupled plasma mass spectrometry (ICP-MS).

Characterization of Nanoparticles

100 nm gold nanoparticles (AuNPs) coated with poly-ethylene glycol (PEG) were characterized using Transmission Electron Microscopy (TEM) (Figure 5A, B), Dynamic Light Scattering (DLS) (Figure 5C), Single Particle ICP-MS (SP-ICP-MS) (Figure 5D), and UV-VIS spectrophotometry (Figure 6). Both the TEM and SP-ICP-MS data showed that the core diameter of the 100 nm PEG-coated AuNPs are ~100 nm, and that this also matched that of the citrate-coated 100 nm AuNPs. That being said, an increase in hydrodynamic diameter due to PEGylation can be seen when examining Figure 5C.

The characterization of the 40 and 65 nm AuNPs as well as the 30 nm AgNPs can be found in Figures 5, 6, 7, 8 and 9. Again, TEM, DLS, SP-ICP-MS and UV-VIS spectrophotometry were used to characterize these nanoparticles. Additionally, zeta potential measurements were carried out to ensure that the surface coatings of the nanoparticles were successful (Table 2). A negative zeta potential was observed for HEP-coated 100 nm AuNPs, whereas the various PEGylated nanoparticles had a zeta potential close to neutral, due to the HEP being negatively charged in natures, while PEG is neutral, thus neutralizing the charge of the nanoparticles. The characterization of the HEP-coated 100 nm AuNPs can be seen in Figure 10.

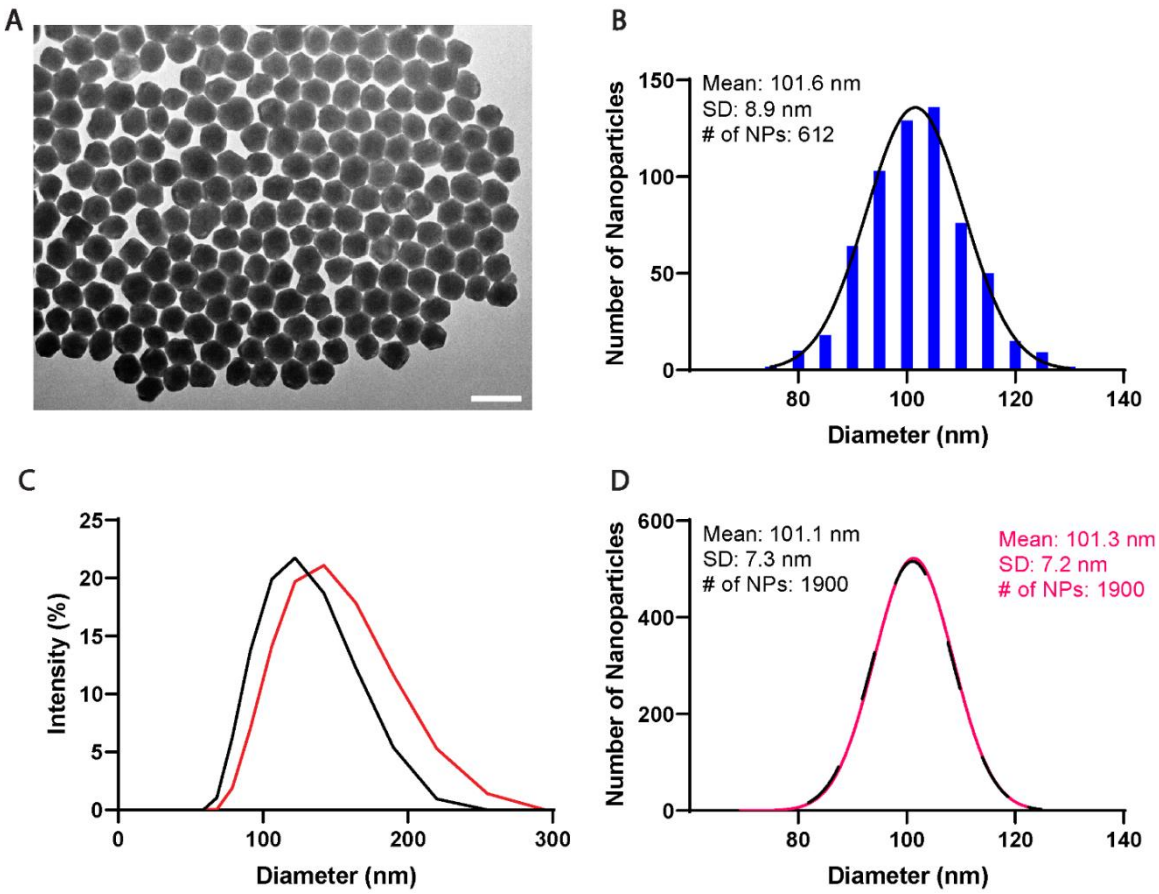

Figure 5: Characterization of PEG-coated 100 nm AuNPs. (A) Transmission electron microscopy (TEM) image of 100 nm AuNPs. The scale bar is 200 nm. **(B)** Size distribution analysis of multiple TEM images including **(A)**. Black line represents Gaussian fit. The total number of nanoparticles analyzed was 612 nanoparticles where NPs stand for nanoparticles. The mean and standard deviation for those nanoparticles are 101.6 nm ± 8.9 nm. **(C)** Dynamic light scattering (DLS) characterization of 100 nm AuNPs in citrate and Tween (black) compared to PEG-coated 100 nm AuNPs (pink). The average Polydispersity index (PdI) for the 100 nm AuNPs in Tween + citrate is 0.065, while it is 0.045 for PEGylated 100 nm AuNPs. **(D)** Single particle inductively-couple mass spectrometry (SP ICP-MS) size distribution analysis of PEG (red) and citrate-coated (black) 100 nm AuNPs. The total number of nanoparticles analyzed was 1900 nanoparticles where NPs stand for nanoparticles. The mean and standard deviation for the PEG-coated nanoparticles

are 101.3 nm ± 7.2 nm, while the citrate-coated NPs had a mean diameter of 101.1 nm and a standard deviation of 7.3 nm.

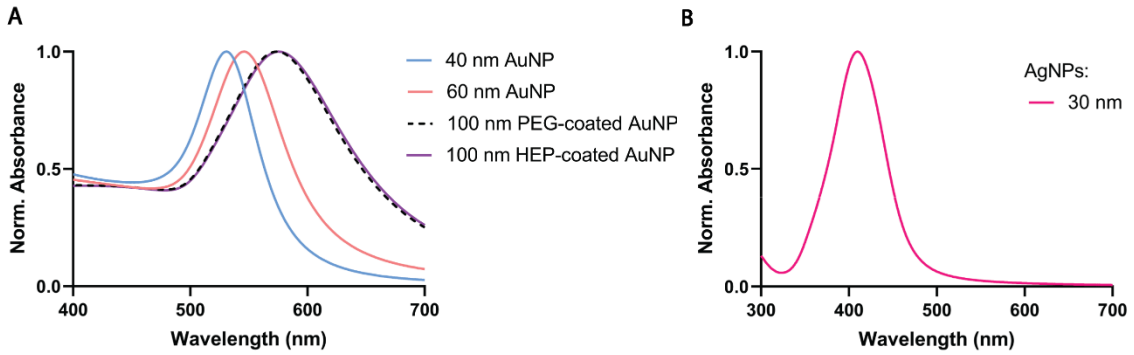

Figure 6: UV-VIS Spectrophotometry Nanoparticle Characterization. (A) Characterization of 40 nm, 65 nm, and 100 nm AuNPs. The wavelength measurements where ran through is 700 - 400 nm. **(B)** Characterization of 40 nm AgNPs. The wavelength measurements where ran through is 700 – 300 nm. The absorbance was normalized among the AuNPs and AgNPs.

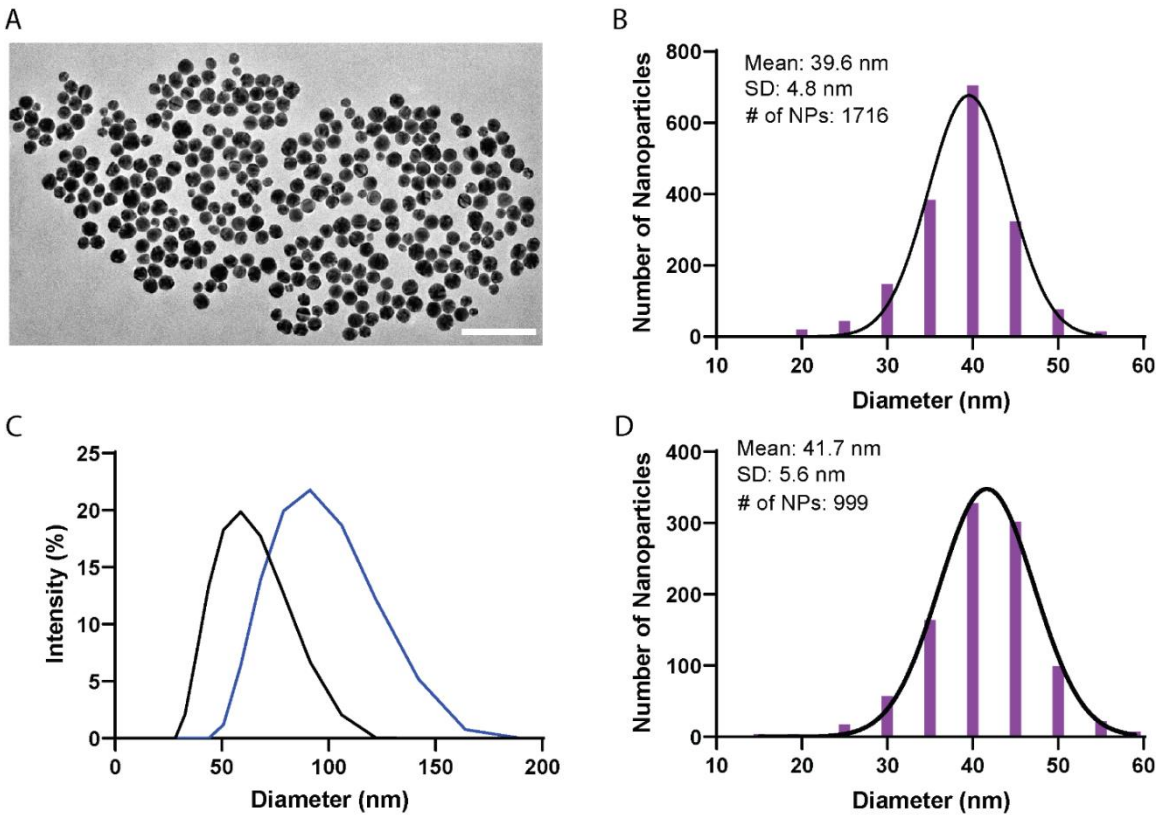

Figure 7: Characterization of 40 nm AuNPs. (A) Transmission electron microscopy (TEM) image of 40 nm AuNPs. The scale bar is 200 nm. **(B)** Size distribution analysis of multiple TEM images including **(A)**. Black line represents Gaussian fit. The total number of nanoparticles analyzed was 1716 nanoparticles where NPs stand for nanoparticles. The mean and standard deviation for those nanoparticles are 39.6 nm ± 4.8 nm. **(C)** Dynamic light scattering (DLS) characterization of 100 nm AuNPs in citrate and Tween (black) compared to PEG-coated 40 nm AuNPs (blue). The average Polydispersity index (PdI) for the 40 nm AuNPs in Tween + citrate is 0.067, while it is 0.032 for PEGylated 40 nm AuNPs. **(D)** Single particle inductively-couple mass spectrometry (SP ICP-MS) size distribution analysis of the 40 nm AuNPs. Black line represents Gaussian fit. The total number of nanoparticles analyzed was 999 nanoparticles where NPs stand for nanoparticles. The mean and standard deviation for those nanoparticles are 41.7 nm ± 5.6 nm.

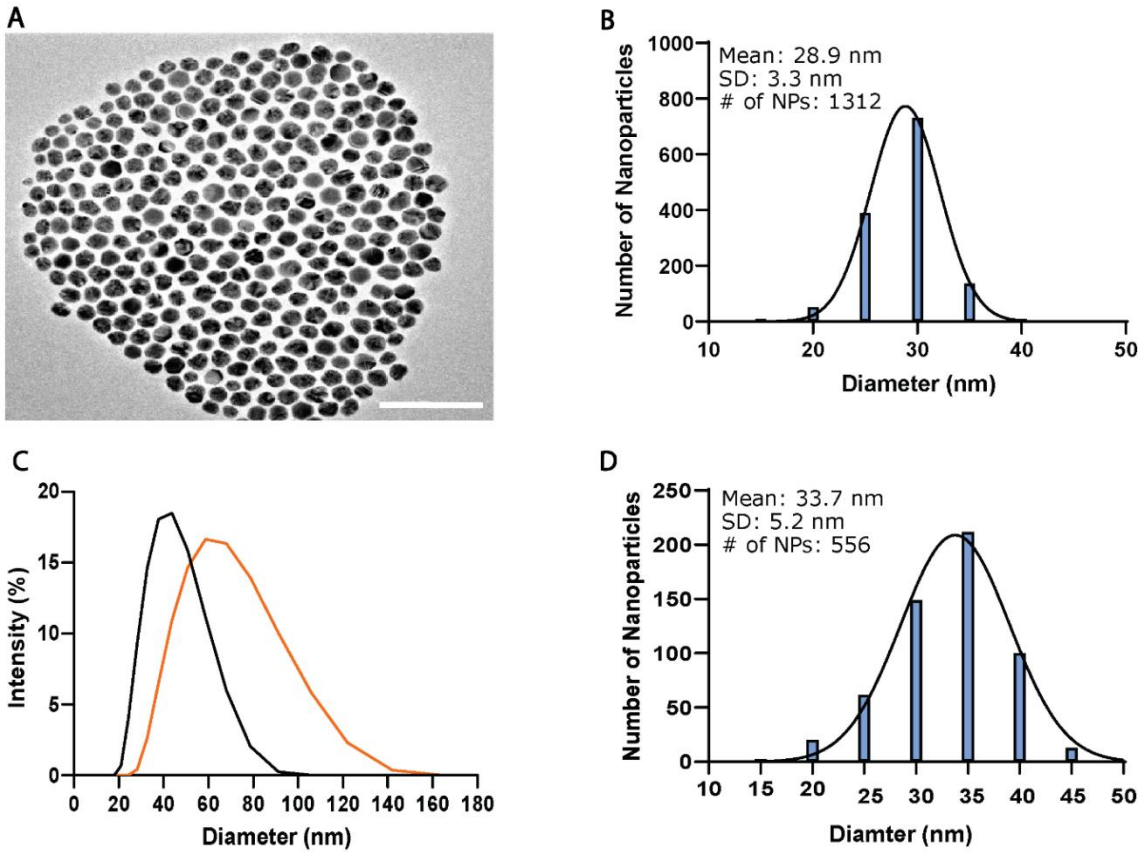

Figure 8: Characterization of 30 nm AgNPs. (A) Transmission electron microscopy (TEM) image of 30 nm AgNPs. The scale bar is 200 nm. **(B)** Size distribution analysis of multiple TEM images including **(A)**. Black line represents Gaussian fit. The total number of nanoparticles analyzed was 1312 nanoparticles where NPs stand for nanoparticles. The mean and standard deviation for those nanoparticles are 28.9 nm ± 3.3 nm. **(C)** Dynamic light scattering (DLS) characterization of 30 nm AgNPs in citrate and Tween (black) compared to PEG-coated 30 nm AgNPs (red). The average Polydispersity index (PdI) for the 30 nm AuNPs in Tween + citrate is 0.116, while it is 0.106 for PEGylated 40 nm AgNPs. **(D)** Single particle inductively-couple mass spectrometry (SP ICP-MS) size distribution analysis of the 40 nm AgNPs. Black line represents Gaussian fit. The total number of nanoparticles analyzed was 556 nanoparticles where NPs stand for nanoparticles. The mean and standard deviation for those nanoparticles are 33.7 nm ± 5.2 nm.

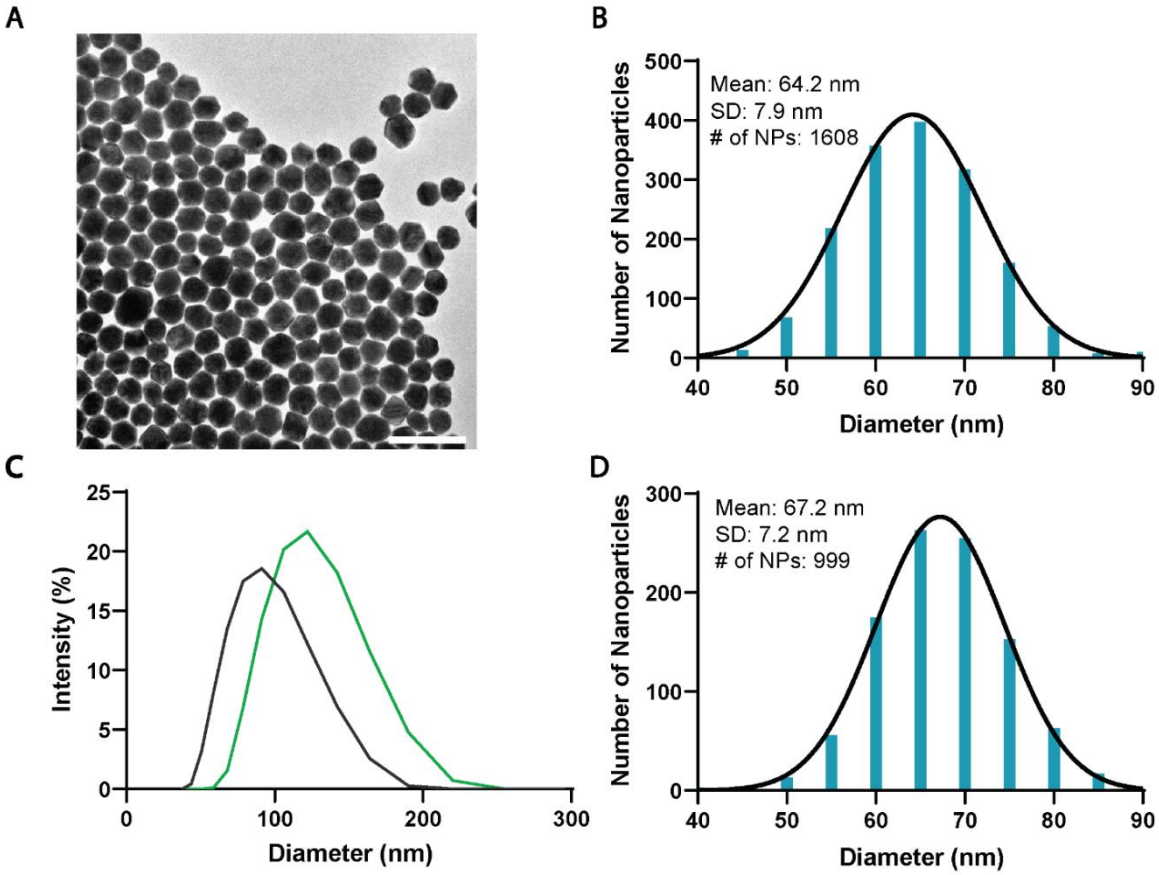

Figure 9: Characterization of 65 nm AuNPs. (A) Transmission electron microscopy (TEM) image of 65 nm AuNPs. The scale bar is 200 nm. **(B)** Size distribution analysis of multiple TEM images including **(A)**. Black line represents Gaussian fit. The total number of nanoparticles analyzed was 1608 nanoparticles where NPs stand for nanoparticles. The mean and standard deviation for those nanoparticles are 64.2 nm ± 7.9 nm. **(C)** Dynamic light scattering (DLS) characterization of 65 nm AuNPs in citrate and Tween (black) compared to PEG-coated 65 nm AuNPs (green). The average Polydispersity index (PdI) for the 65 nm AuNPs in Tween + citrate is 0.065, while it is 0.027 for PEGylated 65 nm AuNPs. **(D)** Single particle inductively-couple mass spectrometry (SP ICP-MS) size distribution analysis of the 65 nm AuNPs. Black line represents Gaussian fit. The total number of nanoparticles analyzed was 999 nanoparticles where NPs stand for nanoparticles. The mean and standard deviation for those nanoparticles are 67.2 nm ± 7.2 nm.

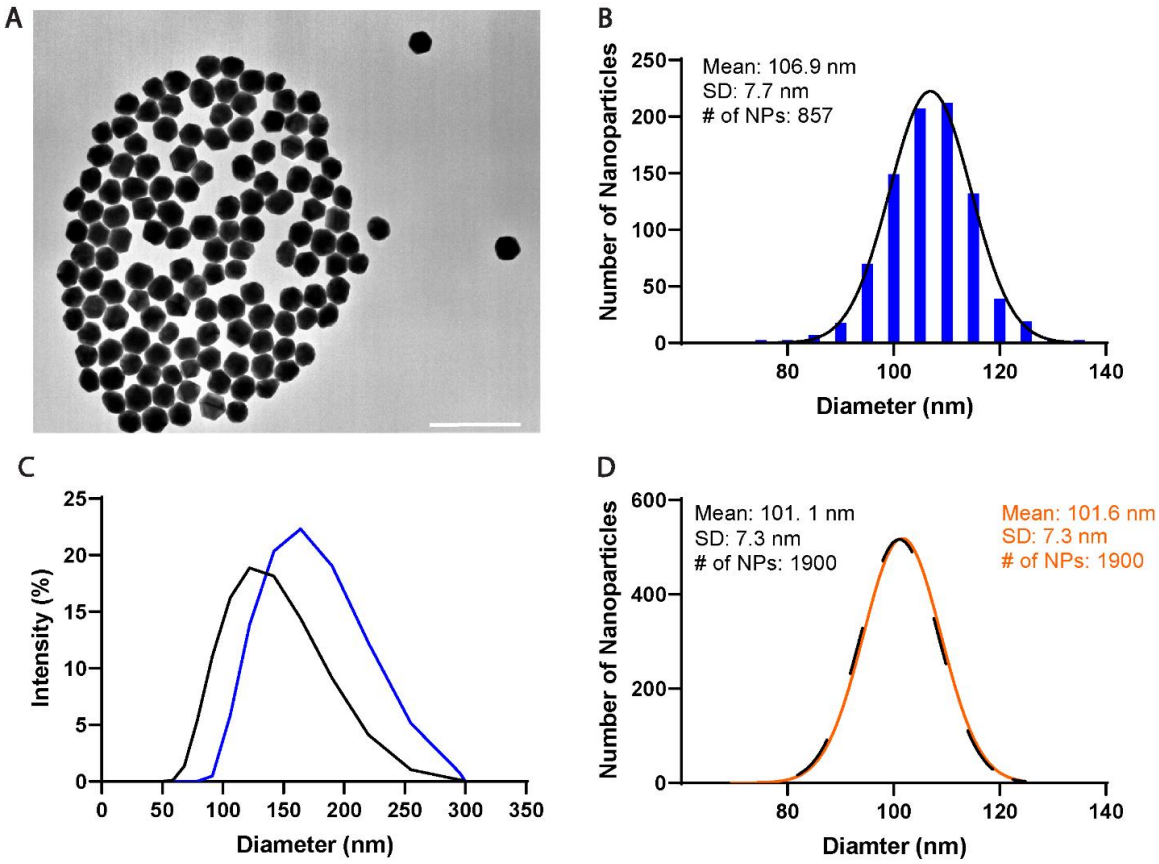

Figure 10: Characterization of 100 nm Heparosan-coated (HEP-coated) AuNPs. (A) Transmission electron microscopy (TEM) image of 100 nm Heparosan-coated AuNPs. The scale bar is 400 nm. **(B)** Size distribution analysis of multiple TEM images including **(A)**. Black line represents Gaussian fit. The total number of nanoparticles analyzed was 857 nanoparticles where NPs stand for nanoparticles. The mean and standard deviation for those nanoparticles are 106.9 nm ± 7.7 nm. **(C)** Dynamic light scattering (DLS) characterization of 65 nm AuNPs in citrate and Tween (black) compared to HEP-coated 100 nm AuNPs (blue). The average Polydispersity index (PdI) for the 100 nm AuNPs in Tween + citrate is 0.067, while it is 0.026 for HEPylated 100 nm AuNPs. **(D)** Single particle inductively-couple mass spectrometry (SP ICP-MS) size distribution analysis of HEP (orange) and citrate-coated (black) 100 nm AuNPs. The total number of nanoparticles analyzed was 1900 nanoparticles where NPs stand for nanoparticles. The mean and

standard deviation for the HEP-coated nanoparticles are 101.6 nm ± 7.3 nm, while the citrate-coated NPs had a mean diameter of 101.1 nm and a standard deviation of 7.3 nm.

Table 2: Nanoparticle Characterization via Zeta Potential

s: Mean +/- Standard Deviation

Nanoparticle Size (nm)	Material	Surface Modification	Zeta Potential (mV) s
100	Gold	Citrate, Tween 20	-26.8 +/- 0.9
100	Gold	10 kDa mPEG-OPSS	1.5 +/- 0.9
100	Gold	13.3 kDA HEP-OPSS	-18.9 +/- 0.7
65	Gold	10 kDa mPEG-OPSS	1.6 +/- 0.5
40	Gold	10 kDa mPEG-OPSS	-0.2 +/- 0.9
30	Silver	5 kDA mPEG-SH	-4.7 +/- 0.4

Establishing the Capability of Flow Cytometry to Detect Events from Cells that Have Uptaken Nanoparticles

We hypothesized that an increase in side scattering (SSC) signal in flow cytometry, will be supported by light scattering visualization in CLSM and an increase in AuNP/cell count in ICP-MS. To test this hypothesis, we did nanoparticle uptake of PEG-coated 100 nm AuNPs and used RAW 264.7 macrophages cell line. RAW 264.7 macrophages were used due to their phagocytic behavior [165], [166]. We ran the samples in flow cytometry and saw an increase in SSC signal (Figure 11C). This shows that the presence of nanoparticles in cells would change the cellular complexity by increasing it. This would help us understand the extent of the nano-bio interactions.

Moreover, since there was an increase in the SSC-A (%), these data sugest that there was a successful uptake of NPs by RAW 264.7 macrophages and this data was supported by the batch mode ICP-MS data in Figure 11B. A 10,000-fold increase in AuNP cell content can be seen from the data. Additionally, we used CLSM (Figure 11A) to confirm that the increase in the SSC signal from the flow data and the light scattering signal from the CLSM data were in fact due to the internalized nanoparticles. A great increase in light scattering signal was observed when imaging the RAW 264.7 macrophage sample with nanoparticles compared to that of the control.

To be able to analyze the flow cytometry data, a flow cytometric gating strategy was followed throughout the various experiments to determine the changes in SSC, and can be seen in Figure 12. All the flow cytometry data used to create the different bar graphs below were obtained from Quadrant 1. Additionally, all the conditions for the flow cytometry

experiments were performed using triplicates, and the data for each triplicate obtained from Quadrant 1 were averaged out and the average was used to create the bar graphs.

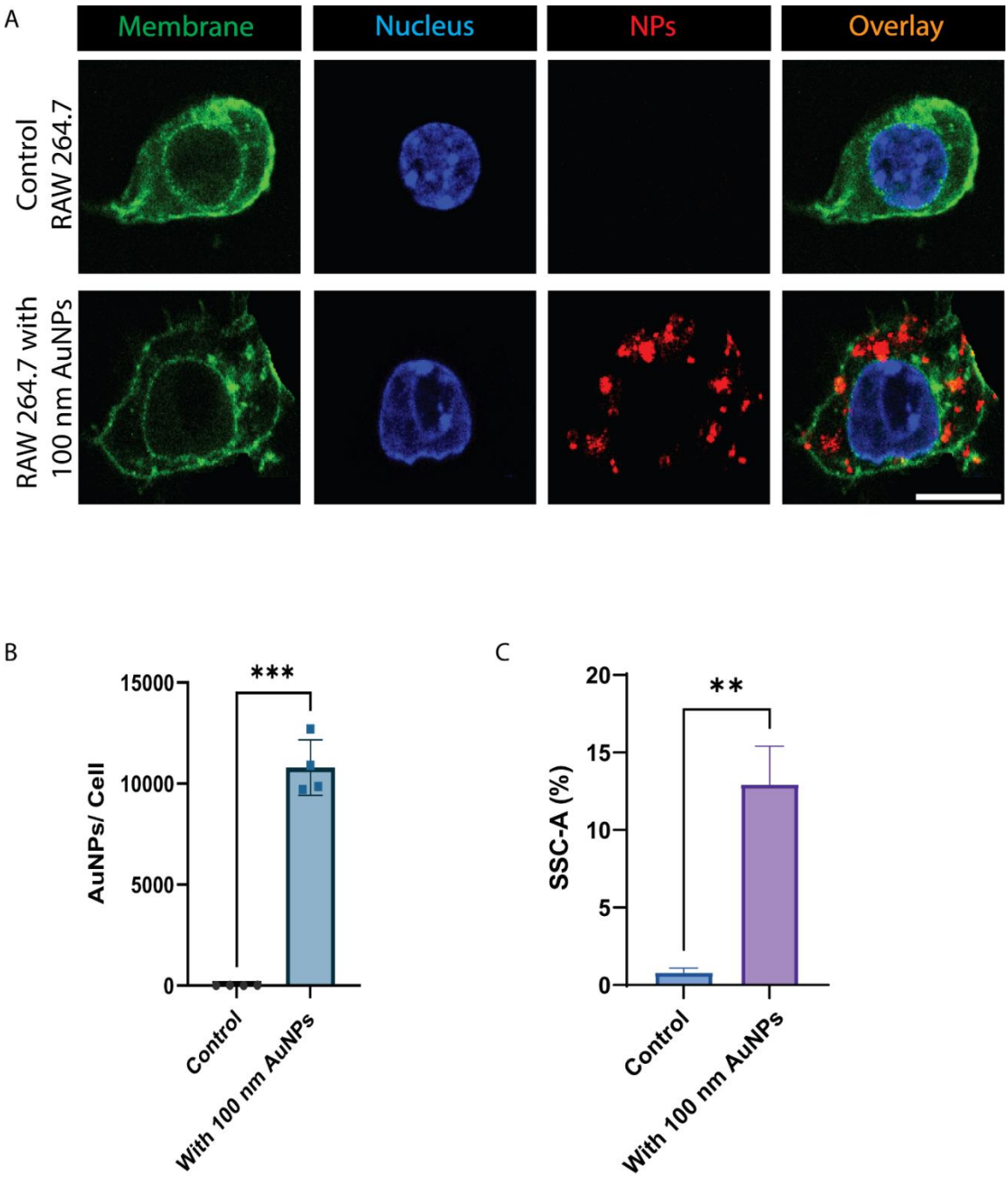

Figure 11: Nanoparticle Uptake of 100 nm AuNPs by RAW 264.7 Macrophage Cell Line. (A) Visualization of nanoparticle uptake through light scattering for RAW 264.7 with 100 nm AuNP

performed by confocal laser scanning laser microscopy (CLSM). The different channels for the membrane, nucleus, and light scattering along with the overlay channel are shown for both the control and the experimental sample. All samples were performed in a triplicate. The scale bar = 10 μm. **(B)** Batch inductively plasma mass spectrometry (ICP-MS) mode showing the uptake of 100 nm AuNPs by RAW 264.7. A Welch's t-test was performed and a statistical significance of <0.0001 was obtained. n = 4 samples for both the control and the experimental sample. **(C)** Flow cytometric analysis of the 100 nm AuNP uptake by RAW 264.7 macrophages. A p-value less than 0.005 was obtained from the unpaired t-test. n = 3 samples for both the control and the experimental sample.

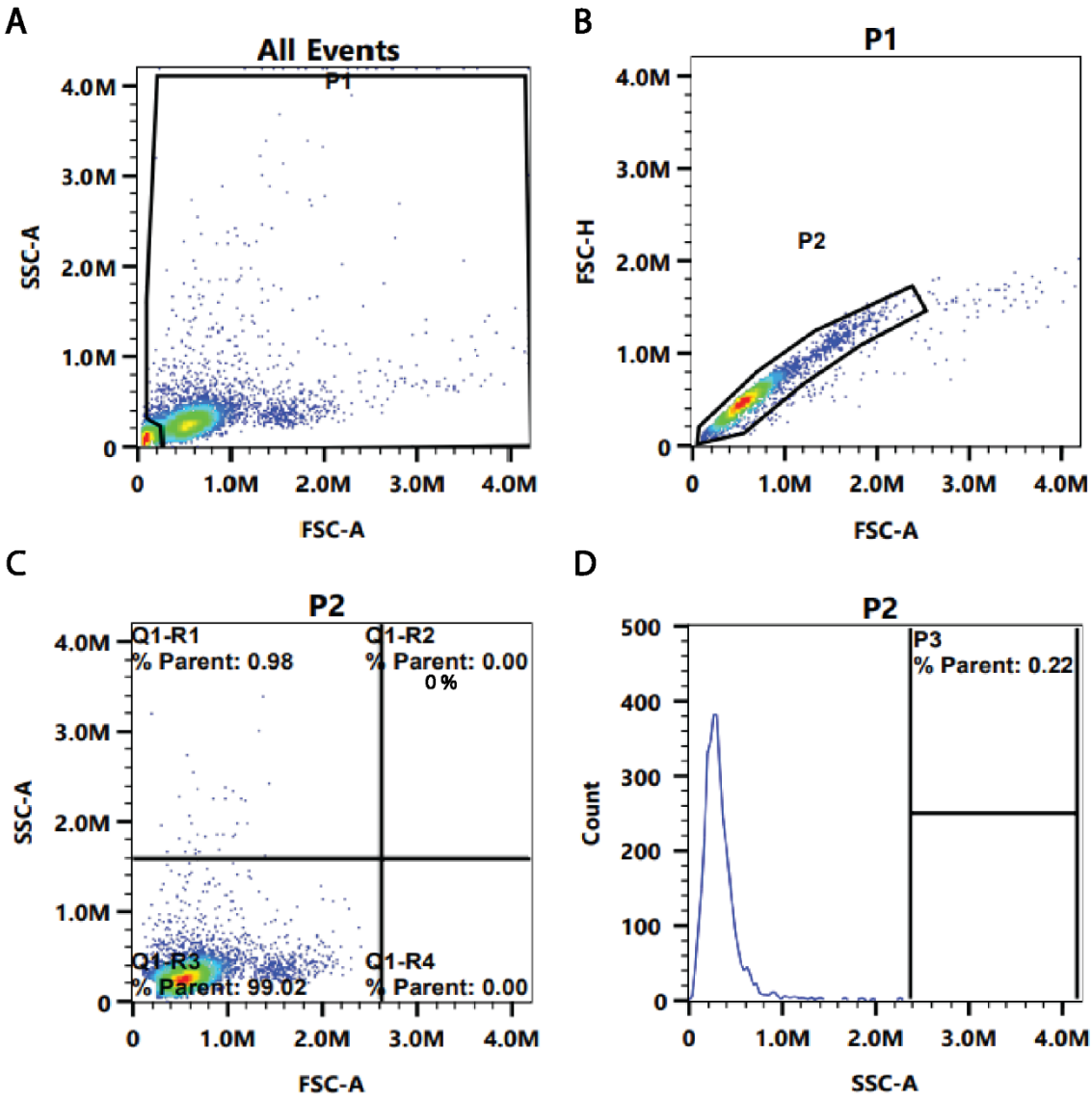

Figure 12: Flow cytometry gating strategy. (A) A FSC-A by SSC-A plot showing the raw data obtained from flow cytometry. P1 represents the desired gate surrounding the non-debris area. **(B)** FSC-A by FSC-H was done to obtain the singlets from the data. Then, a new gate, P2, was drawn around the region of interest of those singlets. **(C)** A FSC-A by SSC-A quadrant gating strategy was done over P2. The quadrant of interest is Q1 as that will change depending on the experimental conditions compared to the control. **(D)** Another post-analysis method of P2 to show how the SSC-A data are distributed. The P3 gating strategy will be used to determine whether or not there will

be a difference in the histogram's SSC-A based on the experimental conditions when compared to the control.

Examining the Generality of Flow Cytometry

Once we validated that the increase in SSC in fact is due to the uptake of nanoparticles using CLSM and ICP-MS, we then sought to confirm and show that flow cytometry is not only limited to the detection of SSC signal from RAW 264.7 macrophages and 100 nm AuNPs. To do this, we used different nanoparticle systems, which included varied nanoparticles sizes and nanoparticle types. We also changed the type of cell line used. The nanoparticles that we used were 40 nm AuNPs, 65 nm AuNPs and 30 nm silver nanoparticles (AgNPs). In addition to the RAW 264.7 macrophages, we ended up using 4T1 murine cells.

Changing Nanoparticle Size

We confirmed that flow cytometry is not limited to a specific cell type nanoparticle size or type as can be seen in Figures 13 and 14. Based on the CLSM data, one can see that as the size of the nanoparticle increases from 40 nm to 65 nm to 100 nm (Figures 11, 13A and 14), the intensity of the light scattering signal of the nanoparticles increases as well. This can also be shown in the higher SSC-A (%) obtained from when running the sample of cells and uptaken 100 nm gold nanoparticles compared to the cell sample with internalized 40 nm AuNPs. That being said, from the flow cytometry data we can see that the SSC-A (%) increase due to the presence of the 65 nm AuNPs is greater than that of the 100 nm AuNPs. This is likely due to the fact that ~60 nm AuNPs is the size at which the greatest number of nanoparticles per cell is seen, compared to other AuNP sizes. This was demonstrated in Chithrani *et al*'s paper [167].

Changing Nanomaterial Type

Originally, before characterization, 30 nm AgNPs were thought to be 40 nm in diameter, which is why the same concentration of nanoparticles for both 40 nm AuNPs and 30 nm AgNPs was used for the uptake. However, after doing TEM and SP-ICP-MS characterization, it was found that the AgNPs used were 30 nm in diameter rather than being 40 nm AgNPs. This explains why there was less light scattering from the 30 nm AgNPs when compared to those of the 40 nm AuNPs. Syed *et al* have shown that when examining two nanoparticle systems or types of the same size, the nanoparticle with the greatest refractive mismatch index will have a greater light scattering intensity [168]. This is why we hypothesized that the 30 nm AgNPs will show a greater light scattering signal. However, from the CLSM data, we can see that the 40 nm AuNPs had higher light scattering signal, which could be explained by the size of the silver nanoparticles being smaller than anticipated.

As for the flow cytometry data, we were able to see that the change in granularity due to the nano-bio interactions and presence of the 30 nm AgNPs was determined by the flow cytometry, meaning that using this instrument we can determine the different nano-bio interactions that occur due to the change in the nanomaterial type.

Since 30 nm AgNPs seem to cause greater increase in the SSC-A (%) than the 40 nm AuNPs, and since the same concentration was used, this could be likely be wither due to the fact that AgNPs' physical properties allow then to scatter more light than gold [168], or that there was a higher uptake of AgNPs than AuNPs. ICP-MS can be used to verify if there was a difference in the uptake between the AgNPs and AuNPs. This could be something to do as a next step.

Another explanation could be explained using the detection limit of the flow cytometry. Zucker *et al* showed that the detection limit for AgNPs is 40 nm, whereas it is 60 nm for AuNPs [169], [170]. However, the detection of AuNPs as small as 24 nm is possible using a laboratory-built high-sensitivity flow cytometer [171]. Since the detection limit varies from one flow cytometer to another, one can therefore understand that it is even possible for smaller sizes of silver nanoparticles to be detected if the sensitivity of the flow cytometer is increased.

Changing Cell Line

4T1 cells were used as they are epithelial cells and hence, they are a different cell type than RAW 264.7 cells which are macrophages and are known for their endocytic capabilities. This helps us understand how cells from different origins interact with nanoparticles and how that affects the nano-bio interactions.

From the CLSM Figure 13 we were able to see that there is a light scattering signal coming from the PEG-coated 100 nm AuNPs, which were internalized in the cells. The intensity of the light scattering signal is different from that of the one seen in Figure 11 that shows the data from RAW 264.7 that have uptaken PEG-coated 100 nm AuNPs.

As for the flow cytometry data, we can see that the flow cytometry was able to detect the SSC-A (%) from both the cell only condition as well as the cells + NP condition. This indicates that flow cytometry can detect changes in the complexity of different cell lines.

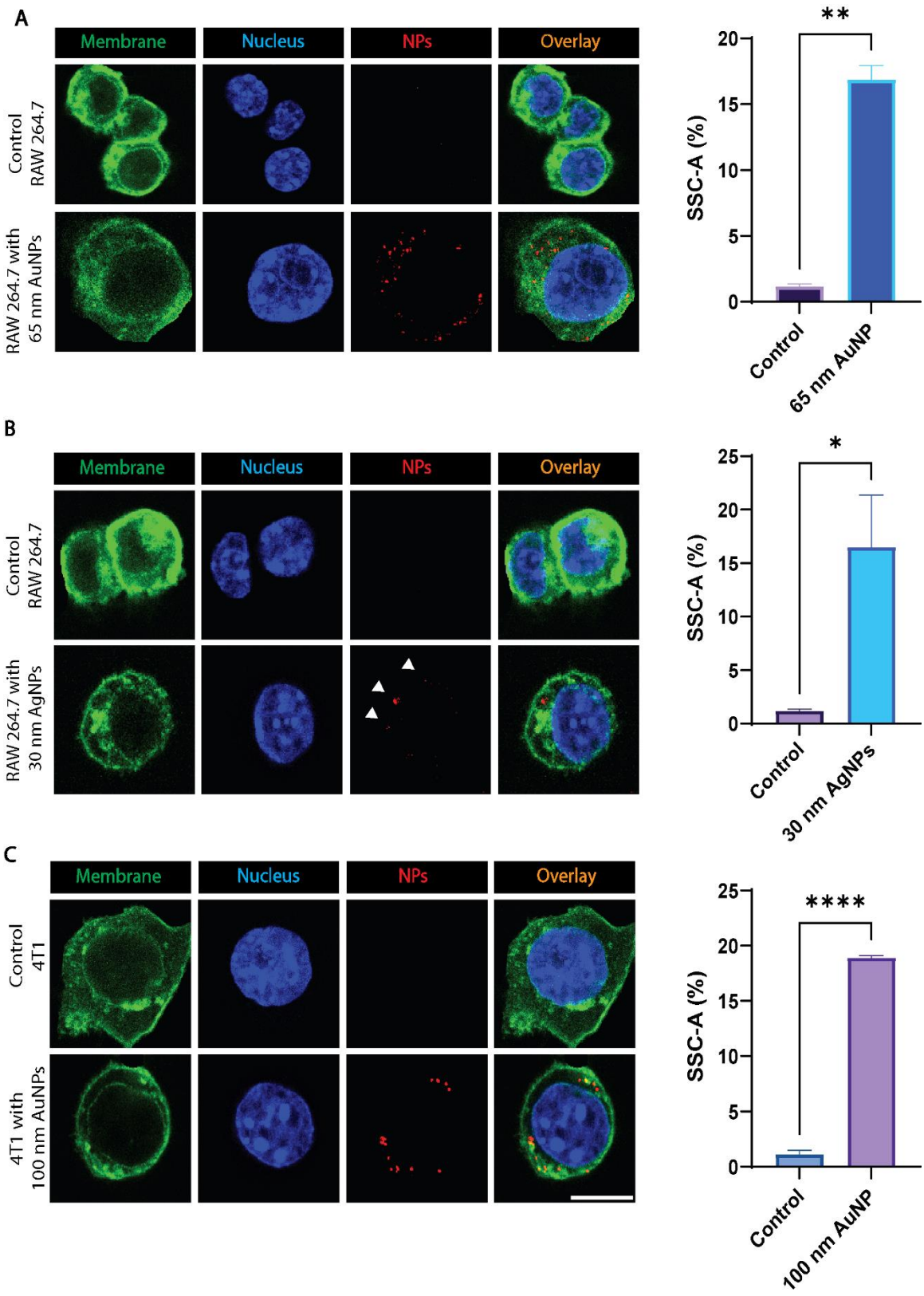
A
Membrane
Nucleus
NPs
Overlay
Control RAW 264.7
RAW 264.7 with 65 nm AuNPs
**
SSC-A (%)
20
15
10
5
0
Control
65 nm AuNP
B
Membrane
Nucleus
NPs
Overlay
Control RAW 264.7
RAW 264.7 with 30 nm AgNPs
*
SSC-A (%)
25
20
15
10
5
0
Control
30 nm AgNPs
C
Membrane
Nucleus
NPs
Overlay
Control 4T1
4T1 with 100 nm AuNPs
****
SSC-A (%)
25
20
15
10
5
0
Control
100 nm AuNP

Figure 13: Detection of nanoparticles by flow cytometry is not limited to 100 nm AuNPs. (A) (Left) Visualization of nanoparticle uptake through light scattering for RAW 264.7 with 65 nm AuNP performed by confocal laser scanning laser microscopy (CLSM). The different channels for the membrane, nucleus, and light scattering along with the overlay channel are shown for both the control and the experimental sample. All samples were performed in a triplicate. (Right) Flow cytometric analysis of the 65 nm AuNP uptake by RAW 264.7 macrophages. A p-value <0.005 was obtained from the Welch's t-test. n = 3 samples for both the control and the experimental samples. **(B)** (Left) Visualization of nanoparticle uptake through light scattering for RAW 264.7 with 40 nm AgNPs performed by confocal laser scanning laser microscopy (CLSM). The different channels for the membrane, nucleus, and light scattering along with the overlay channel are shown for both the control and the experimental sample. All samples were performed in a triplicate. (Right) Flow cytometric analysis of the 40 nm AgNPs uptake by RAW 264.7 macrophages. A p-value <0.05 was obtained from the Welch's t-test. n = 3 samples for both the control and the experimental samples. **(C)** (Left) Visualization of nanoparticle uptake through light scattering for 4T1 triple negative mouse cells with 100 nm AuNP performed by confocal laser scanning laser microscopy (CLSM). The different channels for the membrane, nucleus, and light scattering along with the overlay channel are shown for both the control and the experimental sample. All samples were performed in a triplicate. (Right) Flow cytometric analysis of the 10 nm AuNP uptake by 4T1 cells. A p-value <0.0001 was obtained for the 100 nm AuNPs from the Welch's t-test. n = 3 samples for both the control and the experimental samples. The scale bar = 10 μm.

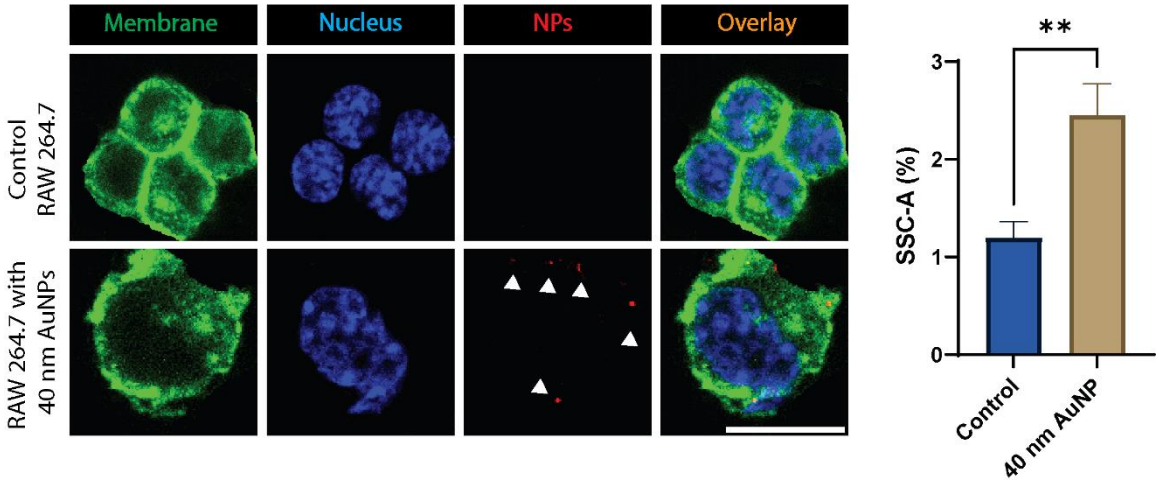

Figure 14: Detection of nanoparticles by flow cytometry for 40 nm AuNPs. (Left) Visualization of nanoparticle uptake through light scattering for RAW 264.7 with 40 nm AuNP performed by confocal laser scanning laser microscopy (CLSM). The different channels for the membrane, nucleus, and light scattering along with the overlay channel are shown for both the control and the experimental sample. All samples were performed in a triplicate. The scale bar = 10 μm. (Right) Flow cytometric analysis of the 40 nm AuNP uptake by RAW 264.7 macrophages. ns means not significant. A p-value <0.01 was obtained from the Welch's t-test. n = 3 samples for both the control and the experimental samples.

Understanding the Kinetics Behavior of Cells using Flow Cytometry

After demonstrating the ability of flow cytometry to run samples prepared using different cell lines, nanoparticle size and type, we wanted to use the flow cytometer to understand the uptake behavior of the cells to these nanoparticles over a set period of time. A few papers have used flow cytometry as a technique to demonstrate the behavior of cell uptake and kinetics [31], [47]. Therefore, to understand the flow cytometry capabilities and see if a similar trend can be obtained to what was shown in flow cytometry kinetics analysis papers, we did our own kinetics analysis experiment using various time points starting from t=0 hr to t=24 hrs.

We performed a kinetics analysis experiment using 5 different concentrations of PEG-coated 100 nm AuNPs that were uptaken for 0, 1, 2, 4, 6, 8 and 24 hrs. The five concentrations were: 0.1 nM, 0.04 nM, 0.02 nM, 0.0133 nM, and 0.01 nM. Those different time points and concentrations would allow us to see how the kinetics of the cell changes with time, and how AuNP concentration affects the kinetics behavior of the cells. After collecting and analyzing the data, we found out that as the concentration of nanoparticles increases, the line changes from a straight line to a plateau (Figure 15C). This can indicate that at certain concentrations, the flow cytometer can get saturated by the amount of NPs in a cell, causing the SSC trend to form a plateau. Since the 0.02 nM is the last concentration at which a straight line is formed, it was the concentration chosen to perform the kinetics analysis experiments using CLSM, ICP-MS, and ultimately, which is yet to be studied, flow cytometry.

In addition to the trends in data obtained from the five concentrations as well as the R^2 value for each trend line which allows us to determine the extent of effect of the existence

of any outlier (Figure 15C), we examined the time constant value for each concentration. The time constants for the five concentrations of 0.1 nM, 0.04 nM, 0.02 nM, 0.0133 nM, and 0.01 nM, are 9.25, 19.89, 7885, 34685, and 48294, respectively. This is an indication of the uptake time for the nanoparticles by the cells. It was seen that the higher the concentration of the AuNPs, the lower the time constant was. This is likely due to the presence of more AuNPs per volume used for the incubation and uptake of NPs by cells. The greater the number of AuNPs per volume present in the media, the greater the number of AuNPs in cells is as the chance of the NP uptake by cell increases.

Figure 15A shows the confocal data for the kinetics analysis experiment. When looking at the panel, one can see that the intensity of the light scattering increases as the incubation time with the nanoparticles increases as well. At t =24 hrs, we can see the highest light scattering signal and therefore, the highest uptake compared to the other time points. Although when looking at the batch mode ICP-MS data (Figure 15B) we see that the highest number of AuNP/cell is at t = 24 hrs, the increase between 4 and 8 hrs, and 8 and 24 hrs is not significant.

In order to understand the difference in the CLSM and ICP-MS data, although the general trend seems similar, we can do a quantitative analysis of the CLSM data. That way we can determine the amount of the light scattering signal between the different time points, which will allow us to compare the data to that of the ICP-MS. This is something to be examined.

Another way to verify that the trend in data collected from both the ICP-MS and CLSM can also be seen in flow cytometry, a kinetics analysis experiment is yet to be performed using FCM using the concentration of 0.02 nM while varying the uptake period to cover a

24-hr time span. The time points will be 0, 4, 8 and 24 hrs, so that they match those time points used in the CLSM and ICP-MS kinetics analysis experiments. However, this is yet to be investigated.

One other thing to mention is that in Figure 15B, we see a lower AuNP/cell count in comparison to that in Figure 11B. This could be explained by the change in passage number used to perform those two experiments as well as having to use a new batch of PEG-coated 100 nm AuNPs for all the kinetics analysis experiments from the one used for the first uptake experiment.

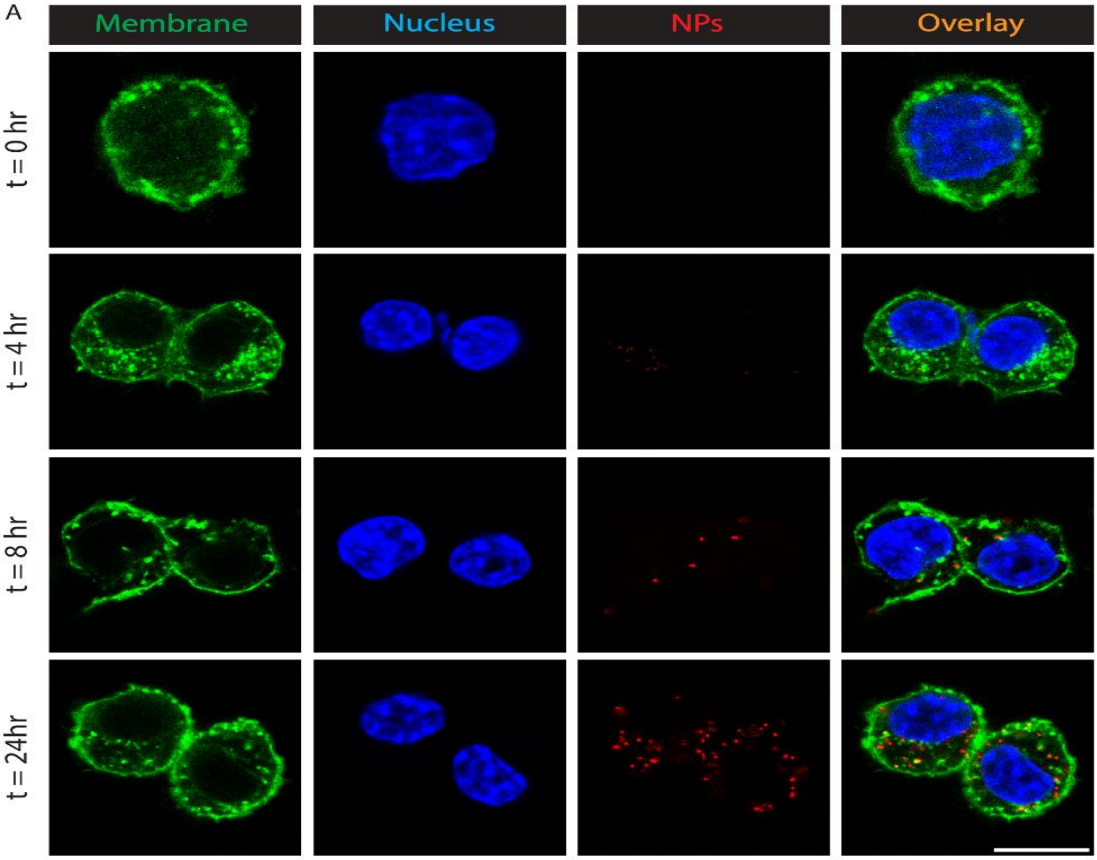
A
Membrane
Nucleus
NPs
Overlay
t = 0 hr
t = 4 hr
t = 8 hr
t = 24hr

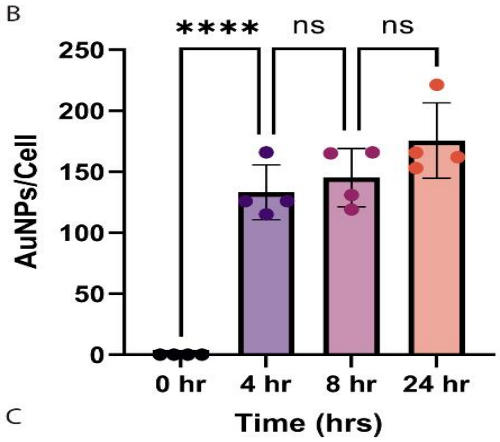
B
****
ns
ns
AuNPs/Cell
250
200
150
100
50
0
0 hr
4 hr
8 hr
24 hr
Time (hrs)

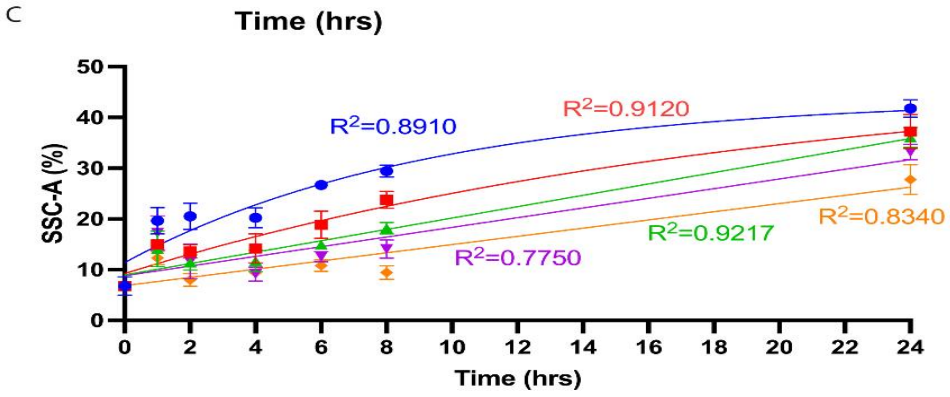
C
SSC-A (%)
50
40
30
20
10
0
R²=0.8910
R²=0.9120
R²=0.9217
R²=0.8340
R²=0.7750
0
2
4
6
8
10
12
14
16
18
20
22
24
Time (hrs)

Figure 15: Kinetics Analysis of 100 nm AuNPs Uptake by RAW 264.7 Macrophage Cell Line. **(A)** Visualization of nanoparticle uptake through light scattering for RAW 264.7 with 100 nm AuNP using Keyence. The different channels for the membrane, nucleus, and light scattering along with the overlay channel are shown for both the control and the experimental sample. All samples were performed in a triplicate. The scale bar = 10 μm. **(B)** Batch inductively plasma mass spectrometry (ICP-MS) mode showing the uptake kinetics of 100 nm AuNPs by RAW 264.7. A one-way ANOVA with Tukey's multiple comparisons was performed. ns = not significant, while **** is equivalent to $p<0.0001$. $a= 0.05$. $n = 4$ samples for both the control and the experimental samples. **(C)** Flow cytometry data for uptake kinetics of 5 different concentrations. A nonlinear fit trend was used to determine the R^2 value for the five different trend lines. The five concentrations are 0.1 nM (blue), 0.04 nM (red), 0.02 nM (green), 0.0133 nM (purple), and 0.01 nM (orange).

Understanding the Uptake Pathway of Nanoparticles and the Effect of Surface Modification on Nanoparticle Uptake using Flow Cytometry

Now that we understood the kinetics of the nanoparticle uptake, and we saw how different nanoparticle systems, and sizes and even cell types can be used and run through the flow cytometry, it is necessary to understand the effect of the surface coating on the uptake of the nanoparticles and hence, on the SSC signal obtained from flow cytometry. For this purpose, we used two different surface modifications which are Poly-Ethylene Glycol (PEG) and Heparosan (HEP). Additionally, we used four different types of physical inhibitors (Table 3) to understand which endocytosis pathway do the HEP-coated 100 nm AuNPs get uptaken by to enter the cells. By adding an inhibitor to the cells, we block a pathway or mechanism through which the nanoparticles pass through to get into the cells. The inhibitor that causes the greatest decrease in nanoparticle uptake indicates that the endocytosis pathway that this inhibitor blocked, is the (main) one through which nanoparticles enter the cells. Furthermore, we used temperature inhibition (4°C) to investigate the effect of low temperature on nanoparticle uptake. Low temperature causes the energy-dependent uptake and passive diffusion to get blocked due to the rigidity of the cell membrane [172].

Those inhibitors were used as they work using different mechanisms of action. However, many of the available inhibitors work on blocking more than one uptake pathway. This tends to be quite challenging to determine if any changes in the nanoparticle uptake were, in fact, due to one uptake pathway. For instance, Methyl-β-cyclodextrin ($M\beta CD$) inhibits both caveolae-mediated endocytosis as well as clathrin-mediated endocytosis [173]. $M\beta CD$ removes cholesterol from the plasma membrane [173],

therefore, affecting the function and structure of invaginated caveolae, including those of caveolae-dependent endocytosis [174]. Moreover, the cholesterol present in the cell membrane originates from lipoproteins that are internalized via clathrin-coated pits by receptor-mediated endocytosis [174]. Therefore, the removal of cholesterol from the cell membrane would affect both clathrin-mediated and caveolae-mediated endocytosis.

Hence, if the $M\beta CD$ inhibitor was used, it would be difficult to determine if the decrease in nanoparticle uptake was due to the inhibitions of either caveolae-mediated or clathrin-mediated, especially if the decrease in nanoparticle uptake was different compared to that of Filipin or Chlorpromazine. Therefore, it is important to choose the inhibitors for the endocytosis inhibition experiment with utmost carefulness.

Based on Yang *et al*, the endocytosis pathway through with HEP-coated AuNPs enter the cell is clathrin-mediated endocytosis [159]. To confirm that the HEP-coated AuNPs are uptaken by the calthrin-mediated endocytosis pathway, we performed our own endocytosis inhibition experiment using flow cytometry.

Table 3: Summary of Endocytosis Physical Inhibition Conditions Used in This Study

Inhibitor	Mechanism of action	Function/Pathway	Condition/Concentration	Ref.
Filipin (B)	Removes cholesterol from the plasma membrane	Caveolae-mediated and clathrin independent endocytosis	5 μg/mL	[175]
Chlorpromazine (CPZ) (D)	Unknown (AP2 inhibition)	Clathrin-mediated endocytosis	10 μg/mL	[175], [176]
Cytochalasin D (CD) (H)	Depolymerizes F-actin	Macropinocytosis and phagocytosis	1 μg/mL	[177], [178]
Sodium Azide	decreases ATP by inhibiting glycolysis	nonspecific endocytosis	0.1% w/v	[179]

First, to be able to understand the effect of the changing the surface modification on the uptake of AuNPs, we used HEP and PEG-coated 100 nm AuNPs. Since the effect of nanoparticle uptake can be seen through changes in the side scattering signal, we performed an uptake experiment using the flow cytometer for both the HEP and PEG-coated 100 nm AuNPs. We saw a significant increase in SSC-A (%) for the cells + HEP condition compared to the cells only condition. As for the cell + PEG condition, the presence of PEG-coated 100 nm AuNPs caused an increase in the SSC-A (%), however that increase is not significant (Figure 16A). This is why we decided to only use HEP-coated 100 nm AuNPs for the endocytosis inhibition experiment, in order to ensure that any signal we obtain is above the background or cell only condition level.

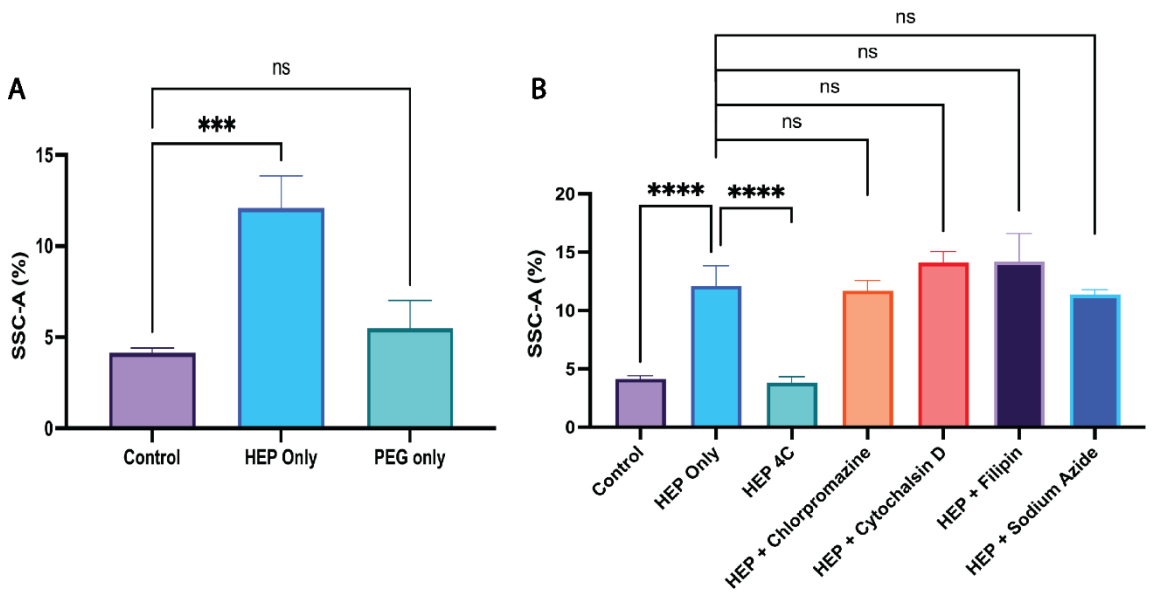

Figure 16: Endocytosis Inhibition of 100 nm AuNPs Uptake by RAW 264.7 Macrophage Cell Line. (A) Comparison of the SSC-A (%) for cells only, cells + HEP, and cells + PEG. A one-way ANOVA with Dunnett's multiple comparisons was performed. ns = not significant, while *** is equivalent to p=0.0006. a= 0.05. n = 3 samples for both the control and the experimental samples. **(B)** Uptake inhibition of HEG-coated 100 nm AuNPs. Five different kinds of inhibitors were used and the corresponding SSC-A (%) was measured and compared to the cell only and cell + HEG controls. A one-way ANOVA with Dunnett's multiple comparisons was performed. ns = not significant, while **** is equivalent to p<0.0001. a= 0.05.

As explained earlier, we used the inhibitors listed in Table 3 for physical inhibition, and had some samples stored at 4°C for temperature inhibition. Figure 16B shows the effect of the 5 types of inhibitors on the uptake of HEP-coated 100 nm AuNPs by RAW 264.7 cells. The data reflected in Figure 16 is obtained from the live cells, that were gated for after applying a viability assay. Figure 18 shows the live cell ratio for the different conditions used in this experiment.

As seen in Figure 16B, the temperature inhibition is the only condition that showed a significant difference in the SSC-A (%) when compared to the cell + HEP only condition, indicating a lower uptake of nanoparticles compared to that control (cell + HEP condition). Considering the data obtained from the physical inhibitors, any change that occurred in the side scattering signal was not significant. Specifically, we saw that the samples that were inhibited by Cytochalasin D and Filipin show an increased SSC-A (%) rather than a lower signal, which does not follow our hypothesis or Yang *et al*'s paper [158].

Due to such data obtained from the Cytochalasin D and Filipin conditions, we wanted to determine if these two inhibitors are effective or not, and if they were effective, whether the concentration used was not sufficient. In order to investigate that, we decided to run another endocytosis inhibition experiment, using three different concentrations of Cytochalasin D and Filipin on cells that have uptaken HEP-coated 100 nm AuNPs. However, this investigation is currently in progress, and the data has not been obtained yet.

Additionally, when looking at the CLSM data, we can see that the light scattering signals for HEP-coated 100 nm AuNPs samples that have been inhibited by Filipin seem to be higher than the rest of the other conditions, and similar to the intensity of the control (Figure 17). Since it is hard to determine the extent of the difference in the light scattering

signals, quantitative analysis for the light scattering signals obtained would allow us to investigate this further. It would allow us to see the extent of the effect of inhibitors on the uptake of the nanoparticles. Since this was not done, it would need to be done in the future as an improvement to this experiment.

With this collected data, we cannot say for sure if the uptake pathway for the HEP-coated 100 nm AuNPs is calthrin-mediated endocytosis, due to the change in the SSC-A (%) being insignificant. Although Yang *et al*'s data show that the uptake pathway for HEP-coated AuNPs, specifically 55 nm, is clathrin-mediated endocytosis [158], we were not able to confirm that for our HEP-coated 100 nm AuNPs using this experiment.

One possibility for such differences could be due to the difference in the size of the nanoparticles used. Based on Kumar *et al*, nanoparticles with diameter ≤200 nm preferred the clathrin-mediated endocytosis as an uptake pathway [180]. However, Li *et al* found that 80 nm AuNPs, with three different surface modifications (PEG, bPEI and lipoic-AuNPs), were significantly inhibited by clathrin inhibitors, while the degree of inhibition of the 40 nm varied with the change in the surface modification [181]. This indicates that nanoparticles of different sizes can get uptaken by cells using different endocytosis pathways, and that the surface modification does have an impact on the uptake pathway. Since 55 nm AuNPs are smaller than 100 nm AuNPs, this could explain the difference shown in the data.

Another reason why Yang's data were different is that for ICP-MS, samples are handled less than for the flow cytometry. Since after the 1.5 hrs, we needed to add a viability assay, do a couple of rounds of washes, scrape the cells, centrifuge, and fix them, we are bound to lose some cells and even kill some cells in the scraping process. As for the

ICP-MS, we only need to wash the samples a couple of times, then freeze them, meaning that the integrity of the samples in ICP-MS is better than that of the flow cytometry. Lastly, the samples get digested in ICP-MS which allows all the cells to be included in the data collection process, whereas when the cells are scraped, some remain adhered to the well-plate. In other words, since some samples are lost when preparing for flow cytometry experiments, this impacts the statistical comparison and data obtained.

Considering the aforementioned reasons behind the differences between Yang's data and mine, repeating this experiment would be necessary to see if any changes to the general trend in data would occur, which could allow us to have a better understanding of the uptake pathway for HEP-coated 100 nm AuNPs.

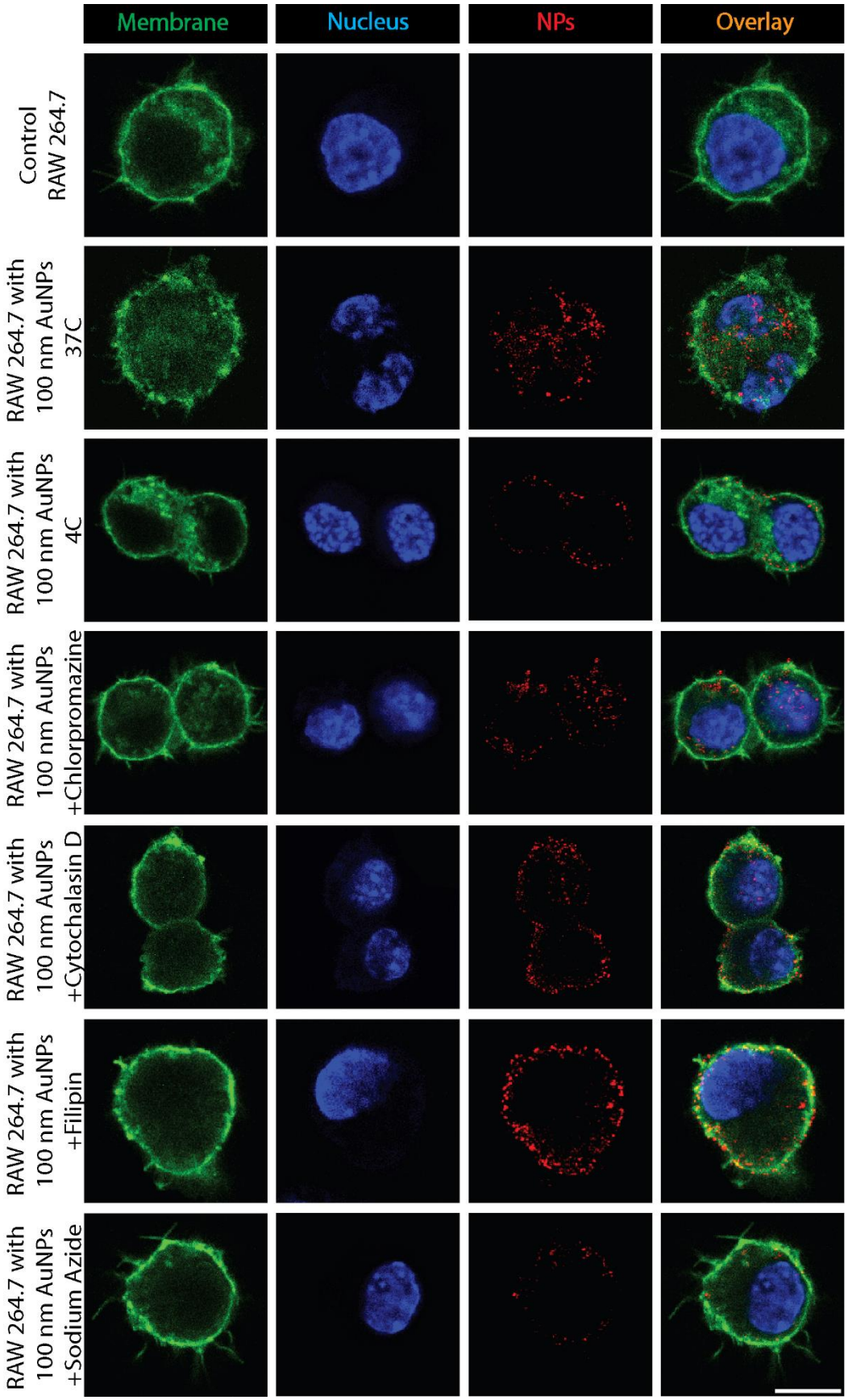
Membrane
Nucleus
NPs
Overlay
Control RAW 264.7
RAW 264.7 with 100 nm AuNPs 37C
RAW 264.7 with 100 nm AuNPs 4C
RAW 264.7 with 100 nm AuNPs +Chlorpromazine
RAW 264.7 with 100 nm AuNPs +Cytochalasin D
RAW 264.7 with 100 nm AuNPs +Filipin
RAW 264.7 with 100 nm AuNPs +Sodium Azide

Figure 17: Endocytosis Inhibition of HEP-coated 100 nm AuNPs Uptake by RAW 264.7 Macrophage Cell Line. Visualization of nanoparticle uptake through light scattering for RAW 264.7 with 100 nm AuNP performed by confocal laser scanning laser microscopy (CLSM). The different channels for the membrane, nucleus, and light scattering along with the overlay channel are shown for both the control and the experimental sample. Four different types of inhibitors were used, and the amount of light scattering signal was studied to determine the effect of inhibitors nanoparticle uptake by cells. All samples were performed in a duplicate. The scale bar = 10 μm.

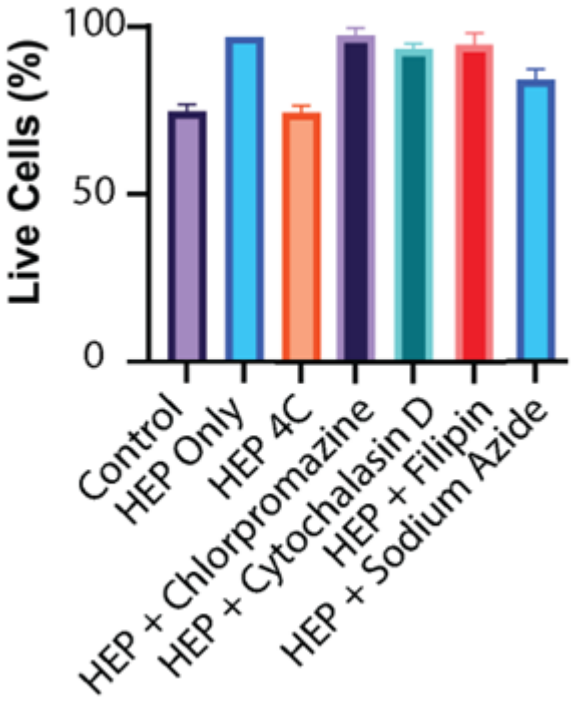

Figure 18: Live cell ratio for the different conditions in the endocytosis inhibition experiment after applying the viability assay and gating for live cells.

Investigating the Recovery of Cells from Inhibitors

Now that we were able to see the effect of having different surface modifications on nanoparticle uptake, we wanted to understand the effect of the inhibitors on the cells, by studying how fast cells can recover from the inhibitors as well as the cells' recovery effect on the uptake of the HEP-coated 100 nm AuNPs.

In order to do that, cells were incubated first for an hour with the corresponding inhibitors and were then incubated with nanoparticles only for 1.5 hrs, rather than inhibitors + nanoparticles (HEP-coated 100 nm AuNPs). Figure 19 demonstrates the data obtained from confocal laser scanning microscopy. It can be seen that the light scattering signal obtained from the samples that were incubated with the inhibitors is similar to that of the cells + HEP control. The light scattering signals for the four physical inhibitors obtained were somewhat greater than those from the endocytosis inhibition experiment. This indicates that cells, and specifically RAW 264.7 macrophages, can recover quickly from the effect of the inhibitors, taking into consideration the amount of time that the cells were incubated with inhibitors, as well as the duration of the nanoparticle uptake. This ability to recover quickly can be seen through the increase of the light scattering signal, as that indicates a higher uptake of nanoparticles compared to the endocytosis inhibition experiment. Therefore, these data suggest that longer incubation periods with inhibitors are likely to slow down how fast cells can recover from the effect of the inhibitors.

In order to further understand the cell recovery capabilities, as a future step, we would need to investigate this by performing the cell recovery experiment using flow cytometry.

Performing such various experiments is necessary, as, despite the current state of the art, we have yet to discover the full potential and capabilities of flow cytometry. Although

flow cytometry has been used for a long time, it was not until recently that it was incorporated into the field of nanomedicine. Hence, there are still many different aspects that still need investigation. Based on my research and readings, flow cytometry has not been used yet in kinetics analysis and endocytosis inhibition experiments, as the current studies are focusing on understanding the effects of surface modifications, and nanoparticle sizes on the side scattering signals, as well as further understanding the forward scattering signals. Therefore, by varying the experiments performed using flow cytometry and by expanding our knowledge, we would be able to study tumors and their microenvironment, thus, enhancing the nanoparticle delivery efficiency, and ultimately improving the field of nanomedicine.

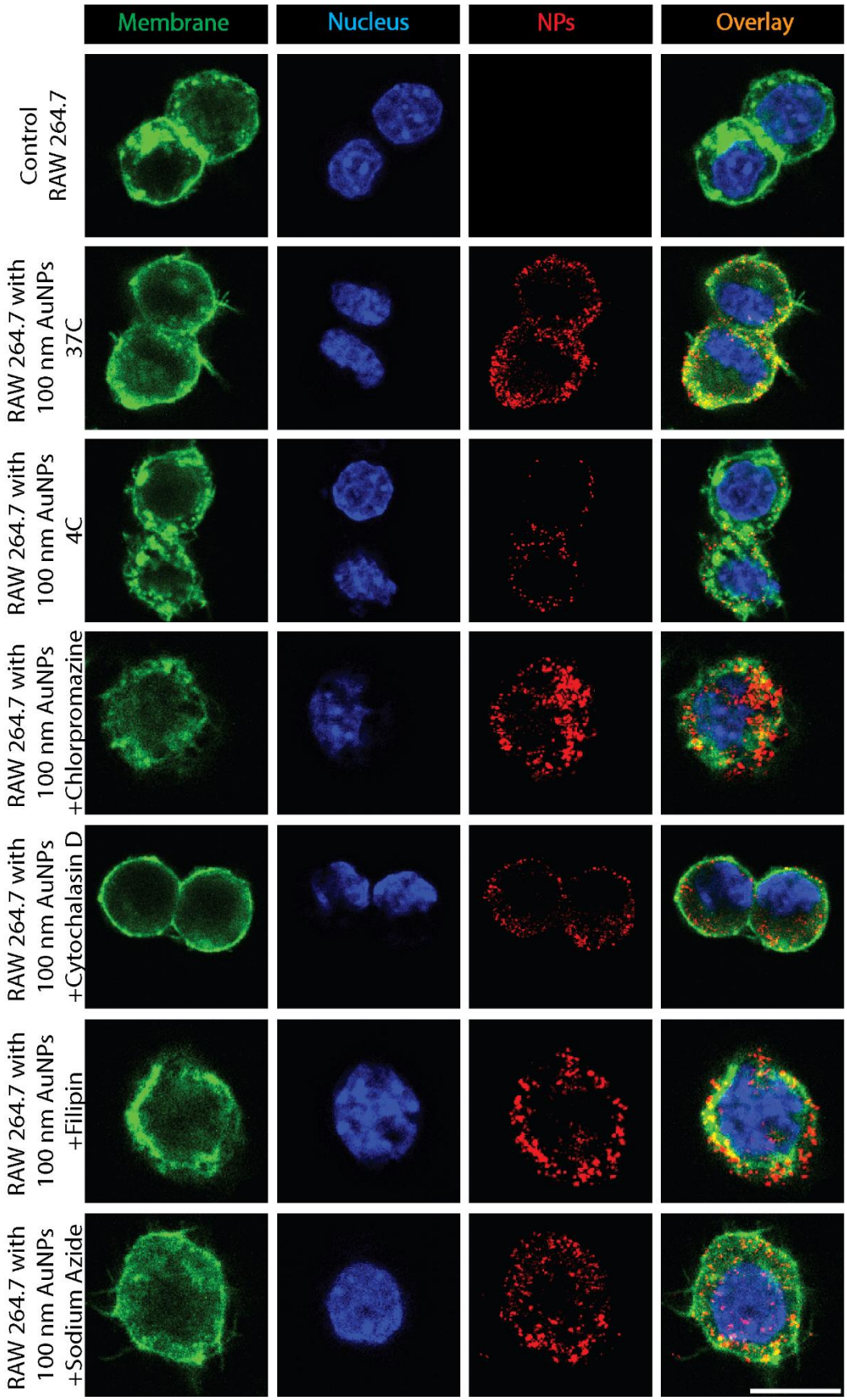
Membrane
Nucleus
NPs
Overlay
Control RAW 264.7
RAW 264.7 with 100 nm AuNPs 37C
RAW 264.7 with 100 nm AuNPs 4C
RAW 264.7 with 100 nm AuNPs +Chlorpromazine
RAW 264.7 with 100 nm AuNPs +Cytochalasin D
RAW 264.7 with 100 nm AuNPs +Filipin
RAW 264.7 with 100 nm AuNPs +Sodium Azide

Figure 19: Cell recovery and uptake of 100 nm AuNPs after the removal of inhibitors. Visualization of nanoparticle uptake through light scattering for RAW 264.7 with 100 nm AuNP performed by confocal laser scanning laser microscopy (CLSM). The different channels for the membrane, nucleus, and light scattering along with the overlay channel are shown for both the control and the experimental sample. Four different types of inhibitors were used, and the amount of light scattering signal was studied to determine how fast cells can recover from the inhibitors. All samples were performed in a duplicate. The scale bar = 10 μm.

Conclusion

In this study, we detailed current and innovative flow cytometry approaches for high-throughput analysis of single cells that can be applied to transform our understanding of nanoparticle-cell interactions. Flow cytometry techniques allow for the identification of nanoparticle presence and can be used to track differences in nanoparticle uptake or cell association based on shifts in light scattering signals. Despite that, the main limiting factor for conventional flow cytometry is the lack of imaging or imaging resolution that limits the understanding and visualization of cells at the single-level while they pass through the flow chamber. Published studies looked into applying imaging technologies as well as machine learning methods to better answer and understand questions regarding nano-bio cell interactions [47], [105], [119], [122], [123]. These methods are exciting avenues for flow cytometry to continue exploring to improve analysis options and workflows. These methods do not only enhance our understanding of nano-bio interactions, as well as the provided visualization of the behavior of the nanoparticles within cells, but they also allow for easier and faster analysis of large sets of data, thus providing increased efficiency.

Additionally, we demonstrated that the detection of nanoparticles and their effect on the complexity of the cell as well as the cellular behavior can be detected by flow cytometry. Furthermore, we showed that flow cytometry is not limited to a specific nanoparticle type, size or even cell line. With the use of CLSM, we saw that larger nanoparticles scatter more light than smaller ones, and that silver scatters more light than gold nanoparticles of the same size. Such data supported the SSC-A data obtained from the uptake of nanoparticles using the flow cytometer.

We were able to show that ICP-MS and CLSM data support the nanoparticle uptake trends in data shown in flow cytometry. Additionally, the kinetics behavior of the cells and the extent of nanoparticle uptake using FCM follow the trends seen in different papers [47], [182]–[184].

All these data were obtained using a label-free technique to avoid affecting the nano-bio interactions as adding a fluorescent tag to nanoparticles alters their surface chemistry and therefore how they would affect and interact with cells [147], [148]. With that in mind, flow cytometry is a promising method to analyze nano-bio interactions at the single-cell level. Additionally, the fact the flow cytometry is not limited to a specific cell line or nanoparticle system provides an opportunity to understand various nanoparticle systems apart from gold and silver nanoparticles, potentially liposomes and lipid nanoparticles. Since lipid nanoparticles and liposomes have a similar composition, and therefore, a similar refractive index to the cells, we will need to investigate if any changes in SSC and cellular complexity when using such nanoparticles would be possible through flow cytometry [185].

We anticipate that the research demonstrated in this study can be applied to research involving a variety of nanomedicine applications that enhance our understanding of nanoparticle-cell interactions. Moreover, using this method is less labor-intensive compared to ICP-MS and can be carried in a label-free way, thus creating a possibility for the development of more efficacious therapies for various diseases, such as cancer, potentially improving clinical results.

Future Directions

With the work done in this thesis, we were able to understand the effect of nano-bio interactions on cellular complexity and the kinetics of nanoparticle uptake in RAW 264.7 using flow cytometry as well as supporting techniques such as ICP-MS and CLSM. Despite that, we were not able to determine the uptake pathway for the HEP-coated 100 nm AuNPs and this experiment will need to be repeated to see if we see a similar trend to what we have obtained before.

Additionally, to understand the reason behind the increase in the side scattering signal for the flow data with the Cytochalasin D and Filipin conditions, we will need to investigate if that increase was due to the inhibitors being effective or not, and whether the concentration used for the inhibition experiment was not sufficient. Therefore, in order to do that, we should use 3-4 concentrations for each of the two inhibitors and run the samples on flow cytometry. In case a trend similar to what we have seen before is observed again across the different concentrations, as a next step we could use an etching agent, such as I_2/KI [186], to see if the increase in the SSC is due to nanoparticles that are stuck on the surface on the cell membrane, and which were not internalized within the cell. Since the etching agent allows us to get rid of nanoparticles on the surface of the cell, once the samples are run through the flow cytometer, any changes that occur in the side scattering signal would be due to the internalized nanoparticles. This would help us further understand how Cytochalasin D and Filipin work on blocking macropinocytosis and caveolae-mediated endocytosis.

In order to further examine the ability of FCM to analyze nano-bio interactions at the single-cell level, we will need to perform the kinetics analysis experiment using the 0.02

nM PEG-coated 100 nm AuNPs. This would allow us to see if the data obtained using flow cytometry would match or be similar to either the ICP-MS or CLSM data, as well as potentially understanding the reason behind the differences in the data obtained.

With that in mind, to take the endocytosis inhibition and kinetics analysis experiments to another level, we can vary the cell line and nanoparticle system. We can go back to using 4T1 cells, 65 nm and 40 nm AuNPs, as well as 30 nm AgNPs for the kinetics analysis. That way, we can see how the kinetics behavior of the cells change with the presence of different cell lines and nanoparticle systems, allowing us to relate that to the data we have obtained before from the flow cytometry generality experiment, which would help us in understand changes in nano-bio interactions. Moreover, when considering potential changes and improvements that could be done for the endocytosis inhibition experiment, we can alter the surface modifications used on the nanoparticles, such as adding BSA, and varying the nanoparticle size. This way we can determine how any changes in the surface chemistry and nanoparticle size affect the uptake pathways or whether such variations would not lead to any change in the nanoparticle uptake pathway.

One other experiment that could be done is the cell recovery experiment. Since we have obtained some data on that using CLSM, we will need to perform the cell recovery experiment, this time using flow cytometry. Not only will that allow us to examine the capabilities of flow cytometry, but we can also confirm if a trend similar to that of the CLSM data can be seen using flow cytometry.

Lastly, we can take the use of flow cytometry to analyze cells at the single-cell level to another degree by analyzing the distribution of nanoparticles in different cells of tissues that are broken down into single cell suspensions, by following the preparation and analysis

methods mentioned in Reichard *et al*.'s study [187]. This would allow us to improve our understanding of how cells from various tissues and organs interact differently with nanoparticles from each other. Such tissues and organs can be obtained from animal studies. Not only would that allow us to study using flow cytometry the bad clinical translation of nanomedicine in which only 0.7% of administered nanoparticles reach the tumor microenvironment [140], but we could establish and further explore the potential of flow cytometry. Suck knowledge along with the performance of more experiments, we will be able to get a stop closer towards enhancing the nanoparticle delivery efficiency, ultimately improving the field of nanomedicine.

Appendix

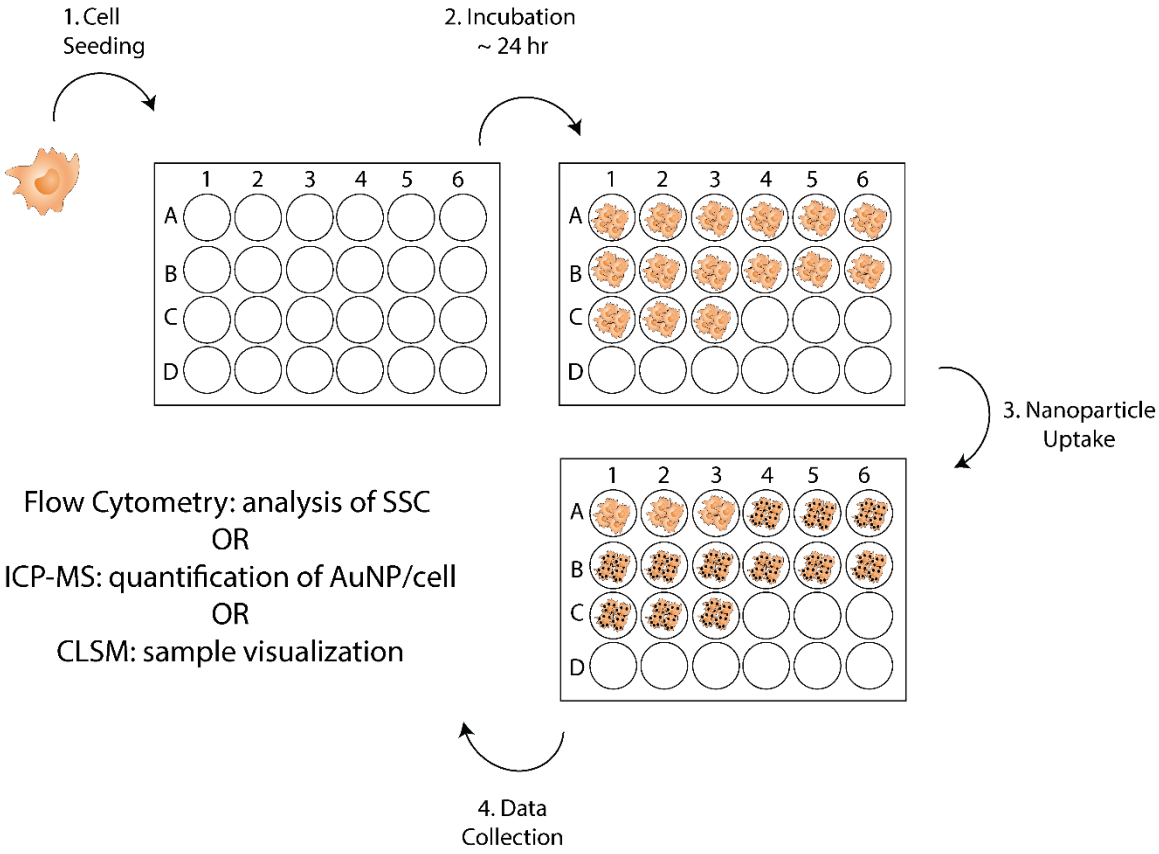

Figure 20: General Schematic of the Major Experimental Setups and Designs

References

[1] C. Zhang *et al.*, “Progress, challenges, and future of nanomedicine,” *Nano Today*, vol. 35. Elsevier B.V., 2020. doi: 10.1016/j.nantod.2020.101008.

[2] S. Đorđević *et al.*, “Current hurdles to the translation of nanomedicines from bench to the clinic,” *Drug Deliv Transl Res*, vol. 12, no. 3, pp. 500–525, 2022, doi: 10.1007/s13346-021-01024-2.

[3] S. Mo *et al.*, “Patient-Derived Organoids from Colorectal Cancer with Paired Liver Metastasis Reveal Tumor Heterogeneity and Predict Response to Chemotherapy,” *Advanced Science*, vol. 9, no. 31, 2022, doi: 10.1002/advs.202204097.

[4] S. Soares, J. Sousa, A. Pais, and C. Vitorino, “Nanomedicine: Principles, properties, and regulatory issues,” *Frontiers in Chemistry*, vol. 6, no. AUG. Frontiers Media S.A., Aug. 01, 2018. doi: 10.3389/fchem.2018.00360.

[5] X. Hu, Y. Zhang, T. Ding, J. Liu, and H. Zhao, “Multifunctional Gold Nanoparticles: A Novel Nanomaterial for Various Medical Applications and Biological Activities,” *Frontiers in Bioengineering and Biotechnology*, vol. 8. Frontiers Media S.A., Aug. 13, 2020. doi: 10.3389/fbioe.2020.00990.

[6] A. C. Anselmo and S. Mitragotri, “Nanoparticles in the clinic,” *Bioeng Transl Med*, vol. 1, no. 1, pp. 10–29, Mar. 2016, doi: 10.1002/btm2.10003.

[7] N. R. S. Sibuyi *et al.*, “Multifunctional Gold Nanoparticles for Improved Diagnostic and Therapeutic Applications: A Review,” *Nanoscale Research Letters*, vol. 16, no. 1. Springer, 2021. doi: 10.1186/s11671-021-03632-w.

[8] M. J. Mitchell, M. M. Billingsley, R. M. Haley, M. E. Wechsler, N. A. Peppas, and R. Langer, “Engineering precision nanoparticles for drug delivery,” *Nature Reviews Drug Discovery*, vol. 20, no. 2. Nature Research, pp. 101–124, Feb. 01, 2021. doi: 10.1038/s41573-020-0090-8.

[9] S. Hua, M. B. C. de Matos, J. M. Metselaar, and G. Storm, “Current trends and challenges in the clinical translation of nanoparticulate nanomedicines: Pathways for translational development and commercialization,” *Frontiers in Pharmacology*, vol. 9, no. JUL. Frontiers Media S.A., 2018. doi: 10.3389/fphar.2018.00790.

[10] J. J. Rennick, A. P. R. Johnston, and R. G. Parton, “Key principles and methods for studying the endocytosis of biological and nanoparticle therapeutics,” *Nature Nanotechnology*, vol. 16, no. 3. Nature Research, pp. 266–276, 2021. doi: 10.1038/s41565-021-00858-8.

[11] P. Foroozandeh and A. A. Aziz, “Insight into Cellular Uptake and Intracellular Trafficking of Nanoparticles,” *Nanoscale Research Letters*, vol. 13. Springer New York LLC, 2018. doi: 10.1186/s11671-018-2728-6.

[12] M. P. Vincent *et al.*, “Surface chemistry-mediated modulation of adsorbed albumin folding state specifies nanocarrier clearance by distinct macrophage subsets,” *Nat Commun*, vol. 12, no. 1, Dec. 2021, doi: 10.1038/s41467-020-20886-7.

[13] J. Yue, T. J. Feliciano, W. Li, A. Lee, and T. W. Odom, “Gold Nanoparticle Size and Shape Effects on Cellular Uptake and Intracellular Distribution of siRNA Nanoconstructs,” *Bioconjug Chem*, vol. 28, no. 6, pp. 1791–1800, Jun. 2017, doi: 10.1021/acs.bioconjchem.7b00252.

[14] A. Abdelkhaliq *et al.*, “Impact of nanoparticle surface functionalization on the protein corona and cellular adhesion, uptake and transport 03 Chemical Sciences 0306 Physical Chemistry (incl. Structural),” *J Nanobiotechnology*, vol. 16, no. 1, Sep. 2018, doi: 10.1186/s12951-018-0394-6.

[15] C. D. Walkey, J. B. Olsen, H. Guo, A. Emili, and W. C. W. Chan, “Nanoparticle size and surface chemistry determine serum protein adsorption and macrophage uptake,” *J Am Chem Soc*, vol. 134, no. 4, pp. 2139–2147, Feb. 2012, doi: 10.1021/ja2084338.

[16] M. Wu, H. Guo, L. Liu, Y. Liu, and L. Xie, “Size-dependent cellular uptake and localization profiles of silver nanoparticles,” *Int J Nanomedicine*, vol. 14, pp. 4247–4259, 2019, doi: 10.2147/IJN.S201107.

[17] A. N. Frickenstein *et al.*, “Mesoporous silica nanoparticles: Properties and strategies for enhancing clinical effect,” *Pharmaceutics*, vol. 13, no. 4. MDPI AG, Apr. 01, 2021. doi: 10.3390/pharmaceutics13040570.

[18] X. Xie, J. Liao, X. Shao, Q. Li, and Y. Lin, “The Effect of shape on Cellular Uptake of Gold Nanoparticles in the forms of Stars, Rods, and Triangles,” *Sci Rep*, vol. 7, no. 1, Dec. 2017, doi: 10.1038/s41598-017-04229-z.

[19] A. Murschhauser *et al.*, “A high-throughput microscopy method for single-cell analysis of event-time correlations in nanoparticle-induced cell death,” *Commun Biol*, vol. 2, no. 1, p. 35, 2019, doi: 10.1038/s42003-019-0282-0.

[20] M. Steinke *et al.*, “Rapid Analysis of Cell–Nanoparticle Interactions using Single-Cell Raman Trapping Microscopy,” *Angewandte Chemie International Edition*, vol. 57, no. 18, pp. 4946–4950, Apr. 2018, doi: https://doi.org/10.1002/anie.201713151.

[21] F. Wang *et al.*, “Microscopic inspection and tracking of single upconversion nanoparticles in living cells,” *Light Sci Appl*, vol. 7, no. 4, p. 18007, 2018, doi: 10.1038/lsa.2018.7.

[22] K. M. McKinnon, “Flow cytometry: An Overview,” *Curr Protoc Immunol*, pp. 1–5, 2019, doi: 10.1002/cpim.40.

[23] A. Adan, G. Alizada, Y. Kiraz, Y. Baran, and A. Nalbant, “Flow cytometry: basic principles and applications,” *Crit Rev Biotechnol*, vol. 37, no. 2, pp. 163–176, 2017, doi: 10.3109/07388551.2015.1128876.

[24] S. Wilhelm, R. Bensen, R. Kothapalli, A. Burgett, R. Merrifield, and C. Stephan, “Quantification of Gold Nanoparticle Uptake into Cancer Cells using Single Cell ICP-MS,”

PerkinElmer Appl Note, 2018, Accessed: Feb. 14, 2023. [Online]. Available: https://resources.perkinelmer.com/lab-solutions/resources/docs/app_014276_01_nexion_sc-icp-ms_np_uptake_in_cancer_cells.pdf

[25] N. D. Donahue *et al.*, "Absolute Quantification of Nanoparticle Interactions with Individual Human B Cells by Single Cell Mass Spectrometry," *Cite This: Nano Lett*, vol. 2022, p. 4199, 2022, doi: 10.1021/acs.nanolett.2c01037.

[26] J. M. Njoroge, J. J. Yourick, and M. A. Principato, "A flow cytometric analysis of macrophage– nanoparticle interactions in vitro: Induction of altered Toll-like receptor expression," *Int J Nanomedicine*, vol. 13, pp. 8365–8378, 2018, doi: 10.2147/IJN.S174184.

[27] R. M. Zucker, K. M. Daniel, E. J. Massaro, S. J. Karafas, L. L. Degn, and W. K. Boyes, "Detection of Silver Nanoparticles in Cells by Flow Cytometry Using Light Scatter and Far-Red Fluorescence," *Journal of Quantitative Cell Science*, vol. 83, no. 10, pp. 962–972, 2013, doi: 10.1002/cyto.22342.

[28] R. M. Zucker, J. Ortenzio, L. L. Degn, J. M. Lerner, and W. K. Boyes, "Biophysical comparison of four silver nanoparticles coatings using microscopy, hyperspectral imaging and flow cytometry," *PLoS One*, vol. 14, no. 7, 2019, doi: 10.1371/journal.pone.0219078.

[29] Y. Wu, M. R. K. Ali, K. Dansby, and M. A. El-Sayed, "Improving the Flow Cytometry-based Detection of the Cellular Uptake of Gold Nanoparticles," *Anal Chem*, vol. 91, no. 22, pp. 14261–14267, 2019, doi: 10.1021/acs.analchem.9b02248.

[30] J. Park, M. K. Ha, N. Yang, and T. H. Yoon, "Flow Cytometry-Based Quantification of Cellular Au Nanoparticles," *Anal Chem*, vol. 89, no. 4, pp. 2449–2456, 2017, doi: 10.1021/acs.analchem.6b04418.

[31] A. Jochums, E. Friehs, F. Sambale, A. Lavrentieva, D. Bahnemann, and T. Scheper, "Revelation of different nanoparticle-uptake behavior in two standard cell lines NIH/3T3 and A549 by flow cytometry and time-lapse imaging," *Toxics*, vol. 5, no. 3, 2017, doi: 10.3390/toxics5030015.

[32] A. Kumar, A. K. Pandey, S. S. Singh, R. Shanker, and A. Dhawan, "A flow cytometric method to assess nanoparticle uptake in bacteria," *Cytometry Part A*, vol. 79 A, no. 9, pp. 707–712, 2011, doi: 10.1002/cyto.a.21085.

[33] A. R. Arze, N. Manier, A. Chatel, and C. Mouneyrac, "Characterization of the nano-bio interaction between metallic oxide nanomaterials and freshwater microalgae using flow cytometry," *Nanotoxicology*, vol. 14, no. 8, pp. 1082–1095, 2020, doi: 10.1080/17435390.2020.1808106ï.

[34] F. Muraca, L. Boselli, V. Castagnola, and K. A. Dawson, "Ultrasmall Gold Nanoparticle Cellular Uptake: Influence of Transient Bionano Interactions," *ACS Appl Bio Mater*, vol. 3, no. 6, pp. 3800–3808, 2020, doi: 10.1021/acsabm.0c00379.

[35] X. Wan *et al.*, “The ultrasmall biocompatible CuS@BSA nanoparticle and its photothermal effects,” *Front Pharmacol*, vol. 10, no. FEB, 2019, doi: 10.3389/fphar.2019.00141.

[36] M. Youhannayee *et al.*, “Physical characterization and uptake of iron oxide nanoparticles of different prostate cancer cells,” *J Magn Magn Mater*, vol. 473, pp. 205–214, 2019, doi: 10.1016/J.JMMM.2018.10.062.

[37] B. Chen, Y. Wang, Y. Guo, P. Shi, and F. Wang, “NaYbF4@NaYF4Nanoparticles: Controlled shell growth and shape-dependent cellular uptake,” *ACS Appl Mater Interfaces*, vol. 13, no. 2, pp. 2327–2335, 2021, doi: 10.1021/acsami.0c20757.

[38] H. Shin, M. Kwak, T. G. Lee, and J. Y. Lee, “Quantifying the level of nanoparticle uptake in mammalian cells using flow cytometry,” *Nanoscale*, vol. 12, pp. 15743–15751, 2020, doi: 10.1039/d0nr01627f.

[39] H. Garcia Romeu, S. Deville, and A. Salvati, “Time- and Space-Resolved Flow-Cytometry of Cell Organelles to Quantify Nanoparticle Uptake and Intracellular Trafficking by Cells,” *Small*, vol. 17, no. 34, 2021, doi: 10.1002/smll.202100887.

[40] J. Khetan, M. Shahinuzzaman, S. Barua, and D. Barua, “Quantitative Analysis of the Correlation between Cell Size and Cellular Uptake of Particles,” *Biophys J*, vol. 116, no. 2, pp. 347–359, 2019, doi: 10.1016/j.bpj.2018.11.3134.

[41] C. P. Carney *et al.*, “Fn14-Directed DART Nanoparticles Selectively Target Neoplastic Cells in Preclinical Models of Triple-Negative Breast Cancer Brain Metastasis,” *Mol Pharm*, vol. 20, no. 1, pp. 314–330, 2023, doi: 10.1021/acs.molpharmaceut.2c00663.

[42] Z. Li *et al.*, “A Multispectral Photoacoustic Tracking Strategy for Wide-Field and Real-Time Monitoring of Macrophages in Inflammation,” *Anal Chem*, vol. 93, no. 24, pp. 8467–8475, 2021, doi: 10.1021/acs.analchem.1c00690.

[43] Y. Wang *et al.*, “Targeted Therapy of Atherosclerosis by a Broad-Spectrum Reactive Oxygen Species Scavenging Nanoparticle with Intrinsic Anti-inflammatory Activity,” *ACS Nano*, vol. 12, no. 9, pp. 8943–8960, 2018, doi: 10.1021/acsnano.8b02037.

[44] E. Puente-Massaguer, P. Saccardo, N. Ferrer-Miralles, M. Lecina, and F. Gòdia, “Coupling Microscopy and Flow Cytometry for a Comprehensive Characterization of Nanoparticle Production in Insect Cells,” *Cytometry Part A*, vol. 97, no. 9, pp. 921–932, 2020, doi: 10.1002/cyto.a.24033.

[45] S. Vranic *et al.*, “Deciphering the mechanisms of cellular uptake of engineered nanoparticles by accurate evaluation of internalization using imaging flow cytometry,” *Part Fibre Toxicol*, vol. 10, no. 1, 2013, doi: 10.1186/1743-8977-10-2.

[46] T. Jin *et al.*, “On-Chip Multicolor Photoacoustic Imaging Flow Cytometry,” *Anal Chem*, vol. 93, no. 23, pp. 8134–8142, 2021, doi: 10.1021/acs.analchem.0c05218.

[47] B. J. Jurgielewicz, Y. Yao, and S. L. Stice, “Kinetics and Specificity of HEK293T Extracellular Vesicle Uptake using Imaging Flow Cytometry,” *Nanoscale Res Lett*, vol. 15, no. 1, 2020, doi: 10.1186/s11671-020-03399-6.

[48] A. Görgens *et al.*, “Optimisation of imaging flow cytometry for the analysis of single extracellular vesicles by using fluorescence-tagged vesicles as biological reference material,” *J Extracell Vesicles*, vol. 8, no. 1, 2019, doi: 10.1080/20013078.2019.1587567.

[49] J. F. Lusk, C. Miranda, and B. S. Smith, “Ovarian cancer detection using photoacoustic flow cytometry,” *Journal of Visualized Experiments*, vol. 2020, no. 155, 2019, doi: 10.3791/60279.

[50] J. F. Lusk, C. Miranda, M. Howell, M. Chrest, J. Eshima, and B. S. Smith, “Photoacoustic Flow System for the Detection of Ovarian Circulating Tumor Cells Utilizing Copper Sulfide Nanoparticles,” *ACS Biomater Sci Eng*, vol. 5, no. 3, pp. 1553–1560, 2019, doi: 10.1021/acsbiomaterials.8b01217.

[51] D. A. Nedosekin *et al.*, “Photoacoustic flow cytometry for nanomaterial research,” *Photoacoustics*, vol. 6, pp. 16–25, 2017, doi: 10.1016/J.PACS.2017.03.002.

[52] K. Bhattacharyya, B. Goldschmidt, and J. Viator, “Detection and capture of breast cancer cells with photoacoustic flow cytometry,” *J Biomed Opt*, vol. 21, no. 8, p. 87007, 2016, doi: 10.1117/1.jbo.21.8.087007.

[53] A. Sun *et al.*, “Acoustic Standing Wave Aided Multiparametric Photoacoustic Imaging Flow Cytometry,” *Anal Chem*, vol. 93, no. 44, pp. 14820–14827, 2021, doi: 10.1021/acs.analchem.1c03713.

[54] D. A. Nedosekin *et al.*, “In vivo noninvasive analysis of graphene nanomaterial pharmacokinetics using photoacoustic flow cytometry,” *Journal of Applied Toxicology*, vol. 37, no. 11, pp. 1297–1304, 2017, doi: 10.1002/jat.3467.

[55] D. A. Nedosekin *et al.*, “In vivo plant flow cytometry: A first proof-of-concept,” *Cytometry Part A*, vol. 79 A, no. 10, pp. 855–865, 2011, doi: 10.1002/cyto.a.21128.

[56] E. I. Galanzha and V. P. Zharov, “Circulating Tumor Cell Detection and Capture by Photoacoustic Flow Cytometry in Vivo and ex Vivo,” *Cancers*, vol. 5, no. 4. MDPI, pp. 1691–1738, 2013. doi: 10.3390/cancers5041691.

[57] E. I. Galanzha, E. v Shashkov, P. M. Spring, J. Y. Suen, and V. P. Zharov, “In vivo, noninvasive, label-free detection and eradication of circulating metastatic melanoma cells using two-color photoacoustic flow cytometry with a diode laser,” *Cancer Res*, vol. 69, no. 20, pp. 7926–7934, 2009, doi: 10.1158/0008-5472.CAN-08-4900.

[58] E. I. Galanzha, E. v Shashkov, T. Kelly, J. W. Kim, L. Yang, and V. P. Zharov, “In vivo magnetic enrichment and multiplex photoacoustic detection of circulating tumour cells,” *Nat Nanotechnol*, vol. 4, no. 12, pp. 855–860, 2009, doi: 10.1038/nnano.2009.333.

[59] D. Wei *et al.*, “Noninvasive monitoring of nanoparticle clearance and aggregation in blood circulation by in vivo flow cytometry,” *Journal of Controlled Release*, vol. 278, pp. 66–73, 2018, doi: 10.1016/J.JCONREL.2018.03.024.

[60] J. Yao *et al.*, “Neovasculature and circulating tumor cells dual-targeting nanoparticles for the treatment of the highly-invasive breast cancer,” *Biomaterials*, vol. 113, pp. 1–17, 2017, doi: 10.1016/J.BIOMATERIALS.2016.10.033.

[61] V. P. Zharov, E. I. Galanzha, E. v Shashkov, J.-W. Kim, N. G. Khlebtsov, and V. v Tuchin, “Photoacoustic flow cytometry: principle and application for real-time detection of circulating single nanoparticles, pathogens, and contrast dyes in vivo,” *J Biomed Opt*, vol. 12, no. 5, p. 51503, 2007, doi: 10.1117/1.2793746.

[62] D. R. A. Stephen P. Perfetto Richard Nguyen Mario Roederer Richard A. Koup Kevin L. Holmes, *Flow Cytometry Protocols - Third Edition*, 3rd ed., vol. 699. Humana Press, 2010. doi: https://doi.org/10.1007/978-1-61737-950-5_1.

[63] G. Maruccio, M. A. Qasaimeh, A. Vembadi, and A. Menachery, “Cell Cytometry: Review and Perspective on Biotechnological Advances,” *Cell Cytometry: Review and Perspective on Biotechnological Advances. Front. Bioeng. Biotechnol*, vol. 7, p. 147, 2019, doi: 10.3389/fbioe.2019.00147.

[64] L. de Rond *et al.*, “A Systematic Approach to Improve Scatter Sensitivity of a Flow Cytometer for Detection of Extracellular Vesicles,” *Cytometry Part A*, vol. 97, no. 6, pp. 582–591, Jun. 2020, doi: https://doi.org/10.1002/cyto.a.23974.

[65] M. Ghosh *et al.*, “Cyto-genotoxic and DNA methylation changes induced by different crystal phases of TiO2-np in bronchial epithelial (16-HBE) cells,” *Mutation Research/Fundamental and Molecular Mechanisms of Mutagenesis*, vol. 796, pp. 1–12, 2017, doi: 10.1016/J.MRFMMM.2017.01.003.

[66] J. Park, M. K. Ha, N. Yang, and T. H. Yoon, “Flow Cytometry-Based Quantification of Cellular Au Nanoparticles,” *Anal Chem*, vol. 89, no. 4, pp. 2449–2456, 2017, doi: 10.1021/acs.analchem.6b04418.

[67] Y. Ibuki and T. Toyooka, “Nanoparticle Uptake Measured by Flow Cytometry,” in *Nanotoxicity*, 2012, pp. 157–166. doi: 10.1007/978-1-62703-002-1_11.

[68] L. Taccola *et al.*, “Zinc oxide nanoparticles as selective killers of proliferating cells,” *Int J Nanomedicine*, vol. 6, pp. 1129–1140, Dec. 2011, doi: 10.2147/IJN.S16581.

[69] R. Chakraborty, D. Leshem-Lev, R. Kornowski, and D. Fixler, “The Scattering of Gold Nanorods Combined with Differential Uptake, Paving a New Detection Method for Macrophage Subtypes Using Flow Cytometery,” *Nano Lett*, vol. 20, no. 11, pp. 8360–8368, 2020, doi: 10.1021/acs.nanolett.0c03525.

[70] N. D. Donahue *et al.*, “Absolute Quantification of Nanoparticle Interactions with Individual Human B Cells by Single Cell Mass Spectrometry,” *Nano Lett*, vol. 22, no. 10, pp. 4192–4199, May 2022, doi: 10.1021/acs.nanolett.2c01037.

[71] J. C. Lee *et al.*, “Exploring Maleimide-Based Nanoparticle Surface Engineering to Control Cellular Interactions,” *ACS Appl Nano Mater*, vol. 3, no. 3, pp. 2421–2429, Jun. 2020, doi: 10.1021/acsanm.9b02541.

[72] M. A. Rodrigues, L. A. Beaton-Green, R. C. Wilkins, and M. F. Fenech, “The potential for complete automated scoring of the cytokinesis block micronucleus cytome assay using imaging flow cytometry,” *Mutation Research - Genetic Toxicology and Environmental Mutagenesis*, vol. 836. Elsevier B.V., pp. 53–64, 2018. doi: 10.1016/j.mrgentox.2018.05.003.

[73] M. G. H. Pelletier, K. Szymczak, A. M. Barbeau, G. N. Prata, K. S. O’Fallon, and P. Gaines, “Characterization of neutrophils and macrophages from ex vivo-cultured murine bone marrow for morphologic maturation and functional responses by imaging flow cytometry,” *Methods*, vol. 112, pp. 124–146, 2017, doi: 10.1016/j.ymeth.2016.09.005.

[74] J. Lannigan and U. Erdbruegger, “Imaging flow cytometry for the characterization of extracellular vesicles,” *Methods*, vol. 112, pp. 55–67, 2017, doi: 10.1016/j.ymeth.2016.09.018.

[75] S. M. Manohar, P. Shah, and A. Nair, “Flow cytometry: Principles, applications and recent advances,” *Bioanalysis*, vol. 13, no. 3. Future Medicine Ltd., pp. 185–202, 2021. doi: 10.4155/bio-2020-0267.

[76] K. T. Soh and P. K. Wallace, “RNA flow cytometry using the branched DNA technique,” in *Methods in Molecular Biology*, Humana Press Inc., 2018, pp. 49–77. doi: 10.1007/978-1-4939-7346-0_4.

[77] X. Li *et al.*, “A Microfluidic Fluorescent Flow Cytometry Capable of Quantifying Cell Sizes and Numbers of Specific Cytosolic Proteins,” *Sci Rep*, vol. 8, no. 1, 2018, doi: 10.1038/s41598-018-32333-1.

[78] L. Ferrer-Font, C. Pellefigues, J. U. Mayer, S. J. Small, M. C. Jaimes, and K. M. Price, “Panel Design and Optimization for High-Dimensional Immunophenotyping Assays Using Spectral Flow Cytometry,” *Curr Protoc Cytom*, vol. 92, no. 1, 2020, doi: 10.1002/cpcy.70.

[79] L. Ferrer-Font *et al.*, “High-dimensional analysis of intestinal immune cells during helminth infection,” *Elife*, vol. 9, 2020, doi: 10.7554/eLife.51678.

[80] A. Rossi, I. Pacella, and S. Piconese, “RNA Flow Cytometry for the Study of T Cell Metabolism,” *Int J Mol Sci*, vol. 22, no. 8, 2021, doi: 10.3390/ijms22083906.

[81] A. P. Frei *et al.*, “Highly multiplexed simultaneous detection of RNAs and proteins in single cells,” *Nat Methods*, vol. 13, no. 3, pp. 269–275, Feb. 2016, doi: 10.1038/nmeth.3742.

[82] M. B. Hanley, W. Lomas, D. Mittar, V. Maino, and E. Park, “Detection of Low Abundance RNA Molecules in Individual Cells by Flow Cytometry,” *PLoS One*, vol. 8, no. 2, Feb. 2013, doi: 10.1371/journal.pone.0057002.

[83] D. L. Bonilla, G. Reinin, and E. Chua, “Full Spectrum Flow Cytometry as a Powerful Technology for Cancer Immunotherapy Research,” *Frontiers in Molecular Biosciences*, vol. 7. Frontiers Media S.A., 2021. doi: 10.3389/fmolb.2020.612801.

[84] L. Li *et al.*, “Development of Spectral Nano-Flow Cytometry for High-Throughput Multiparameter Analysis of Individual Biological Nanoparticles,” *Anal Chem*, 2022, doi: 10.1021/acs.analchem.2c05159.

[85] L. M. Park, J. Lannigan, and M. C. Jaimes, “OMIP-069: Forty-Color Full Spectrum Flow Cytometry Panel for Deep Immunophenotyping of Major Cell Subsets in Human Peripheral Blood,” *Cytometry Part A*, vol. 97, no. 10, pp. 1044–1051, 2020, doi: 10.1002/cyto.a.24213.

[86] J. P. Nolan, “The evolution of spectral flow cytometry,” *Cytometry Part A*, vol. 101, no. 10. John Wiley and Sons Inc, pp. 812–817, 2022. doi: 10.1002/cyto.a.24566.

[87] Y. Tian *et al.*, “Refractive Index Determination of Individual Viruses and Small Extracellular Vesicles in Aqueous Media Using Nano-Flow Cytometry,” *Anal Chem*, vol. 94, no. 41, pp. 14299–14307, 2022, doi: 10.1021/acs.analchem.2c02833.

[88] K. Gao, H. Lian, C. Xue, J. Zhou, and X. Yan, “High-Throughput Counting and Sizing of Therapeutic Protein Aggregates in the Nanometer Size Range by Nano-Flow Cytometry,” *Anal Chem*, vol. 94, no. 50, pp. 17634–17644, 2022, doi: 10.1021/acs.analchem.2c04382.

[89] H. Liu, Y. Tian, C. Xue, Q. Niu, C. Chen, and X. Yan, “Analysis of extracellular vesicle DNA at the single-vesicle level by nano-flow cytometry,” *J Extracell Vesicles*, vol. 11, no. 4, 2022, doi: 10.1002/jev2.12206.

[90] Q. Niu *et al.*, “Quantitative Assessment of the Physical Virus Titer and Purity by Ultrasensitive Flow Virometry,” *Angewandte Chemie - International Edition*, vol. 60, no. 17, pp. 9351–9356, 2021, doi: 10.1002/anie.202100872.

[91] H. Lian, S. He, C. Chen, and X. Yan, “Flow Cytometric Analysis of Nanoscale Biological Particles and Organelles,” *Annual Review of Analytical Chemistry*, vol. 12, pp. 389–409, 2019, doi: 10.1146/annurev-anchem-061318-115042.

[92] K. M. Danielson *et al.*, “Diurnal variations of circulating extracellular vesicles measured by nano flow cytometry,” *PLoS One*, vol. 11, no. 1, 2016, doi: 10.1371/journal.pone.0144678.

[93] J. P. Nolan and D. Condello, “Spectral flow cytometry,” *Curr Protoc Cytom*, no. SUPPL.63, 2013, doi: 10.1002/0471142956.cy0127s63.

[94] Y. Tian *et al.*, “Quality and efficiency assessment of six extracellular vesicle isolation methods by nano-flow cytometry,” *J Extracell Vesicles*, vol. 9, no. 1, 2020, doi: 10.1080/20013078.2019.1697028.

[95] D. Choi, L. Montermini, H. Jeong, S. Sharma, B. Meehan, and J. Rak, “Mapping Subpopulations of Cancer Cell-Derived Extracellular Vesicles and Particles by Nano-Flow Cytometry,” *ACS Nano*, vol. 13, no. 9, pp. 10499–10511, 2019, doi: 10.1021/acsnano.9b04480.

[96] G. Holzner *et al.*, “High-throughput multiparametric imaging flow cytometry: toward diffraction-limited sub-cellular detection and monitoring of sub-cellular processes,” *Cell Rep*, vol. 34, no. 10, p. 108824, 2021, doi: 10.1016/J.CELREP.2021.108824.

[97] D. A. Basiji, W. E. Ortyn, L. Liang, V. Venkatachalam, and P. Morrissey, “Cellular Image Analysis and Imaging by Flow Cytometry,” *Clinics in Laboratory Medicing*, vol. 27, no. 3, pp. 653–670, 2007, doi: 10.1016/j.cll.2007.05.008.

[98] G. Wu *et al.*, “Single-cell extracellular vesicle analysis by microfluidics and beyond,” *TrAC Trends in Analytical Chemistry*, vol. 159, p. 116930, 2023, doi: 10.1016/J.TRAC.2023.116930.

[99] D. M. D. Siu *et al.*, “Deep-learning-assisted biophysical imaging cytometry at massive throughput delineates cell population heterogeneity,” *Lab Chip*, vol. 20, no. 20, pp. 3696–3708, 2020, doi: 10.1039/d0lc00542h.

[100] S. Stavrakis, G. Holzner, J. Choo, and A. deMello, “High-throughput microfluidic imaging flow cytometry,” *Current Opinion in Biotechnology*, vol. 55. Elsevier Ltd, pp. 36–43, 2019. doi: 10.1016/j.copbio.2018.08.002.

[101] Y. Han, Y. Gu, A. C. Zhang, and Y. H. Lo, “Review: Imaging technologies for flow cytometry,” *Lab on a Chip*, vol. 16, no. 24. Royal Society of Chemistry, pp. 4639–4647, 2016. doi: 10.1039/c6lc01063f.

[102] P. Rees, H. D. Summers, A. Filby, A. E. Carpenter, and M. Doan, “Imaging flow cytometry,” *Nature Reviews Methods Primers*, vol. 2, no. 1, 2022, doi: 10.1038/s43586-022-00167-x.

[103] T. K. Kaiser *et al.*, “Highly selective organ distribution and cellular uptake of inorganic-organic hybrid nanoparticles customized for the targeted delivery of glucocorticoids,” *Journal of Controlled Release*, vol. 319, pp. 360–370, Mar. 2020, doi: 10.1016/J.JCONREL.2020.01.010.

[104] T. Blasi *et al.*, “Label-free cell cycle analysis for high-throughput imaging flow cytometry,” *Nat Commun*, vol. 7, 2016, doi: 10.1038/ncomms10256.

[105] M. Lippeveld *et al.*, “Classification of Human White Blood Cells Using Machine Learning for Stain-Free Imaging Flow Cytometry,” *Cytometry Part A*, vol. 97, no. 3, pp. 308–319, 2020, doi: 10.1002/cyto.a.23920.

[106] J. Botha, H. R. Pugsley, and A. Handberg, “Conventional, high-resolution and imaging flow cytometry: Benchmarking performance in characterisation of extracellular vesicles,” *Biomedicines*, vol. 9, no. 2, pp. 1–24, 2021, doi: 10.3390/biomedicines9020124.

[107] L. Wu *et al.*, “Isolation-free measurement of single urinary extracellular vesicles by imaging flow cytometry,” *Nanomedicine*, vol. 48, p. 102638, 2023, doi: 10.1016/J.NANO.2022.102638.

[108] W. W. Woud *et al.*, “An imaging flow cytometry-based methodology for the analysis of single extracellular vesicles in unprocessed human plasma,” *Commun Biol*, vol. 5, no. 1, 2022, doi: 10.1038/s42003-022-03569-5.

[109] F. L. Ricklefs *et al.*, “Imaging flow cytometry facilitates multiparametric characterization of extracellular vesicles in malignant brain tumours,” *J Extracell Vesicles*, vol. 8, no. 1, 2019, doi: 10.1080/20013078.2019.1588555.

[110] T. Tertel, A. Görgens, and B. Giebel, “Analysis of individual extracellular vesicles by imaging flow cytometry,” *Methods Enzymol*, vol. 645, pp. 55–78, 2020, doi: 10.1016/BS.MIE.2020.05.013.

[111] Y. Ofir-Birin, P. Abou karam, A. Rudik, T. Giladi, Z. Porat, and N. Regev-Rudzki, “Monitoring extracellular vesicle cargo active uptake by imaging flow cytometry,” *Front Immunol*, vol. 9, no. MAY, 2018, doi: 10.3389/fimmu.2018.01011.

[112] K. O’Brien, K. Breyne, S. Ughetto, L. C. Laurent, and X. O. Breakefield, “RNA delivery by extracellular vesicles in mammalian cells and its applications,” *Nature Reviews Molecular Cell Biology*, vol. 21, no. 10. Nature Research, pp. 585–606, 2020. doi: 10.1038/s41580-020-0251-y.

[113] L. Czernek and M. Düchler, “Functions of Cancer-Derived Extracellular Vesicles in Immunosuppression,” *Archivum Immunologiae et Therapiae Experimentalis*, vol. 65, no. 4. Birkhauser Verlag AG, pp. 311–323, 2017. doi: 10.1007/s00005-016-0453-3.

[114] M. Malloci *et al.*, “Extracellular Vesicles: Mechanisms in Human Health and Disease,” *Antioxidants and Redux Signaling*, vol. 30, no. 6, 2019, doi: 10.1089/ars.2017.7265.

[115] M. Takasugi, “Emerging roles of extracellular vesicles in cellular senescence and aging,” *Aging Cell*, vol. 17, no. 2. Blackwell Publishing Ltd, 2018. doi: 10.1111/acel.12734.

[116] S. Mastoridis, G. M. Bertolino, G. Whitehouse, F. Dazzi, A. Sanchez-Fueyo, and M. Martinez-Llordella, “Multiparametric analysis of circulating exosomes and other small extracellular vesicles by advanced imaging flow cytometry,” *Front Immunol*, vol. 9, no. JUL, Jul. 2018, doi: 10.3389/fimmu.2018.01583.

[117] N. Nitta *et al.*, “Intelligent Image-Activated Cell Sorting,” *Cell*, vol. 175, no. 1, pp. 266-276.e13, Sep. 2018, doi: 10.1016/j.cell.2018.08.028.

[118] D. Schraivogel *et al.*, “High-speed fluorescence image-enabled cell sorting,” *Science (1979)*, vol. 375, no. 6578, pp. 315–320, 2022, doi: 10.1126/science.abj3013.

[119] Y. Gu, A. C. Zhang, Y. Han, J. Li, C. Chen, and Y. H. Lo, “Machine Learning Based Real-Time Image-Guided Cell Sorting and Classification,” *Cytometry Part A*, vol. 95, no. 5, pp. 499–509, 2019, doi: 10.1002/cyto.a.23764.

[120] A. Kleiber, D. Kraus, T. Henkel, and W. Fritzsche, “Review: Tomographic imaging flow cytometry,” *Lab on a Chip*, vol. 21, no. 19. Royal Society of Chemistry, pp. 3655–3666, Oct. 07, 2021. doi: 10.1039/d1lc00533b.

[121] F. Merola *et al.*, “Tomographic flow cytometry by digital holography,” *Light Sci Appl*, vol. 6, no. 4, Apr. 2017, doi: 10.1038/lsa.2016.241.

[122] M. Nassar *et al.*, “Label-Free Identification of White Blood Cells Using Machine Learning,” *Cytometry Part A*, vol. 95, no. 8, pp. 836–842, 2019, doi: 10.1002/cyto.a.23794.

[123] M. Doan *et al.*, “Diagnostic Potential of Imaging Flow Cytometry,” *Trends in Biotechnology*, vol. 36, no. 7. Elsevier Ltd, pp. 649–652, 2018. doi: 10.1016/j.tibtech.2017.12.008.

[124] P. Rees *et al.*, “Nanoparticle vesicle encoding for imaging and tracking cell populations,” *Nat Methods*, vol. 11, no. 11, pp. 1177–1181, Oct. 2014, doi: 10.1038/nmeth.3105.

[125] H. Mikami *et al.*, “Virtual-freezing fluorescence imaging flow cytometry,” *Nat Commun*, vol. 11, no. 1, Dec. 2020, doi: 10.1038/s41467-020-14929-2.

[126] M. Sarimollaoglu, D. A. Nedosekin, Y. A. Menyaev, M. A. Juratli, and V. P. Zharov, “Nonlinear photoacoustic signal amplification from single targets in absorption background,” *Photoacoustics*, vol. 2, no. 1, pp. 1–11, 2014, doi: 10.1016/J.PACS.2013.11.002.

[127] R. H. Edgar, A.-P. Samson, T. Kocsis, and J. A. Viator, “Photoacoustic Flow Cytometry Using Functionalized Microspheres for Selective Detection of Bacteria,” *Micromachines (Basel)*, vol. 14, no. 3, p. 573, Feb. 2023, doi: 10.3390/mi14030573.

[128] D. A. Nedosekin *et al.*, “Photoacoustic in vitro flow cytometry for nanomaterial research,” *Photoacoustics*, vol. 6, pp. 16–25, Jun. 2017, doi: 10.1016/j.pacs.2017.03.002.

[129] R. H. Edgar *et al.*, “Bacteriophage-mediated identification of bacteria using photoacoustic flow cytometry,” *J Biomed Opt*, vol. 24, no. 11, p. 1, Nov. 2019, doi: 10.1117/1.jbo.24.11.115003.

[130] A. Sun *et al.*, “Acoustic Standing Wave Aided Multiparametric Photoacoustic Imaging Flow Cytometry,” *Anal Chem*, vol. 93, no. 44, pp. 14820–14827, 2021, doi: 10.1021/acs.analchem.1c03713.

[131] F. Liu *et al.*, “An opto-acousto-fluidic microscopic system with a high spatiotemporal resolution for microfluidic applications,” *Opt Express*, vol. 27, no. 2, p. 1425, Jan. 2019, doi: 10.1364/oe.27.001425.

[132] E. I. Galanzha and V. P. Zharov, “Photoacoustic flow cytometry,” *Methods*, vol. 57, no. 3. pp. 280–296, 2012. doi: 10.1016/j.ymeth.2012.06.009.

[133] Y. Suo, Z. Gu, and X. Wei, “Advances of In Vivo Flow Cytometry on Cancer Studies,” *Cytometry Part A*, vol. 97, no. 1. Wiley-Liss Inc., pp. 15–23, 2020. doi: 10.1002/cyto.a.23851.

[134] C. Cai *et al.*, “In vivo photoacoustic flow cytometry for early malaria diagnosis,” *Cytometry Part A*, vol. 89, no. 6, pp. 531–542, 2016, doi: 10.1002/cyto.a.22854.

[135] V. v. Tuchin, A. Tárnok, and V. P. Zharov, “In vivo flow cytometry: A horizon of opportunities,” *Cytometry Part A*, vol. 79 A, no. 10. pp. 737–745, Oct. 2011. doi: 10.1002/cyto.a.21143.

[136] X. Tan, R. Patil, P. Bartosik, J. M. Runnels, C. P. Lin, and M. Niedre, “In Vivo Flow Cytometry of Extremely Rare Circulating Cells,” *Sci Rep*, vol. 9, no. 1, Dec. 2019, doi: 10.1038/s41598-019-40143-2.

[137] J. V. Sweedler and E. A. Arriaga, “Single cell analysis,” *Analytical and Bioanalytical Chemistry*, vol. 387, no. 1. pp. 1–2, Jan. 2007. doi: 10.1007/s00216-006-0921-4.

[138] S. J. Altschuler and L. F. Wu, “Cellular Heterogeneity: Do Differences Make a Difference?,” *Cell*, vol. 141, no. 4. Elsevier B.V., pp. 559–563, 2010. doi: 10.1016/j.cell.2010.04.033.

[139] K. Klepárník and F. Foret, “Recent advances in the development of single cell analysis-A review,” *Analytica Chimica Acta*, vol. 800. pp. 12–21, Oct. 24, 2013. doi: 10.1016/j.aca.2013.09.004.

[140] Q. Dai *et al.*, “Quantifying the Ligand-Coated Nanoparticle Delivery to Cancer Cells in Solid Tumors,” *ACS Nano*, vol. 12, no. 8, pp. 8423–8435, Aug. 2018, doi: 10.1021/acsnano.8b03900.

[141] S. Theiner, K. Loehr, G. Koellensperger, L. Mueller, and N. Jakubowski, “Single-cell analysis by use of ICP-MS,” *Journal of Analytical Atomic Spectrometry*, vol. 35, no. 9. Royal Society of Chemistry, pp. 1784–1813, Sep. 01, 2020. doi: 10.1039/d0ja00194e.

[142] M. Sousa De Almeida, E. Susnik, B. Drasler, P. Taladriz-Blanco, A. Petri-Fink, and B. Rothen-Rutishauser, “Understanding nanoparticle endocytosis to improve targeting strategies in nanomedicine,” *Chemical Society Reviews*, vol. 50, no. 9. Royal Society of Chemistry, pp. 5397–5434, May 07, 2021. doi: 10.1039/d0cs01127d.

[143] Y. Xiao *et al.*, “Effect of Surface Modifications on Cellular Uptake of Gold Nanorods in Human Primary Cells and Established Cell Lines,” *ACS Omega*, vol. 5, no. 50, pp. 32744–32752, Dec. 2020, doi: 10.1021/acsomega.0c05162.

[144] V. Sheth *et al.*, “Quantifying Intracellular Nanoparticle Distributions with Three-Dimensional Super-Resolution Microscopy,” *ACS Nano*, vol. 17, no. 9, pp. 8376–8392, May 2023, doi: 10.1021/acsnano.2c12808.

[145] J. Cauzzo, M. Nystad, A. M. Holsæter, P. Basnet, and N. Škalko-Basnet, “Following the fate of dye-containing liposomes in vitro,” *Int J Mol Sci*, vol. 21, no. 14, pp. 1–17, Jul. 2020, doi: 10.3390/ijms21144847.

[146] N. D. Donahue, H. Acar, and S. Wilhelm, “Concepts of nanoparticle cellular uptake, intracellular trafficking, and kinetics in nanomedicine,” *Advanced Drug Delivery Reviews*, vol. 143. Elsevier B.V., pp. 68–96, Mar. 15, 2019. doi: 10.1016/j.addr.2019.04.008.

[147] L. Rodriguez-Lorenzo, K. Fytianos, F. Blank, C. Von Garnier, B. Rothen-Rutishauser, and A. Petri-Fink, “Fluorescence-encoded gold nanoparticles: Library design and modulation of cellular uptake into dendritic cells,” *Small*, vol. 10, no. 7, pp. 1341–1350, Apr. 2014, doi: 10.1002/smll.201302889.

[148] S. Roussel, P. Grenier, V. Chénard, and N. Bertrand, “Dual-Labelled Nanoparticles Inform on the Stability of Fluorescent Labels In Vivo,” *Pharmaceutics*, vol. 15, no. 3, Mar. 2023, doi: 10.3390/pharmaceutics15030769.

[149] J. P. Robinson, “Flow cytometry: past and future,” *BioTechniques*, vol. 72, no. 4. Future Science Ltd, pp. 159–169, Apr. 01, 2022. doi: 10.2144/btn-2022-0005.

[150] R. P. Friedrich *et al.*, “Flow cytometry for intracellular SPION quantification: Specificity and sensitivity in comparison with spectroscopic methods,” *Int J Nanomedicine*, vol. 10, pp. 4185–4201, 2015, doi: 10.2147/IJN.S82714.

[151] R. R. Jahan-Tigh, C. Ryan, G. Obermoser, and K. Schwarzenberger, “Flow cytometry,” *Journal of Investigative Dermatology*, vol. 132, no. 10. Nature Publishing Group, pp. 1–6, 2012. doi: 10.1038/jid.2012.282.

[152] R. M. Zucker, E. J. Massaro, K. M. Sanders, L. L. Degn, and W. K. Boyes, “Detection of TiO2 nanoparticles in cells by flow cytometry,” *Cytometry Part A*, vol. 77, no. 7, pp. 677–685, Jul. 2010, doi: 10.1002/cyto.a.20927.

[153] H. Suzuki, T. Toyooka, and Y. Ibuki, “Simple and easy method to evaluate uptake potential of nanoparticles in mammalian cells using a flow cytometric light scatter analysis,” *Environ Sci Technol*, vol. 41, no. 8, pp. 3018–3024, Apr. 2007, doi: 10.1021/es0625632.

[154] S. D. Perrault and W. C. W. Chan, “Synthesis and Surface Modification of Highly Monodispersed, Spherical Gold Nanoparticles of 50−200 nm,” *J Am Chem Soc*, vol. 131, no. 47, pp. 17042–17043, Jun. 2009, doi: 10.1021/ja907069u.

[155] B. Y. J. Turkevich, P. C. Stevenson, and J. Hillier, “A Study of the Nucleation and Growth Processes in the Synthesis of Colloidal Gold,” *Compt. rend. U.R.S.S*, vol. 47, no. 1. Turkevich and Hillier, p. 30, 1941.

[156] L. Rainville, M. C. Dorais, and D. Boudreau, “Controlled synthesis of low polydispersity Ag@SiO2 core-shell nanoparticles for use in plasmonic applications,” *RSC Adv*, vol. 3, no. 33, pp. 13953–13960, Jun. 2013, doi: 10.1039/c3ra41677a.

[157] D. Paramelle, A. Sadovoy, S. Gorelik, P. Free, J. Hobley, and D. G. Fernig, “A rapid method to estimate the concentration of citrate capped silver nanoparticles from UV-visible light spectra,” *Analyst*, vol. 139, no. 19, pp. 4855–4861, Jun. 2014, doi: 10.1039/c4an00978a.

[158] W. Yang *et al.*, “Nanoparticle Surface Engineering with Heparosan Polysaccharide Reduces Serum Protein Adsorption and Enhances Cellular Uptake,” *Nano Lett*, vol. 22, no. 5, pp. 2103–2111, Jun. 2022, doi: 10.1021/acs.nanolett.2c00349.

[159] W. Yang *et al.*, “Controlling Nanoparticle Uptake in Innate Immune Cells with Heparosan Polysaccharides,” *Nano Lett*, vol. 22, no. 17, pp. 7119–7128, Sep. 2022, doi: 10.1021/acs.nanolett.2c02226.

[160] F. Wang *et al.*, “Scattered Light Imaging Enables Real-Time Monitoring of Label-Free Nanoparticles and Fluorescent Biomolecules in Live Cells,” *J Am Chem Soc*, vol. 141, no. 36, pp. 14043–14047, Jun. 2019, doi: 10.1021/jacs.9b05894.

[161] M. Okuyama *et al.*, “Small-molecule mimics of an α-helix for efficient transport of proteins into cells,” *Nat Methods*, vol. 4, no. 2, pp. 153–159, Jun. 2007, doi: 10.1038/nmeth997.

[162] A. N. Frickenstein *et al.*, “Quantification of monodisperse and biocompatible gold nanoparticles by single-particle ICP-MS,” *Anal Bioanal Chem*, 2023, doi: 10.1007/s00216-023-04540-x.

[163] N. D. Donahue *et al.*, “Assessing nanoparticle colloidal stability with single-particle inductively coupled plasma mass spectrometry (SP-ICP-MS),” *Anal Bioanal Chem*, vol. 412, no. 22, pp. 5205–5216, Sep. 2020, doi: 10.1007/s00216-020-02783-6.

[164] N. D. Donahue *et al.*, “Quantifying Chemical Composition and Reaction Kinetics of Individual Colloidally Dispersed Nanoparticles,” *Nano Lett*, vol. 22, no. 1, pp. 294–301, Jan. 2022, doi: 10.1021/acs.nanolett.1c03752.

[165] H. MATSUI, T. ITO, and S.-I. OHNISHI, “PHAGOCYTOSIS BY MACROPHAGES III. EFFECTS OF HEAT-LABILE OPSONIN AND POLY(L-LYSINE) HIROSHI MATSUI, TADANAO ITO AND SHUN-ICHI OHNISHI,” 1983.

[166] H. H. Gustafson, D. Holt-Casper, D. W. Grainger, and H. Ghandehari, “Nanoparticle uptake: The phagocyte problem,” *Nano Today*, vol. 10, no. 4. Elsevier B.V., pp. 487–510, Jun. 2015. doi: 10.1016/j.nantod.2015.06.006.

[167] B. D. Chithrani, A. A. Ghazani, and W. C. W. Chan, “Determining the size and shape dependence of gold nanoparticle uptake into mammalian cells,” *Nano Lett*, vol. 6, no. 4, pp. 662–668, Apr. 2006, doi: 10.1021/nl052396o.

[168] A. M. Syed *et al.*, “Three-Dimensional Imaging of Transparent Tissues via Metal Nanoparticle Labeling,” *J Am Chem Soc*, vol. 139, no. 29, pp. 9961–9971, Jun. 2017, doi: 10.1021/jacs.7b04022.

[169] R. M. Zucker, J. N. R. Ortenzio, and W. K. Boyes, “Characterization, detection, and counting of metal nanoparticles using flow cytometry,” *Cytometry Part A*, vol. 89, no. 2, pp. 169–183, Jun. 2016, doi: 10.1002/cyto.a.22793.

[170] J. B. Simonsen, N. E. A. Reeler, A. Fossum, K. A. Lerstrup, B. W. Laursen, and K. Nørgaard, “Quantifying and sorting of gold nanoparticle dimers from complex reaction mixtures using flow cytometry,” *Nano Res*, vol. 9, no. 10, pp. 3093–3098, Jun. 2016, doi: 10.1007/s12274-016-1192-9.

[171] S. Zhu *et al.*, “Size Differentiation and Absolute Quantification of Gold Nanoparticles via Single Particle Detection with a Laboratory-Built High-Sensitivity Flow Cytometer,” *J Am Chem Soc*, vol. 132, no. 35, pp. 12176–12178, Jun. 2010, doi: 10.1021/ja104052c.

[172] S. Behzadi *et al.*, “Cellular uptake of nanoparticles: Journey inside the cell,” *Chemical Society Reviews*, vol. 46, no. 14. Royal Society of Chemistry, pp. 4218–4244, Jul. 21, 2017. doi: 10.1039/c6cs00636a.

[173] V. Sheth, L. Wang, R. Bhattacharya, P. Mukherjee, and S. Wilhelm, “Strategies for Delivering Nanoparticles across Tumor Blood Vessels,” *Advanced Functional Materials*, vol. 31, no. 8. Wiley-VCH Verlag, Feb. 01, 2021. doi: 10.1002/adfm.202007363.

[174] S. K. Rodal, G. Skretting, Ø. Garred, F. Vilhardt, B. Van Deurs, and K. Sandvig, “Extraction of Cholesterol with Methyl-Cyclodextrin Perturbs Formation of Clathrin-coated Endocytic Vesicles,” 1999.

[175] L. Di Marzio *et al.*, “pH-sensitive non-phospholipid vesicle and macrophage-like cells: Binding, uptake and endocytotic pathway,” *Biochimica et Biophysica Acta (BBA) - Biomembranes*, vol. 1778, no. 12, pp. 2749–2756, Jun. 2008, doi: 10.1016/J.BBAMEM.2008.07.029.

[176] H. Zhang *et al.*, “Carbon Nitride Nanosheets for Imaging Traceable CpG Oligodeoxynucleotide Delivery,” *ACS Appl Nano Mater*, vol. 4, no. 8, pp. 8546–8555, Jun. 2021, doi: 10.1021/acsanm.1c01658.

[177] R. Kapetanovic *et al.*, “Contribution of phagocytosis and intracellular sensing for cytokine production by Staphylococcus aureus-activated macrophages,” *Infect Immun*, vol. 75, no. 2, pp. 830–837, Jun. 2007, doi: 10.1128/IAI.01199-06.

[178] J. W. Perry and C. E. Wobus, “Endocytosis of Murine Norovirus 1 into Murine Macrophages Is Dependent on Dynamin II and Cholesterol,” *J Virol*, vol. 84, no. 12, pp. 6163–6176, Jun. 2010, doi: 10.1128/jvi.00331-10.

[179] B. J. Reisman *et al.*, “Apoptolidin family glycomacrolides target leukemia through inhibition of ATP synthase,” *Nat Chem Biol*, vol. 18, no. 4, pp. 360–367, Jun. 2022, doi: 10.1038/s41589-021-00900-9.

[180] D. Kumar, I. Mutreja, K. Chitcholtan, and P. Sykes, “Cytotoxicity and cellular uptake of different sized gold nanoparticles in ovarian cancer cells,” *Nanotechnology*, vol. 28, no. 47, Nov. 2017, doi: 10.1088/1361-6528/aa935e.

[181] Y. Li and N. A. Monteiro-Riviere, “Mechanisms of cell uptake, inflammatory potential and protein corona effects with gold nanoparticles,” *Nanomedicine*, vol. 11, no. 24, pp. 3185–3203, Dec. 2016, doi: 10.2217/nnm-2016-0303.

[182] C. Åberg, “Kinetics of nanoparticle uptake into and distribution in human cells,” *Nanoscale Adv*, vol. 3, no. 8, pp. 2196–2212, 2021, doi: 10.1039/d0na00716a.

[183] N. Vtyurina, C. Åberg, and A. Salvati, “Imaging of nanoparticle uptake and kinetics of intracellular trafficking in individual cells,” *Nanoscale*, vol. 13, no. 23, pp. 10436–10446, Jun. 2021, doi: 10.1039/d1nr00901j.

[184] J. Blechinger, A. T. Bauer, A. A. Torrano, C. Gorzelanny, C. Bräuchle, and S. W. Schneider, “Uptake kinetics and nanotoxicity of silica nanoparticles are cell type dependent,” *Small*, vol. 9, no. 23, pp. 3970–3980, Dec. 2013, doi: 10.1002/smll.201301004.

[185] Q. Zhang *et al.*, “Quantitative refractive index distribution of single cell by combining phase-shifting interferometry and AFM imaging,” *Sci Rep*, vol. 7, no. 1, Dec. 2017, doi: 10.1038/s41598-017-02797-8.

[186] E. C. Cho, J. Xie, P. A. Wurm, and Y. Xia, “Understanding the role of surface charges in cellular adsorption versus internalization by selectively removing gold nanoparticles on the cell surface with a I 2/KI etchant,” *Nano Lett*, vol. 9, no. 3, pp. 1080–1084, Mar. 2009, doi: 10.1021/nl803487r.

[187] A. Reichard and K. Asosingh, “Best Practices for Preparing a Single Cell Suspension from Solid Tissues for Flow Cytometry,” *Cytometry Part A*, vol. 95, no. 2, pp. 219–226, Feb. 2019, doi: 10.1002/cyto.a.23690.